

# Increased Control over Reaction Conditions in a Hybrid Trap

Inauguraldissertation

zur  
Erlangung der Würde eines Doktors der Philosophie  
vorgelegt der  
Philosophisch-Naturwissenschaftlichen Fakultät  
der Universität Basel  
von

**Pascal Eberle**  
aus Basel-Stadt, Schweiz

Basel, 2020

Originaldokument gespeichert auf dem Dokumentenserver der Universität Basel  
edoc.unibas.ch

Licensed under the  
Attribution-NonCommercial 4.0 International (CC BY-NC 4.0) License



Genehmigt von der Philosophisch-Naturwissenschaftlichen Fakultät  
auf Antrag von

Prof. Dr. Stefan Willitsch und Prof. Dr. David Carty

Basel, den 18.09.2018

Prof. Dr. Martin Spiess

## Abstract

This thesis presents work towards increased control over reaction conditions in a hybrid trap, which is composed of an ion trap spatially overlapped with a magneto-optical trap (MOT).

A novel type of hybrid trap is presented with the aim to increase the control over collision energies. As normally on our setup both the neutral and ionic species are continuously cooled, collision energies are low and hard to control. To solve this problem, a dynamic MOT was created, where an atom cloud is shuttled between two off-center positions within the trap. A detailed description of the new hybrid trap setup is presented. The generation of the MOT laser light and its manipulation inside an acousto-optical modulator setup driven by a home-built radio-frequency setup is discussed. The shuttling atom cloud was analysed by time-of-flight experiments, which were compared to results from Monte Carlo trajectory simulations. During reaction measurements, the atoms can be moved at velocities of 3.1 to 4.8 m·s<sup>-1</sup>, corresponding to kinetic energies of the rubidium atoms of  $E_{\text{kin}} = 50$  mK to 120 mK.

For the ions, work towards implementing vibrationally state-selected molecular oxygen ions is presented. Ions were produced by resonant multiphoton ionisation and spectroscopy was performed on the  $3d\delta$   $^3\Phi$  Rydberg states. First reactions of molecular oxygen ions in the vibrational ground state with a stationary atom cloud were measured. It was found that the reaction rate did not depend on the excited state fraction of the rubidium atoms. This was rationalised with the crossing of the potential energy surface of a charge-transfer exit channel close to the potential minimum of the ground-state entrance-channel potential energy surface.



# Acknowledgements

I would first like to thank Stefan Willitsch for the opportunity to do this exciting research project in his group. His continuous support, his patience and his knowledge were very valuable.

I would like to thank Alexander Dörfler for his work on the experiment. He did all the simulations and helped immensely in getting the shuttling atom trap to work. His fresh input when he joined the experiment was of great importance.

I would like to acknowledge Ravi Krishnamurthy for the initial setup of the experiment.

I would like to thank Claudio von Planta for the work he did during his Master thesis on this project. He developed the simulations used to analyse the shuttling experiment.

I would like to thank Uxía Rivero for being a great office neighbour and her support. I would also like to acknowledge the rest of the group, current and past members, for the enjoyable and friendly atmosphere.

I would like to acknowledge the visiting students who spent time in the group for their COMIQ secondments. Amir Mahdian from Ulm (Hecker Denschlag group) had valuable input for the alignment process of the shuttling atom trap. Luca Carcagni from Bonn (Köhl group) helped with temperature determination of the atom cloud.

I would like to thank Anatoly Johnson for support with all laser related problems and some help with LabVIEW programming.

I would like to thank Georg Holderied for electronics support. I would also like to acknowledge help from Andreas Tonin from the physics department's electronic lab.

I would like to thank the mechanics workshop: Philip Knöpfel, Grischa Martin, Dieter Wild and their apprentices. Their excellent mechanical work was crucial in the success of many aspects of the experiment.

I would like to thank David Carty for kindly agreeing to be the second examiner for this thesis.

Finally, I would like to thank my family and friends for their continuous support. Without them, the conclusion to this work would have not been accomplished.



# Contents

<b>1</b>	<b>Background and Motivation</b>	<b>1</b>
1.1	A Brief History of Moving Atoms . . . . .	2
1.2	Hybrid Traps . . . . .	7
1.3	Controlled Chemistry in Ion Traps . . . . .	8
<b>2</b>	<b>Introduction - Theory and General Methods</b>	<b>11</b>
2.1	Ion-Neutral Collisions . . . . .	11
2.1.1	Classical Capture Model . . . . .	11
2.1.2	Relevant Interaction Potentials . . . . .	13
2.1.3	Langevin Collision Rate . . . . .	13
2.1.4	Extension to Quadrupol-Ion Interaction . . . . .	14
2.1.5	Quantum-Mechanical Effects . . . . .	14
2.2	Light-Matter Interaction . . . . .	15
2.2.1	Two-Level System . . . . .	15
2.2.2	Light Forces . . . . .	16
2.2.3	Doppler Laser Cooling . . . . .	17
2.2.4	Laser Cooling in $\text{Ca}^+$ and Rb . . . . .	19
2.2.5	Photoionisation of $\text{O}_2$ Using the $1,3\Phi$ States . . . . .	19
2.3	Magneto-Optical Trap . . . . .	22
2.3.1	Operation Principle . . . . .	22
2.3.2	Pushing Atoms with Light . . . . .	24
2.3.3	Atom Number and Density Estimation . . . . .	24
2.4	Ion Trapping . . . . .	26
2.4.1	Equations of Motion . . . . .	26
2.4.2	Coulomb Crystals . . . . .	28
2.5	Hybrid Trap . . . . .	29
2.5.1	Determination of Reaction Rate Constants . . . . .	29
2.5.2	Calculating the Overlap . . . . .	29
2.6	$\text{O}_2^+$ state detection . . . . .	31
2.6.1	Determination of Vibrational State . . . . .	31
<b>3</b>	<b>The Shuttling MOT</b>	<b>33</b>
3.1	Technical Implementation and Methods . . . . .	34
3.1.1	Experimental Setup . . . . .	34
3.1.2	Operation Principle . . . . .	34
3.1.3	Light Generation . . . . .	36
3.1.4	Light Manipulation . . . . .	37
3.1.5	Radio Frequency Generation and Manipulation . . . . .	39
3.1.6	Pulse Sequence Programming . . . . .	41
3.1.7	Imaging . . . . .	42

3.1.8	Simulations . . . . .	43
3.2	Measurements and Results . . . . .	44
3.2.1	Time-of-Flight Measurements . . . . .	45
3.2.2	Results from Simulations . . . . .	46
3.2.3	Reactions with Ion Crystals . . . . .	47
3.2.4	Second Order Rate Constant Estimation . . . . .	48
3.3	Summary and Conclusion . . . . .	51
<b>4</b>	<b>Molecular Oxygen Ions</b>	<b>53</b>
4.1	Molecular Beam and REMPI Setup . . . . .	53
4.1.1	Pulsed Valve and Source Chamber . . . . .	54
4.1.2	Time-of-Flight Spectrometer and Ionisation Chamber . . . . .	55
4.1.3	REMPI Laser Setup . . . . .	56
4.1.4	Measurement Control and Signal Acquisition . . . . .	56
4.2	Measurements using the Molecular Beam . . . . .	57
4.2.1	O <sub>2</sub> REMPI Spectra Analysis and Interpretation . . . . .	57
4.2.2	Molecular Beam Alignment and Failed Loading . . . . .	58
4.3	Reactions using O <sub>2</sub> <sup>+</sup> in the Vibrational Ground State . . . . .	63
4.3.1	Loading and Vibrational State Determination . . . . .	64
4.3.2	Reactions with a Stationary Atom Cloud . . . . .	65
4.3.3	O <sub>2</sub> <sup>+</sup> + Rb Reaction Rate Measurements Summary . . . . .	67
4.3.4	Reaction Product Analysis . . . . .	69
4.3.5	Possible Reaction Mechanisms . . . . .	70
4.4	Summary and Conclusion . . . . .	72
<b>5</b>	<b>Conclusion and Outlook</b>	<b>75</b>
<b>A</b>	<b>New In-Vacuum Components</b>	<b>77</b>
A.1	New Calcium and Rubidium Sources . . . . .	77
A.2	New Ion Trap . . . . .	79
<b>B</b>	<b>LabVIEW Programs</b>	<b>81</b>
B.1	LaserLock . . . . .	81
B.2	Custom Andor EMCCD Camera Program . . . . .	83
B.3	Experiment Control . . . . .	83
B.3.1	Hybrid Trap Control . . . . .	83
B.3.2	REMPI Program . . . . .	84
B.3.3	Atom Cloud Time-of-Flight Monitoring . . . . .	85
B.4	Analysis Software . . . . .	85
B.4.1	Fitting Tools for Crystal Analysis . . . . .	85
B.4.2	MOT Atom Number and Density Analysis . . . . .	86
B.4.3	Crystal and Atom Cloud Overlap Calculation . . . . .	86
<b>C</b>	<b>Mini-Circuits Radio-Frequency Components</b>	<b>93</b>
C.1	Voltage-Controlled Oscillator (VCO) . . . . .	93
C.2	Fixed and Voltage-Variable Attenuators . . . . .	93
C.3	Two-Way and Four-Way RF Splitter . . . . .	94
C.4	Single Pole Double Throw Switches . . . . .	94
C.5	Amplifiers . . . . .	94

# List of Figures

2.1	Impact Parameter Scheme . . . . .	12
2.2	Two level Scheme . . . . .	16
2.3	Doppler Cooling Scheme . . . . .	17
2.4	Ca <sup>+</sup> and Rb Energy Level Structure . . . . .	19
2.5	Hund's coupling cases a and b . . . . .	20
2.6	Magneto-Optical Trap Scheme . . . . .	23
2.7	Magneto-Optical Trap Zeeman Levels . . . . .	23
2.8	Paul Trap Schematic . . . . .	27
2.9	Coulomb Crystal Images . . . . .	29
2.10	Overlap Calculation Schematic . . . . .	30
3.1	Experiment Schematic . . . . .	35
3.2	Shuttling Operation Principle of the Shuttling Atom Trap . . . . .	36
3.3	The 780 nm Laser Setup . . . . .	37
3.4	AOM Setup Schematic . . . . .	38
3.5	Radio Frequency Generation for the AOM Setup . . . . .	39
3.6	Shuttling Operation Pulse Sequence . . . . .	43
3.7	Shuttling Imaging System and Experimental Images . . . . .	44
3.8	Shuttling Atom Cloud Time of Flight Trace . . . . .	46
3.9	Collision Energies versus Push Beam Powers . . . . .	47
3.10	Collision Energy Spread Obtained from Simulations . . . . .	48
3.11	Ca <sup>+</sup> -Rb Pseudo-First Order Reaction Rate with Shuttling . . . . .	49
4.1	Molecular Beam Machine Setup . . . . .	54
4.2	Piezo Valve Schematic . . . . .	55
4.3	O <sub>2</sub> <sup>+</sup> Time-of-Flight Trace . . . . .	58
4.4	O <sub>2</sub> <sup>3</sup> Φ <sub>2,3</sub> (ν = 0) spectrum . . . . .	59
4.5	O <sub>2</sub> <sup>3</sup> Φ <sub>2,3</sub> (ν = 1) spectrum . . . . .	60
4.6	O <sub>2</sub> <sup>3</sup> Φ <sub>2,3</sub> (ν = 2) spectrum . . . . .	61
4.7	Molecular Beam Alignment . . . . .	62
4.8	Loading O <sub>2</sub> <sup>+</sup> from the Molecular Beam . . . . .	64
4.9	Loading O <sub>2</sub> <sup>+</sup> from Leaked Background Oxygen . . . . .	65
4.10	O <sub>2</sub> <sup>+</sup> State Confirmation with Xenon . . . . .	66
4.11	O <sub>2</sub> + Rb Reaction Rate Summary . . . . .	68
4.12	Product REMS of O <sub>2</sub> <sup>+</sup> + Rb Reactions . . . . .	69
4.13	Entrance and Product Channels in O <sub>2</sub> <sup>+</sup> and Rb Reactions . . . . .	72
A.1	New Ca and Rb Atom Sources . . . . .	78
A.2	New Ion Trap . . . . .	79
B.1	LaserLock Programs . . . . .	87
B.2	Custom EMCCD Camera Software . . . . .	88

B.3 Hybrid Trap Controls . . . . .	89
B.4 Atom Shuttling Light Control & REMPI Program . . . . .	90
B.5 Crystal & MOT Analysis Programs . . . . .	91
B.6 Overlap Estimation Program . . . . .	92

# Chapter 1

## Background and Motivation

The work presented in this thesis can be summarised under the topic *cold and controlled chemistry*. The main focus was the continuation of the experiments performed by Felix Hall, who originally built and designed the experimental apparatus this thesis is based on [1]. The aim was to increase the control over the reaction conditions in the ion-neutral systems studied.

**The Experiment** The core of the experimental apparatus is a so-called hybrid trap, a combination of a magneto-optical trap (MOT) for neutral atoms and an ion trap in the form of a linear Paul trap for ionic species. In a magneto-optical trap, the combination of a light field and a magnetic field are used to provide cooling and trapping for neutral atoms. On this experiment, the MOT is used with rubidium-87 exclusively. The linear Paul trap uses a combination of static and dynamic electrical fields to trap ionic species and laser cooling can be applied to suitable ions, which are singly charged calcium ions in our case. The laser-cooled ions can be used to sympathetically cool other ionic species which are not accessible by direct laser cooling.

The purpose of our hybrid trapping experiment is the study of cold chemistry at low collision energies with a high control over the reaction conditions. The first part of this thesis deals with the problem of control over the collision energy in hybrid trapping experiments. Since both the neutral and ionic species inside the hybrid trap are cooled, kinetic energies are low and difficult to tune. We tried to address this with the creation of a dynamic trap for the atoms, where the atoms are constantly shuttled between two off-center positions inside the MOT.

The second part of this thesis deals with the implementation of molecular ions into the hybrid trap. First work in this direction was already performed by Felix Hall with molecular nitrogen ions and this thesis presents work towards the incorporation of molecular oxygen ions into the hybrid trap. The direct comparison between molecular nitrogen ions and molecular oxygen ions is interesting, as both systems should exhibit similar characteristics. Molecular ions also open up the possibility of studying the influence of internal degrees of freedom such as vibration and rotation on the reactivity of the system. For this, molecular ions need to be prepared in selected vibrational and rotation states. One possibility of creating the desired states is the ionisation of suitable intermediate Rydberg states in the neutral molecule in a resonance-enhanced multiphoton ionisation (REMPI) scheme.

**Structure of This Thesis** This introduction will explore the history of cooling down samples of atoms and using various techniques to generate moving atoms at well-defined velocities. The second chapter gives an overview of the theory and methods used in this work. Introduced is the basic theory behind collisions of ionic and neutral species, the interaction of light and matter, from where the working principle behind the magneto-optical trap is introduced. The theory behind trapping ions in Paul traps is introduced and aspects of the combination of the two traps to form the hybrid trap are discussed. The theory and methods chapter is concluded with the discussion of the proposed determination of the vibrational state of molecular oxygen ions loaded into the ion trap. Chapter three deals with the aspects of the shuttling MOT. The experimental setup and technical implementation is discussed in detail. Presented are the results, which come in the form of time-of-flight traces and their comparison with results from simulations. First attempts at reactions with calcium ions in the ion trap are also discussed. The fourth chapter discusses work towards incorporating molecular oxygen ions into the hybrid trap. Spectroscopy on promising states for vibrationally selected molecular oxygen ions using REMPI is presented. First reactions with molecular oxygen ions in the vibrational ground state are shown. Finally, the fifth chapter concludes the main part of the thesis and gives an outlook to future work. Some more work on the design of new atom sources is presented in the appendix, where also some of the software written during this work is presented. The appendix is concluded with an overview of the radio-frequency components used in the shuttling MOT setup.

## 1.1 A Brief History of Moving Atoms

In order to give an overview of how atoms have been moved using light forces, a brief history of controlling the motion of atoms using light shall be given here.

**Momentum Transfer between Photons and Atoms** Einstein's quantum theory of radiation [2], developed in 1917, predicted the transfer of momentum between a photon and an atom or molecule during absorption or emission. A few years later, the first experimental demonstration of the force photons can exert onto individual atoms was reported in 1933 by Frisch [3], who measured the displacement of a narrow atomic sodium beam illuminated with the D-line light from a sodium lamp. It was not until the invention of the laser with its high-power, tunable and narrow-band light that the idea of cooling atoms using light became feasible. Before the proposition of laser cooling, Ashkin put forward the prospect of using laser light to deflect atoms using photon scattering in 1970 [4], which was soon after realised in 1972 by Picqué and Vialle [5] and the group of Schieder and co-workers [6].

**Doppler Laser Cooling** Finally, the idea of using laser light to cool down atoms by scattering photons was proposed in 1975 in two independent papers by Hänsch and Schawlow [7] as well as Wineland and Dehmelt [8]. It did not take long and in 1978, the two groups of Neuhauser, Hohenstatt, Toschek and Dehmelt [9] as well as the group of Wineland, Drullinger and Walls [10] independently reported on successful laser cooling at almost the exact same time. Both groups reported the laser-cooling of singly charged ions of alkaline earth metals inside ion traps. Ion traps offer strong

confinement in deep traps and thus are able to trap ions even at room temperature. After initial trapping at room temperature, cooling light can then be applied to cool the ions.

**The Dipole Force** As neutral atoms are not as strongly influenced by electric and magnetic fields, ion traps do not work for them and other means of trapping needed to be devised. In 1978, the same year as the first successful Doppler laser cooling of ions, Ashkin proposed the idea of using an intense laser field to trap atoms using the dipole gradient force [11]. The dipole gradient force arises from the interaction of a strong light field with the induced dipole of an atom and was first suggested to be used for the manipulation of atoms in 1962 by Askar'yan [12], as well as Letokhov in 1968 [13]. First experimental evidence of this dipole force was presented in 1978 [14], where an intense, tightly focussed laser beam was used on a beam of sodium atoms to focus, defocus and steer the atomic beam.

**Using Laser Light to Stop Atoms** First work towards the cooling and trapping of neutral atoms using the scattering force was reported in two consecutive publications in 1985 by Prodan and co-workers [15] as well as Ertmer and co-workers [16]. Both groups presented the slowing, stopping and reversal of velocity of an atomic beam of sodium. Atoms could be produced at rest in the laboratory frame, but there was no continuous cooling or trapping yet. Since the atoms were produced from an effusive oven, they were moving at several hundred meters per second in the lab frame and needed to be slowed down. As the light applied slows the atoms down, changes in the Doppler shift will move the atom's transition out of resonance with the slowing laser beam. The two groups used different approaches to circumvent this. Ertmer and co-workers used an electro-optical modulator to chirp the laser frequency to compensate for the change in Doppler shift, while Prodan and co-workers employed a steadily varying magnetic field along the travel direction of the atoms to use the Zeeman effect on the energy levels involved in the cooling transition to accommodate the changing Doppler shift as the atoms are slowed. Prodan and co-workers also noted the possibility of using light forces to produce atoms at well-controlled velocities together with atoms at rest to study velocity-sensitive collisions.

A few months later, the first group used their atom stopping technique to load a purely magnetic trap presented in a letter by Migdall and co-workers [17]. The magnetic trap was formed by two co-axial coils in anti-Helmholtz configuration creating a quadrupolar magnetic field. Atom numbers were probed with a weak laser beam after varying trapping times and a time constant of 0.83(7) seconds was found for the exponential decay of atoms remaining inside the trap. Atom densities were very low at only around  $10^3 \text{ cm}^{-3}$ .

**The Optical Molasses Technique** Just a month after the loading of a magnetic trap by a stopped atom beam, the group of Chu presented the first continuous three-dimensional cooling of atoms using counter-propagating beams [18]. Sodium atoms were cooled in three dimensions using 3 pairs of counter-propagating laser beams. Atoms were generated by laser ablation of a sodium pellet and were loaded into the cooling region by pre-cooling with a chirped laser pulse. In this way, atoms at  $\sim 240 \text{ } \mu\text{K}$  were produced in the cooling region at comparably low densities of  $10^6 \text{ cm}^{-3}$ . As there is no restoring force, the atoms were not trapped and spend on average only

approximately 0.1 seconds in the cooling region. The technique was dubbed optical molasses, due to “. . . the observation that the motion of the atoms in a viscous fluid of photons (“optical molasses”) is analogous to diffusion in classical Brownian motion.” as the authors have noted.

A year later in 1986, the same group presented the loading of an optical dipole trap [19] similar to the one proposed by Ashkin in 1978 [11] from atoms inside an optical molasses as presented above. A laser beam at 220 mW was focused to a spot radius of  $\omega_0 \approx 10 \mu\text{m}$  to generate the dipole trap, where atoms can be trapped for approximately 1 second, limited by background gas ejecting trapped atoms when colliding. The densities were estimated to be on the order of  $10^{11} \text{ cm}^{-3}$ , but the authors estimate to only have around 500 atoms inside the trap. They note the possibility of moving the trapped atoms by slowly changing the position of the focus of the trapping laser, but only reaching a speed of around  $1 \text{ cm}\cdot\text{s}^{-1}$ .

**The Magneto-Optical Trap** The big breakthrough in cooling and trapping of neutral atoms was reported in 1987 in a paper by Raab and co-workers [20], where they introduced the magneto-optical trap. The basic principle behind the trap was the addition of a quadrupolar magnetic field to the optical molasses reported previously. This added a restoring force to the damping force, creating a trap for the atoms (the working principle is explained in more detail in section 2.3). The combination of the optical molasses with the quadrupolar magnetic field allowed the continuous cooling and trapping of atoms and provided a trap with unprecedented atom numbers, densities and temperatures. The trap presented could hold as many as  $10^7$  atoms at densities above  $10^{11} \text{ cm}^{-3}$  and temperatures reaching below 1 mK. For trap depth estimations, the authors used a short and intense laser pulse to move the trapped atoms in order to determine the minimal velocity with which most of the atoms are ejected from the trap. The authors also noted the robustness of the trap to intensity balance in the beams as well as purity of the circular polarisation and frequency of the laser beam. They also mentioned the effects of slight misalignment of the laser beams, which led to atoms settling in different local potential minima with the possibility of making atoms oscillate between them!

**Atomic Fountains** It did not take long after the introduction of the magneto-optical trap that the dense atom cloud it produces was used in experiments where control over the motion of the atoms is crucial. In 1989, Kasevich and co-workers presented the first successful implementation of an atomic fountain [21], an experiment in which an atom cloud gets launched upwards and then falls back down under the influence of gravity. The idea of an atomic fountain was first proposed by Zacharias in the early 1950’s [22], but limited experimental tools at that time prevented a working implementation of the proposed idea. To make the atomic fountain work, the group of Kasevich and co-workers used sodium atoms, which were precooled in a magneto-optical trap. After loading around  $5 \cdot 10^7$  atoms into the trap, the magnetic field was turned off, after which the intensity of the cooling beams was reduced, leading to further cooling of the atoms. The cooling beams were then switched off and pulse of an intense vertical laser beam tuned resonantly with a transition in sodium launched the atoms upwards at a velocity of  $2.4 \text{ m}\cdot\text{s}^{-1}$ . At the top of their trajectory, the atoms pass through an RF waveguide to perform spectroscopy on the hyperfine splitting of the ground state of the atoms using Ramsey interferometry [23]. The performance

as a frequency standard and thus reference clock was mentioned, but the experiment was never used in such a way.

One problem in the above mentioned initial implementation of an atomic fountain was the increase of the transversal spread of the atoms flying upwards after scattering photons from the pushing beam. The group addressed this problem in a publication in 1991, where they introduced a new scheme to push the atoms upwards [24]. Their setup consisted of a magneto-optical trap where two of the three counter-propagating laser beams were angled at  $45^\circ$  with regard to the vertical axis. To push the atoms upwards, the magnetic field was turned off, followed by a decrease of the frequency of the two laser beams propagating downwards, while the frequency of the two laser beams propagating upwards was increased. This created polarisation gradients propagating upwards at a speed of  $2.5 \text{ m}\cdot\text{s}^{-1}$ , which pushed the atoms upwards within the moving optical molasses.

As mentioned above, one of the applications of atomic fountains is the usage as a frequency and thus time standard. Until the establishment of atomic fountains as frequency standards, thermal atomic beams were used in the implementation of the most precise frequency standards available. The history of these frequency standards up until their replacement by fountain clocks is given in an article titled “NIST Primary Frequency Standards and the Realization of the SI Second” [25]. The first atomic fountain used as a clock was presented in 1996 [26] with a fractional frequency uncertainty of  $3 \cdot 10^{-15}$ , a description of the setup can be found in [27]. The atoms were launched using the moving optical molasses technique [24]. Even today, caesium fountains are some of the most precise atomic clocks [28] and are widely used as frequency standards, since the SI second is defined with respect to the hyperfine transition in caesium-133.<sup>1</sup>

**2D Magneto-Optical Traps** A different approach to generate a beam of slow atoms with high degree of control over the velocity of the atoms was presented by Chu and his group in 1990 [31]. They presented a two-dimensional version of the magneto-optical trap, acting as a funnel for atoms. A quadrupolar magnetic field was created by four parallel current wires in a “hairpin” arrangement, which created a zero-field axis at the center of the wire geometry. Two pairs of counter-propagating laser beams perpendicular to the zero-field axis provided cooling and trapping along these directions. There was no trapping along the zero-field axis, but a pair of counter-propagating laser beams provided cooling. A drift velocity of up to  $5 \text{ m}\cdot\text{s}^{-1}$  along the central axis could be imparted onto the atoms by creating a difference in either the intensity or the frequency of the two axial beams. For axial laser beams at different intensities, the atoms moved at a speed where they scattered the same amount of photons from both beams. In the case where the frequencies were different, the atoms moved at a speed where the frequencies of the two beams was Doppler shifted to be equal.

Similar 2D setups have been demonstrated for sodium atoms [32] and for caesium atoms [33]. A slightly different approach was employed by Swanson and co-workers in

---

<sup>1</sup>In recent years, novel types of atom clocks with improved accuracy have been developed. Examples include clocks based on optical transitions in ultra-cold strontium atoms in an optical lattice [29] or clocks based on single  $\text{Al}^+$  ions used for spectroscopy and cooled by a single laser-cooled ion ( $\text{Be}^+$  or  $\text{Mg}^+$ ) [30].

1996 [34], where they presented a 2D MOT for rubidium in which the atoms velocity was controlled using the moving optical molasses approach [24].

In 1997, Weyers and co-workers presented a 2D MOT that was not only able to push the atoms with the moving optical molasses approach, but also with a laser beam and a homogeneous magnetic field [35]. Atoms were cooled and trapped horizontally by two pairs of counter-propagating laser beams. Angled at  $14^\circ$  with respect to the vertical axis, another crossed pair of counter-propagating laser beams created the moving optical molasses that pushed the atoms downwards. As a second pushing method they employed a homogeneous magnetic field together with a stationary laser wave formed by opposite circular polarisation in the two vertical counter-propagating beams [36].

Two-dimensional magneto-optical traps are still an active research field and are mostly used to quickly load a 3D MOT used as an intermediate state for further experiments. 2D MOTs have been developed for many different type of atoms, for recent examples see [37–41].

**Transfer of Atoms between Two MOT Setups** The transfer of rubidium atoms between two magneto-optical traps was demonstrated by Myatt and co-workers [42]. Atoms were first loaded into a vapour cell MOT and, after the trap was switched off, pushed with a laser beam towards the second MOT. The atoms were guided towards the second MOT through a tube in which they were confined by a hexapole magnetic field. A very similar experiment was presented by Swanson and co-workers [43] for potassium atoms. Atoms were pushed out continuously from a first 3D MOT using a small, slowly diverging pushing beam, which pushed the atoms towards a second MOT in a different chamber. A 2D MOT setup in the tube connecting the two chambers improved transfer efficiency. Dimova and co-workers presented a similar setup where a red-detuned, high power, slowly diverging beam was used to transfer atoms in two independent setups using either rubidium or caesium [44]. In a setup presented by Mishra and co-workers, a hollow beam was used for guiding a cloud of rubidium atoms from one MOT to another [45].

A different approach to generate a velocity-tunable beam from a 3D MOT was presented by Lu and co-workers [46]. A standard three-dimensional MOT setup was used with three retro-reflected laser beams, where one of the mirrors used for retro-reflection had a hole in the middle, through which a slow beam of atoms could escape the MOT. The authors called this setup a “low-velocity intense atom source” (LVIS). The velocity could be tuned with either intensity or detuning of the cooling beams. Yan and co-workers presented a modification of the LVIS setup, where they guided the atom beam with a hollow blue-detuned laser beam [47].

**Application Example** A combination of the various techniques presented above was used in an atom interferometry setup presented by Müller and co-workers [48, 49]. Rubidium atoms were loaded into two separate 2D MOTs from which they were pushed with a laser beam towards their respective 3D MOT. The atoms loaded into the 3D MOTs were then launched towards each other with the moving optical molasses approach.

**Moving Atoms using the Optical Dipole Force** The experiments presented so far all used the scattering light force to move the atoms; in some cases, the dipole

force was used to guide atoms. The optical dipole force is a powerful tool and used in many types of experiments [50], some of which also used the optical dipole force to move atoms with high control.

Dahan and co-workers loaded caesium atoms from a MOT into an optical potential formed by a laser standing wave [51]. By introducing a frequency difference in the two counter-propagating laser beams, the optical potential started to move. By tuning the frequency difference, a constant inertial force was acting on the atoms, which made the atoms move and made the observation of Bloch oscillations [52, 53] of atoms possible. A similar setup to move sodium atoms was used by Wilkinson and co-workers [54] to observe atomic Wannier-Stark ladders [55]. Kuhr and co-workers used a standing wave dipole trap to trap and move a single atom loaded from a MOT [56]. The atom could be moved up to 1 cm with very high precision at speeds of 1 to 10 m·s<sup>-1</sup>.

Transport of atoms in an 1D optical lattice over distances of up to 20 cm has been presented by Schmid and co-workers [57], which was achieved using the overlap of an optical Bessel beam and a counter-propagating Gaussian beam to form the optical lattice. Dickerson and co-workers presented inertial sensing with an atom interferometer [58] where the atoms are launched vertically in a moving optical lattice, similarly to the atomic fountain experiments presented above.

**Other approaches** There also exist some approaches to move atoms controllably without using light. In one example, Greiner and co-workers load atoms from a 3D MOT into a purely magnetic quadrupole trap, from which the atoms were transported over a distance of 33 cm using a chain of quadrupole coils [59]. Controlled atom transport has also been presented by the same group in so-called magnetic conveyor belts on a chip using Ioffe-Pritchard-type trapping potentials [60].

## 1.2 Hybrid Traps

The concept of hybrid traps has first been proposed in 2003 by the group of Smith and co-workers [61]. The authors suggested overlapping a magneto-optical trap with a linear Paul trap and the simultaneous cooling of both species in both traps. A few years later, the first experimental implementation was presented in the form of a hybrid trap where neutral Yb atoms inside a MOT were overlapped with Yb<sup>+</sup> ions loaded into a surface ion trap [62, 63]. This spawned a research area with many new experimental demonstrations of hybrid trap systems consisting of MOTs overlapped with ion traps [64–67]. Other experiments used atoms inside a magnetic trap [68] or Bose-Einstein condensates formed inside crossed optical dipole traps [69, 70]. Also used were thermal atoms inside an optical dipole trap [71].

These experiments are of great interest for both physics and chemistry. Elastic collisions are observed, which can for example result in atom loss [68, 70, 71] or cooling of the ion [67, 69]. Reactive processes are observed as well, one example being charge-transfer reactions [63–65, 70, 72–74] which can either happen radiatively or non-radiatively. Also observed are molecule formation [65, 73, 75], quenching collisions leading to relaxation of internal excitations [76, 77] or spin-exchange collisions [74].

Even though many of these experiments demonstrate great control over various aspects of the experiments, tuning the collision energy is still not straight-forward. Quantum effects in the form of shape resonances are expected to be present in all of

these ion-neutral system. Calculations have shown that shape resonances are to be expected at commonly achievable collision energies in hybrid trapping experiments [78]. However, so far no shape resonances have been observed due to lack of control over the collision energy. Attempts where additional collision energy is introduced by introducing additional micromotion to the ions have not been able to resolve any fine structure expected to be seen due to quantum effects [65, 73, 75, 79].

In chapter 3, a new type of hybrid trap is introduced which attempts to solve the problem of adjustable collision energies. Off-center atom clouds are trapped in the MOT by creating a radiation-pressure imbalance in one of the beams. From this off-center position, atoms are pushed towards the ion trap center using an on-resonance laser beam. After passing the ion trap center and interacting with the ions, the atoms are trapped in an off-center position opposite the original one. From this other off-center position, the atoms are pushed back, interact with the ions and are cooled back into the first off-center position and a new cycle can begin. By carefully tuning the intensity of the pushing beam, atom clouds at well-defined velocities can be generated.

### 1.3 Controlled Chemistry in Ion Traps

The invention of the experimental techniques described in section 1.1 and 1.2 made it possible to study physical and chemical processes at very low temperatures. Next to the already introduced hybrid traps, some other methods will be highlighted here, for example reactions of laser-cooled calcium ions with velocity-selected  $\text{CH}_3\text{F}$  molecules [80] or with conformer-selected 3-aminophenol [81]. Cold and controlled molecules can also be created by Zeeman deceleration [82, 83] or Stark deceleration [82, 84]. Many other examples exist in this growing field and new techniques are constantly being developed, such as centrifuge deceleration of molecules [85]. Even direct laser cooling has been demonstrated for certain diatomic molecules such as  $\text{SrF}$  [86, 87],  $\text{YO}$  [88] and  $\text{CaF}$  [89, 90] and one polyatomic molecule,  $\text{SrOH}$  [91].

Other promising candidates for cold and controlled chemistry are molecular ions inside Coulomb crystals in ion traps [92]. Even though molecular ions can not be directly cooled themselves, they can be cooled sympathetically due to their Coulomb interaction with directly laser-coolable atomic ions. Examples of reactions with sympathetically cooled molecular ions include  $\text{H}_3^+$  reacting with  $\text{O}_2$  [93] or  $\text{OCS}^+$  reacting with  $\text{ND}_3$  [94]. Additionally, molecular ions in ion traps offer the prospect for state-selected reaction studies. Molecular ions in the rovibrational ground state can be produced by optical pumping, which has first been demonstrated for  $\text{MgH}^+$  ions [95] and  $\text{HD}^+$  [96] ions in two consecutive publications. Another possibility is to produce the molecular ions directly in the desired state, which can be achieved by resonance-enhanced multiphoton ionisation (REMPI) using suitable intermediate states. This has been demonstrated in our group for  $\text{N}_2^+$  ions [97, 98].

Another promising candidate for state-selected generation using REMPI are molecular oxygen ions [99, 100] and experiments in this direction are presented in chapter 4.  $\text{O}_2^+$  ions are of interest due to their importance in the chemistry of the upper atmosphere of our planet [101]. The re-neutralisation reaction of  $\text{O}_2^+$  with Cs is already well studied [102–104]. Direct comparison with previous experiments of  $\text{N}_2^+$  ions and Rb atoms [72] is also of interest. Contrary to  $\text{N}_2^+$  ions, reactions of  $\text{O}_2^+$  ions with Rb atoms in the ground state were expected to be slow, due to an energy mismatch in

the involved energy levels of the entrance and product channels (see Fig. 4.13). It was thus expected to see an enhancement of the reaction rate for vibrationally excited  $O_2^+$  ions.



# Chapter 2

## Introduction - Theory and General Methods

This chapter is the foundation of this work, where the theory behind the processes studied and methods used in the experiments are introduced. The main focus of this work was studying reactions between neutral and charged particles with increased control over the reaction conditions. The theoretical framework of ion-neutral collisions will be introduced in the first section 2.1. Section 2.2 introduces the theory behind the interaction of light and matter. Presented are the methods used to cool ions and atoms. The generation of molecular ions by photoionisation is also discussed. In Section 2.3, the magneto-optical trap used to generate a cloud of cold rubidium atoms will be presented and Section 2.4 introduces the theory behind trapping ions in radio-frequency ion traps. In Section 2.5 some aspects of the combination of the two traps presented in the previous sections will be discussed. The chapter is concluded by introducing a scheme for the determination of the vibrational states of molecular oxygen ions after loading.

### 2.1 Ion-Neutral Collisions

Collisions between charged and neutral particles play an important role in chemistry in dilute gaseous media. Examples include the upper atmosphere of our own planet [101] or gas clouds in the inter-stellar medium [105]. These ion-neutral processes often feature universal behaviour and are usually exothermic with no barriers. They generally mostly depend on the long-range part of their interaction potential. In this section, the theory behind ion-neutral collisions will be briefly laid out.

First, the classical capture model for structureless particles is introduced, leading to the formulation of the temperature-independent Langevin rate constant for charge - induced dipole collisions. Also mentioned are charge - permanent quadrupole interactions, which can lead to an enhancement of the reaction rate. The section is concluded with the introduction of quantum-mechanical effects in cold collisions.

#### 2.1.1 Classical Capture Model

The classical capture model assumes the collision of two structure-less particles in free space, unperturbed by their environment. The capture model assumes that the two particles react with each other with unit probability for all trajectories with enough

energy to overcome centrifugal barriers in the effective interaction potential [106]. To start, consider two particles with relative velocity  $v$  and distance  $R$ , as shown in figure 2.1 a). The distance between the particles perpendicular to the velocity vector is called impact parameter  $b$ .

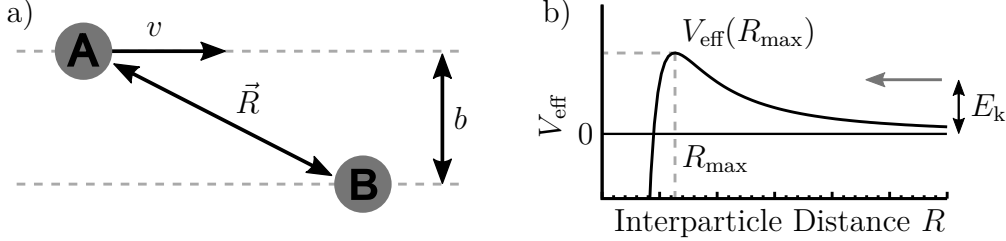


Figure 2.1: a) The definitions of relative velocity  $v$ , distance  $R$  and impact parameter  $b$  when two structure-less particles A and B approach each other are shown. b) A plot of the effective potential  $V_{\text{eff}}$  of two particles interacting at kinetic energy  $E_k$ . The bump in the potential is referred to as centrifugal barrier.

The total energy of the system in absence of a force is given by [106] as

$$E_T = \frac{\mu}{2} \left( \frac{dR}{dt} \right)^2 + \frac{E_T b^2}{R^2} \quad (2.1)$$

which links the energy before the collision at  $R = -\infty$  to finite values of  $R$ . At first the energy is dominated by the kinetic energy, but at small values of  $R$ , the second term due to the rotation of  $\vec{R}$  gains importance, which manifests itself as the centrifugal term  $E_T b^2 / R^2$  in equation (2.1).

In the presence of a force, the interaction potential  $V(R)$  responsible for the force can simply be added to equation (2.1) to read

$$E_T = \frac{\mu}{2} \left( \frac{dR}{dt} \right)^2 + \frac{E_T b^2}{R^2} + V(R). \quad (2.2)$$

The interaction potential and centrifugal barrier can be added together to an effective potential of the form

$$V_{\text{eff}} = \frac{E_T b^2}{R^2} + V(R), \quad (2.3)$$

which will always have a maximum if the potential  $V(R)$  is proportional to  $R^{-s}$  for  $s \geq 3$ . This maximum is known as the centrifugal barrier and it increases as  $b$  increases. Figure 2.1 b) shows a plot of a model effective potential with a centrifugal barrier. There exists a maximum value for  $b$  known as  $b_{\text{max}}$  for every collision energy where the centrifugal barrier is equal to the collision energy.

At values of  $b > b_{\text{max}}$ , the particles will not get to short internuclear distances, where at  $b < b_{\text{max}}$ , they do. Because of the cylindrical symmetry of the problem, this defines a collision cross section  $\sigma = \pi b_{\text{max}}^2$ . Multiplying the cross section  $\sigma$  with the velocity  $v$  results in the rate constant  $k = \sigma v$ .

### 2.1.2 Relevant Interaction Potentials

Depending on the identity of the collision partners, the interaction potential  $V(R)$  takes different forms, where the long-range part of the potential can be described by

$$V(R) = \sum_{n=1}^{\infty} \frac{C_n}{R^n}, \quad (2.4)$$

where  $C_n$  are the long-range coefficients. For this work, the relevant coefficients are  $C_3$  for the *charge*  $\leftrightarrow$  *permanent-quadrupole* interaction and  $C_4$  for the *charge*  $\leftrightarrow$  *induced-dipole* interaction. The two coefficients are given by [1, 107] as

$$C_3^{\text{elst}} = (-1)^{l+\Lambda} \begin{pmatrix} l & 2 & l \\ -\Lambda & 0 & \Lambda \end{pmatrix} \langle l || Q_2 || l \rangle, \quad (2.5)$$

$$C_4^{\text{ind}} = -\frac{1}{2} \left( \alpha_0 + \frac{3\Lambda^2 - 6}{6} \alpha_2 \right). \quad (2.6)$$

For these formulae,  $l$  and  $\lambda$  are the neutral particle's orbital angular momentum and its projection on the collision axis, the bracketed arrays in equation (2.5) are Wigner  $3j$  symbols,  $\langle l || Q_2 || l \rangle$  is the reduced matrix element of the quadrupole moment of the neutral particle and  $\alpha_0$  and  $\alpha_2$  are the scalar and tensor components of the electric dipole polarisability of the neutral particle for a given quantum state.

### 2.1.3 Langevin Collision Rate

For the simple case of collisions between charged particles and neutral particles with zero orbital angular momentum  $l$ , the relevant long-range coefficient is  $C_4$ , since there is no charge permanent-quadrupole interaction and usually interactions with  $n > 4$  can be ignored. For  $l = 0$ ,  $\alpha_2$  is negligibly small, thus combining equations (2.4) and (2.6) results in a potential of the form

$$V(R) = -\frac{\alpha_0}{2R^4}. \quad (2.7)$$

Inserting this into equation (2.2) and solving for  $b_{\text{max}}$ , the so-called Langevin cross-section  $\sigma_L$  can be calculated. The name originates from Paul Langevin, a pioneer in the work on ion-neutral collisions [108].  $\sigma_L$  in this case is found as

$$\sigma_L = \pi \left( \frac{2\alpha_0}{E_T} \right)^{1/2}, \quad (2.8)$$

which can be written as the Langevin rate constant  $k_L$  as

$$k_L = 2\pi \left( \frac{\alpha_0}{\mu} \right)^{1/2}. \quad (2.9)$$

This gives a theoretical collision rate for ion-neutral reactions which is not dependent on the collision energy.

### 2.1.4 Extension to Quadrupol-Ion Interaction

If the collision involve neutral particles in an electronic state with orbital angular momentum  $l = 1$ , then not only the  $C_4$ , but also the  $C_3$  is expected to have a significant effect at long range. Laser cooling of rubidium (see section 2.2.4) involves the first excited state  $^2P_{3/2}$  with orbital quantum number  $l = 1$ , i.e. the Langevin collision rate is not applicable, but needs to be extended to also include charge-permanent quadrupole interactions. The derivation of a rate constant including this “extended” interaction potential was done by Felix Hall [1] and his work and the important results shall be briefly summarised in this section.

For a collision involving a neutral particle with orbital angular momentum  $l = 1$ , the interaction potential is formulated as

$$V(R) = \frac{C_3^{\text{elst}}}{R^3} + \frac{C_4^{\text{ind}}}{R^4}, \quad (2.10)$$

where the  $C_3$  coefficient according to equation (2.5) contains a reduced matrix element. Reformulating this for a single electron atom (ignoring spin-orbit interactions) in terms of modified spherical harmonics, one finds for  $l = 1$  with its projections  $\lambda = 0$  and  $\lambda = 1$  to relate to two symmetries of  $\Sigma$  and  $\Pi$ , respectively, with which a  $p$  orbital can approach the ion. Collisions in  $\Sigma$  symmetry lead to an attractive interaction, whereas collisions in  $\Pi$  symmetry lead to a repulsive interaction. These cases have to be treated separately to calculate the collision rate constant. Additionally, the tensor polarisability  $\alpha_2$  in  $C_4$  may not be negligibly small for  $l = 1$ .

The evaluation of the  $C_3$  terms requires the calculation of the square of the mean radius of the valence electron, which was calculated within the single electron approximation using the quantum defect method. From this, interaction potentials for ion-neutral collisions with a neutral in an electronic state with  $l = 1$  can be formulated. The evaluation of the collision rate constant in these systems can then be done numerically, for which a script was written by Felix Hall. Contrary to the Langevin rate constant derived in the previous section, the collision rate constant obtained with this “extended” potential has an energy dependence, which is proportional to  $E^{-1/6}$ .

### 2.1.5 Quantum-Mechanical Effects

At the lowest collision energies observable in the experiments presented in this thesis, quantum mechanical effects in the form of so-called shape resonances are expected to become important [78]. In an effective potential as shown in Fig. 2.1 b), quasi-bound states can exist above the asymptotic energy behind the centrifugal barrier. If the energy of an incoming particle matches this quasi-bound state, the particles wave function can be dynamically trapped behind the centrifugal barrier. This results in a large amplitude of the scattering wave function at short internuclear distances, where reactions take place, resulting in an increased cross section.

Shape resonances have for example been observed in the Penning ionisation of  $H_2$  and Argon atoms by metastable Helium atoms inside a merged-beam apparatus [109]. In these systems, shape-resonances are comparably wide (tens of millikelvin) due to the light masses of the reaction partners involved. Their results also highlight how the position and width of shape resonances can be used to verify calculated potential energy surfaces. Systems studied on our experiment have all involved reaction partners

with higher masses, where shape resonances start to occur at lower collision energies and are also much more narrow and thus harder to observe.

Calculations on the Ca + Rb<sup>+</sup> system predict several shape resonances below 100 mK [78], which so far have not been observed in experiments. Previous reaction studies on our experiment have been limited to lowest average kinetic energies of around 20 mK and collision energy resolution worse than that [65, 75], preventing the measurement of reaction rate enhancements due to shape resonances. The shuttling atom trap tries to address the problem of poor control over the collision energy and is discussed in chapter 3.

## 2.2 Light-Matter Interaction

The interaction of light with matter is the starting point of many of the techniques used in this thesis. Light is used to cool ions and atoms down to temperatures well below 1 K. In the case of neutral atoms, it also provides part of the trapping force, together with the magnetic field. Further, light is also used to ionise molecular ions in a controlled way.

This section introduces light-matter interaction, starting with the two-level system and introducing the steady state populations. Then light forces are introduced, which are then used to explain Doppler laser cooling. The energy levels involved in Doppler cooling of calcium ions and rubidium atoms are discussed and the section is concluded with the explanation of the photo-ionisation spectrum of the O<sub>2</sub> <sup>1,3</sup>Φ states.

### 2.2.1 Two-Level System

An important quantity to know is the steady state populations of atoms in a (near-) resonant light field. Starting from semi-classical theory of light-matter interaction, working through Rabi oscillations and optical Bloch equations [110], the excited state population of a two-level system is found to be

$$\rho_{ee} = \frac{\Omega_{\text{R}}^2}{\Gamma^2 + 4\delta^2 + 2\Omega_{\text{R}}^2}, \quad (2.11)$$

where  $\Omega_{\text{R}} = d_{\text{eg}} \cdot \mathbf{E}_0 / \hbar$  is the Rabi frequency with the transition dipole matrix element  $d_{\text{eg}}$  and the electric field amplitude  $\mathbf{E}_0$  and  $\Gamma = 1/\tau$  is excited state decay rate, the inverse of the excited state lifetime  $\tau$ . The detuning  $\delta = \omega_{\text{eg}} - \omega$  is the difference between the resonance transition frequency  $\omega_{\text{eg}}$  and the frequency of the light field  $\omega$ , as shown in Figure 2.2.

Equation (2.11) can be simplified by introducing the saturation intensity defined as

$$I_{\text{S}} = \frac{\hbar\Gamma\omega_{\text{eg}}^3}{12\pi c^2}, \quad (2.12)$$

where  $c$  is the speed of light in vacuum. From the saturation intensity, one can define the saturation parameter  $S_0$  using the intensity  $I$  of the light field as

$$S_0 = \frac{I}{I_{\text{S}}} = \frac{2\Omega_{\text{R}}^2}{\Gamma^2}, \quad (2.13)$$

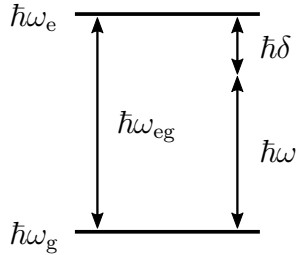


Figure 2.2: A model two-level system with ground state  $g$  at energy  $\hbar\omega_g$  and excited state  $e$  at energy  $\hbar\omega_e$  with a difference in energy of  $\hbar\omega_{eg}$ , driven by a light field of frequency  $\omega$  and detuning  $\delta$ .

which can be used to rewrite the steady-state solution of the excited state fraction as

$$\rho_{ee} = \frac{S_0/2}{1 + S_0 + \left(\frac{2\delta}{\Gamma}\right)^2}, \quad (2.14)$$

which approaches  $\frac{1}{2}$  for increasing intensity.

For the  $5s\ ^2S_{1/2} \rightarrow 5p\ ^2P_{3/2}$  transition in  $^{87}\text{Rb}$  equation (2.12) results in a theoretical value for the saturation intensity of  $I_S = 1.66\ \text{mW}/\text{cm}^2$  using circularly polarised light [111] ( $I_S = 3.58\ \text{mW}/\text{cm}^2$  for light with isotropic polarisation). Experiments where the excited state fraction of rubidium in a magneto-optical trap were measured directly revealed that a value of  $I_S = 9.2 \pm 1.7\ \text{mW}/\text{cm}^2$  better reproduces experimentally measured parameters [112], so this value for the saturation intensity was used in the atom number determination method introduced in section 2.3.3.

The photon scattering rate  $\Gamma_{\text{Ph}}$  is the product of the excited state population  $\rho_{ee}$  and the excited state decay rate  $\Gamma$ :

$$\Gamma_{\text{Ph}} = \rho_{ee}\Gamma. \quad (2.15)$$

These formulae will be important for the description of the properties of the magneto-optical trap introduced in section 2.3.

## 2.2.2 Light Forces

Another important aspect in light-matter interaction is the force a photon can exert onto an atom. A photon possesses a momentum  $\hbar k$ , where the angular wavenumber  $k$  is related to the light's wavelength  $\lambda$  by  $k = 2\pi/\lambda$ .

The scattering force  $F$  can be calculated as

$$F = \hbar k \Gamma_{\text{Ph}}, \quad (2.16)$$

and since the photon scattering rate  $\Gamma_{\text{Ph}}$  saturates at  $\Gamma/2$ , the maximum of this force is

$$F_{\text{max}} = \frac{\hbar k \Gamma}{2}. \quad (2.17)$$

Thus the maximum acceleration is

$$a_{\text{max}} = \frac{F_{\text{max}}}{m} = \frac{\hbar k \Gamma}{2m} = v_r \frac{\Gamma}{2}, \quad (2.18)$$

where  $v_r$  is the recoil velocity

$$v_r = \frac{\hbar k}{m}. \quad (2.19)$$

### 2.2.3 Doppler Laser Cooling

The light forces presented in the previous section can be used to change the momentum of particles, where if the average momentum of a particle is reduced, cooling can be achieved. Since a single photon's momentum is minuscule compared to the momentum of particles to be cooled, many such photons need to be scattered to change the particle's momentum considerably. In order to scatter many photons, the particles need a closed cycle of absorption and emission, limiting the possibility of laser cooling to species with simple energy level structures and thus mostly to atoms.

The laser-cooled species in this work are singly charged calcium ions and neutral rubidium atoms, the energy level structures of which are discussed in section 2.2.4. In recent years, progress has been made towards laser cooling of simple two-atomic molecules, such as SrF [86,87], YO [88] or CaF [89,90], and even the first cooling of the tri-atomic species SrOH has been reported [91].

To achieve cooling using light forces, the forces acting on the particles must be velocity dependent and dissipative, so that the particles are cooled more than they are heated. A simple way this can be achieved is by exploiting the physics of the Doppler effect. The resulting Doppler laser cooling technique was proposed in two independent papers by Hänsch and Schawlow [7] as well as Wineland and Dehmelt [8] in 1975 and will be introduced below.

In Doppler laser cooling, a red-detuned cooling laser is used. Atoms moving against the laser beam direction will see the frequency of the laser shifted towards resonance and scatter photons. This process slows them down, because the momentum gain from spontaneous emission happens in all spatial directions and averages out over time, as is sketched in Figure 2.3.

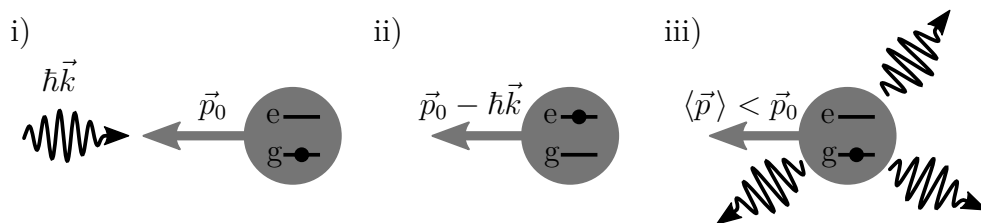


Figure 2.3: The principle of Doppler laser cooling. In i), a photon with momentum  $\hbar\vec{k}$  of a light field propagating opposite a particle with initial momentum  $\vec{p}_0$  gets absorbed. ii) The absorbed photon excites the particle from ground state  $g$  to the excited state  $e$  and the particles momentum is reduced by an amount equal to the photons momentum. Finally in iii) the particle relaxes back to its ground state by emitting a photon in a random direction. This cycle is continuously driven resulting in a reduction in velocity of the particle opposite the propagation direction of the light field.

Consider a light field of a running wave with wave vector  $k$ , frequency  $\omega$  and detuning  $\delta_0$  and an atom with momentum  $p$  at velocity  $v$  opposing the direction of the laser field as sketched in Figure 2.3. The zero velocity detuning from the atomic

transition at frequency  $\omega_{eg}$  is given as  $\delta_0 = \omega - \omega_{eg}$  and the total detuning including the Doppler effect is  $\delta = \delta_0 - kv$ . Equation (2.16) thus reads as

$$F = \hbar k \Gamma_{\text{Ph}} = \frac{\hbar k \Gamma}{2} \cdot \frac{S_0}{1 + S_0 + 2 \left( \frac{\delta_0 - kv}{\Gamma} \right)^2}. \quad (2.20)$$

A Taylor expansion of First order can be made around  $v = 0$  for small  $v$ , the result of which is

$$F \approx F_0 - \beta v, \quad (2.21)$$

where  $\beta$  is the damping coefficient:

$$\beta = -\hbar k^2 \frac{4S_0 \left( \frac{\delta_0}{\Gamma} \right)}{\left[ 1 + S_0 + 4 \left( \frac{\delta_0}{\Gamma} \right)^2 \right]^2} \quad (2.22)$$

and  $F_0$  is a term corresponding to constant acceleration.

For red detuning at  $\delta_0 < 0$  (i.e. laser frequency set to below transition frequency) the damping coefficient is positive, leading to damping of  $v$  and thus a cooling effect. Velocity-dependence is also fulfilled, since as the velocity  $v$  decreases, the force acting on the particles is also reduced. But due the term  $F_0$  in equation (2.21), a force is acting on the particles even once they are slowed down to a stop, thus leading to an acceleration in the opposite direction.

This can be prevented using counter-propagating laser beams, such that the force in equation (2.20) now reads

$$F_{\pm} = \hbar k \Gamma_{\text{Ph}} = \frac{\hbar k \Gamma}{2} \cdot \frac{S_0}{1 + S_0 + 2 \left( \frac{\delta_0 \pm kv}{\Gamma} \right)^2}. \quad (2.23)$$

In this case, the term  $F_0$  in the Taylor expansion cancel out and give

$$F \approx -\beta v \quad (2.24)$$

with

$$\beta = 8\hbar k^2 \frac{S_0 \delta_0}{\left[ 1 + S_0 + 4 \left( \frac{\delta_0}{\Gamma} \right)^2 \right]^2}. \quad (2.25)$$

This is now a purely velocity-dependent force and this configuration represents the one-dimensional optical molasses, resulting in damping along the axis of the counter-propagating laser beams. To achieve cooling in all three spatial dimensions, three orthogonal counter-propagating laser beams need to be overlapped, resulting in a three-dimensional optical molasses configuration, the first experimental demonstration of which was achieved by S. Chu and co-workers in 1985 [18]. Even though the density of atoms might be increased locally at the intersection of the three laser beams, the atoms are not trapped. There is no restoring force and the atoms are free to drift out of the laser beams.

One possibility of trapping particles is the addition of a quadrupolar magnetic field, which can add a restoring force and thus provide trapping. This setup, where the light and magnetic field together are providing the trapping, is called a magneto-optical trap and is introduced in section 2.3. For charged particles, ion traps can provide trapping independent of the light field and are introduced in section 2.4.

There is a limit to the temperature that can be reached using Doppler laser cooling, set by the recoil velocity of single photons spontaneously emitted in the process. The residual motion due to these random spontaneous emission events is the Doppler cooling limit and gives an estimate for the Doppler temperature  $T_D$  as the lowest temperature reachable in an optical molasses configuration [110] as

$$k_B T_D = \frac{\hbar\Gamma}{2}. \quad (2.26)$$

## 2.2.4 Laser Cooling in $\text{Ca}^+$ and Rb

The two species laser cooled in this work are singly charged calcium ions and neutral rubidium atoms. Both species possess a single electron in the outer-most shell, leading to a simple energy level structure. A schematic of the energy levels involved in laser cooling of both species is shown in Figure 2.4.

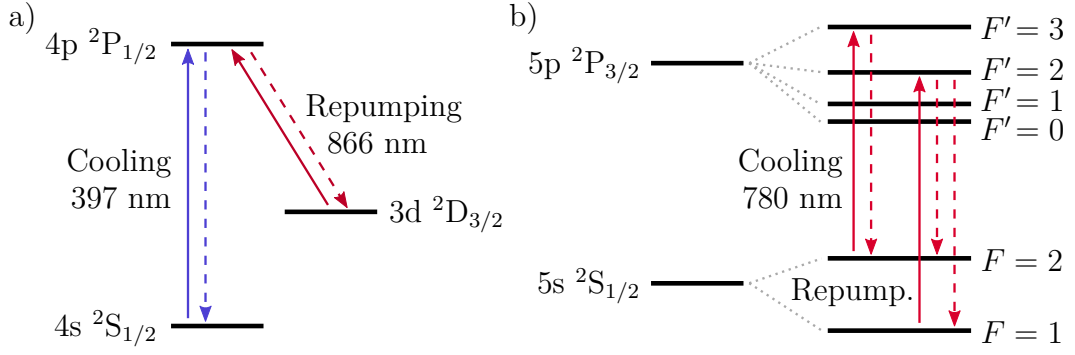


Figure 2.4: Energy levels involved in the laser cooling of a) singly charged calcium ions and b) neutral rubidium atoms. Solid arrows indicate absorption and dashed arrows indicate spontaneous emission.

Doppler laser cooling in calcium ions is achieved by driving the  $4s\ ^2S_{1/2} \rightarrow 4p\ ^2P_{1/2}$  transition at around 397 nm. At a lower probability, the  $4p\ ^2P_{1/2}$  level can also spontaneously decay to the metastable  $3d\ ^2D_{3/2}$  level. In order to reintroduce the ions into the cooling cycle, the ions need to be repumped on the  $3d\ ^2D_{3/2} \rightarrow 4p\ ^2P_{1/2}$  transition at around 866 nm.

In rubidium the  $5s\ ^2S_{1/2}$  ( $F = 2$ )  $\rightarrow$   $5p\ ^2P_{3/2}$  ( $F' = 3$ ) transition is used for Doppler laser cooling. Atoms off-resonantly excited to the  $5p\ ^2P_{3/2}$  ( $F' = 2$ ) level can decay to the  $5s\ ^2S_{1/2}$  ( $F = 1$ ) level, which is not addressed by the cooling laser. Since the two hyperfine levels in the ground state are only separated by approximately 6.8 GHz, an electro-optical modulator (EOM) generating sidebands at this frequency can provide repumping.

In the excited state  $5p\ ^2P_{3/2}$  of rubidium, a single 397 nm photon of the calcium cooling laser is enough to ionise the rubidium atom. To avoid this, the laser cooling light for the calcium ions and rubidium atoms are never present simultaneously.

## 2.2.5 Photoionisation of $\text{O}_2$ Using the $1,3\Phi$ States

The  $3d\delta\ ^{1,3}\Phi$  Rydberg states in molecular oxygen were described by Chupka and co-workers in two-photon resonant excitations from either the  $X\ ^3\Sigma_g^-$  ground state [113]

or the metastable  $a^1\Delta_g$  state [114] in molecular oxygen. In a follow-up paper, they use these states to generate molecular oxygen ions in a desired vibrational state with very high fidelity [99]. To be able to use these states for the generation of vibrationally state-selected molecular oxygen ions, one needs to measure and understand their spectrum. The structure of the spectra arise due to the different angular momentum couplings in ground and excited state and selection rules in the excitation scheme used.

**Hund's Coupling Cases** Hund's coupling cases describe different possible coupling hierarchies in the coupling of the various angular momenta present in molecules. There are a five cases usually denoted case a through e. Since only case a and b are relevant for the two states involved in the transitions presented here, these two cases shall be introduced here.

In Hund's case a, the nuclear rotation is coupled weakly to the electronic angular momentum, but the two electronic angular momenta (spin and orbital angular momentum) are coupled strongly to the internuclear axis. The projection of the orbital angular momentum  $\vec{L}$  and the projection of the spin angular momentum  $\vec{S}$  couple to the total electronic angular momentum  $\vec{\Omega}$ .  $\vec{\Omega}$  then couples to the rotational angular momentum  $\vec{R}$ , forming the resulting total angular momentum  $\vec{J}$ . A schematic of this coupling is shown in Figure 2.5 a).

In Hund's case b, the vector  $\vec{S}$  is not coupled to the internuclear axis. The coupling is as follows: the projection of the orbital angular momentum  $\vec{L}$  on the internuclear axis called  $\vec{\Lambda}$  couples to the rotational angular momentum  $\vec{R}$ , leading to the total angular momentum without spin  $\vec{N}$ .  $\vec{N}$  can then couple with the spin angular momentum  $\vec{S}$  to form the total angular momentum  $\vec{J}$ . A schematic of this coupling is shown in Figure 2.5 b).

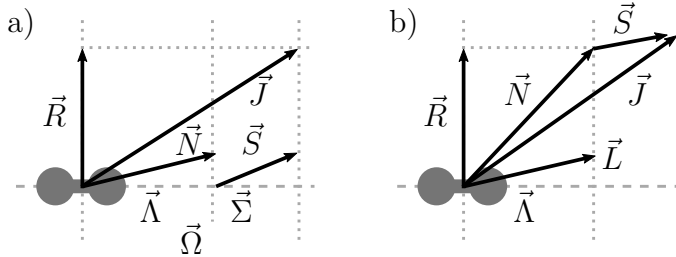


Figure 2.5: Vector diagrams of Hund's cases a and b.

- a) Hund's case a. The coupling hierarchy is first  $\vec{\Omega} = \vec{\Lambda} + \vec{\Sigma}$  and then  $\vec{J} = \vec{\Omega} + \vec{R}$ .  
 b) Hund's case b. The coupling hierarchy is first  $\vec{N} = \vec{\Lambda} + \vec{R}$  and then  $\vec{J} = \vec{N} + \vec{S}$ .

**Ground State of  $O_2$**  The ground state of molecular Oxygen is a  $^3\Sigma_g^-$  state and follows Hund's coupling case b (first  $\vec{N} = \vec{\Lambda} + \vec{R}$  and then  $\vec{J} = \vec{N} + \vec{S}$ ). Since the ground state of oxygen is a  $\Sigma$ -state,  $\vec{\Lambda}$  is zero and thus  $\vec{N} = \vec{R}$ . The total angular momentum is then given as  $\vec{J} = \vec{N} + \vec{S}$ . Oxygen is a homonuclear diatomic molecule with total nuclear spin  $I = 0$ , so every other rotational level is missing due to exchange symmetry and only levels with  $N$  odd exist, with positive parity.  $S$  can be 1, 0 or  $-1$ , leading to three different total angular momenta  $J$  per rotational level:

$J = N + 1, N$  and  $N - 1$ , denoted the  $F_1, F_2$  and  $F_3$  levels, respectively. An overview of the first rotational levels and resulting total angular momentum  $J$ , split up by the  $F_i$  components, is shown on the left side of table 2.1.

With molecular oxygen being a triplet state, the spin-spin interaction has to be considered as well. Given by Herzberg [115], the energies of the  $F$ -states can be approximated by

$$\begin{aligned} F_1 &= B_\nu N(N + 1) - \frac{2\lambda(N + 1)}{2N + 3} + \gamma(N + 1) \\ F_2 &= B_\nu N(N + 1) \\ F_3 &= B_\nu N(N + 1) - \frac{2\lambda N}{2N - 1} - \gamma N, \end{aligned} \tag{2.27}$$

where  $B_\nu$  is the rotational constant of the vibrational state  $\nu$  and for  $\nu = 0$  given as  $B_0 = 1.438 \text{ cm}^{-1}$ ,  $\gamma = -0.0084 \text{ cm}^{-1}$  is the spin-rotation coupling constant and  $\lambda = 1.984$  is the spin-spin coupling constant.

**Excited State of  $\text{O}_2$**  The measured excited states of molecular Oxygen are  $^1,^3\Phi_g$  Rydberg states and follow Hund's coupling case a (first  $\vec{\Omega} = \vec{\Lambda} + \vec{\Sigma}$  and then  $\vec{J} = \vec{\Omega} + \vec{R}$ ). The  $\Phi$  states measured were only triplet states, i.e.  $\Sigma = 1, 0$  or  $-1$  and  $\Lambda$  in case of a  $\Phi$  state is equal to 3. So there are 3 total electronic angular momenta quantum numbers  $\Omega = 2, 3$  and 4 possible. The measured states had  $\Omega = 2$  and 3, meaning total angular momentum levels of  $J = 2, 3, 4, \dots$  for  $^3\Phi_2$  and  $J = 3, 4, 5, \dots$  for  $^3\Phi_3$  are possible.

As stated in [114], the rotational energies in the  $^3\Phi_3$  and  $^3\Phi_2$  states do not follow the usual expression

$$T + BJ(J + 1) - DJ^2(J + 1)^2, \tag{2.28}$$

but are better fit by

$$T + \gamma J + BJ(J + 1), \tag{2.29}$$

indicating that there are energy level shifts proportional to  $J$ . The values for the constants are also given in reference [114].

**Expected Transitions** In transitions from the  $^3\Sigma_g^-$  ground state to the  $^3\Phi$  states the orbital angular momentum quantum number  $\Lambda$  changes by 3, meaning these transitions are nominally forbidden, since they violate the selection rule for change in the orbital angular momentum quantum number of  $\Delta\Lambda \leq 2$  in two-photon transitions [113]. They become allowed because of an  $l$ -uncoupling interaction with the nearby, allowed  $^1,^3\Delta$  complex [113].

Expected  $J$  levels in the ground state of oxygen and levels reached in the excited state of the O-, P-, Q-, R- and S-branch are shown in table 2.1. The corresponding energy levels in the ground and excited state have been calculated and by subtracting the appropriate ground state level energy (up to  $R = 17$ ) from the excited state level energy, the different transition energies have been calculated.

In this manner, a total of 123 transitions to the  $^3\Phi_2$  and 116 transitions to the  $^3\Phi_3$  state have been calculated per vibrational level, totalling to 717 calculated line positions. A plot of the calculated line positions together with the measured spectra can be found in section 4.2.1.

Table 2.1: The expected levels in the ground state of molecular oxygen, separated for the different spin-rotation components  $F_i$ . On the right, the expected  $J$  levels reached in the excited state for the O-, P-, Q-, R- and S-branch are shown. The red  $J$  levels, namely 0 and 1, do not exist for the  ${}^3\Phi_2$  state and the red and green  $J$  levels, namely 0, 1 and 2, do not exist in the  ${}^3\Phi_3$  state.

spin-rotation component	$N = R$	$J = N + S$	O	P	Q	R	S
	1	2	0	1	2	3	4
$F_1 (S = 1)$	1	2	0 <sup>†</sup>	1	2	3	4
$F_1 (S = 1)$	3	4	2	3	4	5	6
	5	6	4	5	6	7	8
	⋮	⋮	⋮	⋮	⋮	⋮	⋮
	1	1	-	0	1	2	3
$F_2 (S = 0)$	3	3	1	2	3	4	5
	5	5	3	4	5	6	7
	⋮	⋮	⋮	⋮	⋮	⋮	⋮
	1	0	-	-	0	1	2
$F_3 (S = -1)$	3	2	0	1	2	3	4
	5	4	2	3	4	5	6
	⋮	⋮	⋮	⋮	⋮	⋮	⋮

## 2.3 Magneto-Optical Trap

The optical molasses technique introduced in section 2.2.3 can be used to cool particles, but the particles are not actually trapped. To trap the particles, an additional position-dependent force needs to be implemented which pushes all the atoms towards a point in space. A position-dependent force can be added with the overlap of an quadrupolar magnetic field onto the light field, resulting in a magneto-optical trap (MOT), which will be described in this section. Figure 2.6 shows a schematic of this setup.

### 2.3.1 Operation Principle

To understand the operation principle behind a magneto-optical trap, a sketch of the position dependence on the energy level structure of a particle with a transition  $F = 0 \rightarrow F' = 1$  inside an inhomogeneous magnetic field is shown in Figure 2.7. Due to the increase in magnetic field when the particle moves away from the trap center, the Zeeman splitting in the excited state increases. This increase in splitting in the excited state moves the transition closer to the frequency of the light field  $\omega$  at detuning  $\delta$  when the particle leaves the trap center.

Selection rules only allow  $\Delta M = +1$  for  $\sigma+$  polarisation and  $\Delta M = -1$  for  $\sigma-$  polarisation. This introduces an imbalance in the scattering rate from the two beams when the atom leaves the trap center and thus adds a restoring force towards the trap center. For example, consider an atom moving left in Figure 2.7, which moves the  $M_g = 0 \rightarrow M_e = +1$  transition (subscripts g and e referring to ground and excited state, respectively) closer to resonance with the light field at frequency  $\omega$  and thus

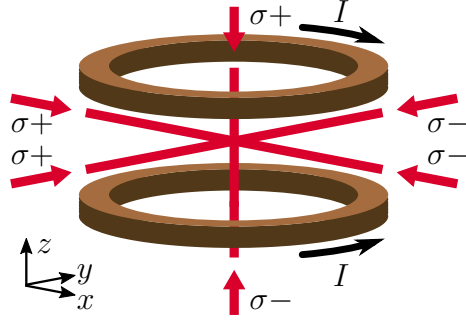


Figure 2.6: Basic setup of a standard magneto-optical trap. Two coils in orange in anti-Helmholtz configuration (where the current  $I$  runs in opposite directions) generate a quadrupolar magnetic field. At the center of the quadrupolar magnetic field, 3 pairs of counter-propagating beams are overlapped in an optical-molasses configuration where each pair consists of beams with opposite circular polarisations  $\sigma+$  and  $\sigma-$ .

makes the atom more likely to absorb a photon from the beam with  $\sigma+$  polarisation from the left, pushing the atom back towards the trap center.

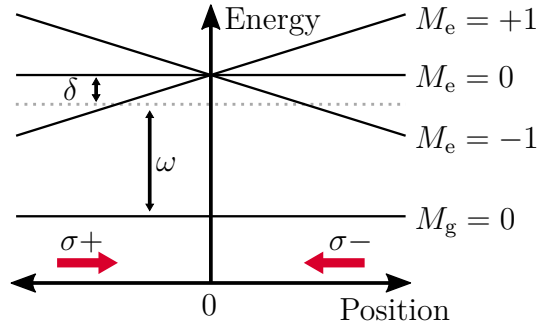


Figure 2.7: Energy level diagram of a simple model MOT with no Zeeman splitting in the lower level. In the excited upper state, Zeeman splitting to  $M_e = -1, 0, 1$  happens with increasing distance from the trap center, because of the increasing magnetic field. The magnetic field increases linearly with position.

Because of the splitting of the Zeeman levels of the particles in the excited state, equation (2.23) now reads

$$F_{\pm} = \frac{\hbar k \Gamma}{2} \cdot \frac{S_0}{1 + S_0 + \left(\frac{2\delta_{\pm}}{\Gamma}\right)^2}, \quad (2.30)$$

where the new detuning  $\delta_{\pm}$  is given as

$$\delta_{\pm} = \delta_0 \mp kv \pm \frac{\mu' B}{\hbar}. \quad (2.31)$$

The term  $\pm \frac{\mu' B}{\hbar}$  is responsible for the position dependency of the force, due to the increase in magnetic field  $B$  as the particles move away from the trap center with

$$\mu' = (g_e m_e - g_g m_g) \mu_B \quad \text{and} \quad B = A \cdot z, \quad (2.32)$$

where  $\mu_B$  is the Bohr magneton,  $A$  is the magnetic field gradient and subscripts  $g$  and  $e$  refer to the ground and excited states, respectively.

Similarly to working out equation (2.24), the force can be expanded as

$$F \approx -\beta v - \kappa z, \quad (2.33)$$

where  $\beta$  is the same as for optical molasses as in equation (2.25) and  $\kappa$  is given as

$$\kappa = \frac{\mu' A}{\hbar k} \beta. \quad (2.34)$$

This results in there being a position-dependent force as well as a damping force, effectively cooling and trapping the particles with a magnetic field and light.

### 2.3.2 Pushing Atoms with Light

The forces introduced in section 2.2.2, extended to laser cooling in section 2.2.3 and adapted for the MOT in section 2.3.1 can also be utilised to push atoms. Two setups using scattering light forces can be applied to make atoms move: either using counter-propagating laser beams or a single laser beam.

As introduced in section 2.2.3 in equations (2.23) to (2.25), having two counter-propagating laser beams at the same frequency and intensity will result in damping along this axis. Changing the frequency or intensity of one of the two beams creates an imbalance in the scattering force in the two directions, creating a radiation pressure difference. This makes the atom drift along the axis [31], as long as there is no restoring force present. With a restoring force an equilibrium can be reached where the restoring force and the radiation pressure cancel each other, leading to trapping in an off-center position (with respect to the trap center).

Equations (2.20) to (2.22) pertained to the case of a single laser beam. Considering a stationary atom in this setup, the atom gets pushed away from the laser beam source. Using a light frequency resonant with a transition in the atom, the atom will be quickly accelerated, shifting the atom off resonance due to increasing Doppler shift, resulting in a non-linear acceleration.

The shuttling atom trap introduced in chapter 3 makes use of both concepts introduced here. Radiation pressure imbalance in one of the axes due to decrease in intensity of one of the two beams results in trapping the atom cloud in an off-center position. Atoms are shuttled back and forth between two such off-center positions using on-resonance laser beam pulses. The whole process and technical implementation is explained in detail in section 3.1.

### 2.3.3 Atom Number and Density Estimation

After establishing the basic working principle of magneto-optical traps in section 2.3.1, this section will cover how the number of atoms inside the atom cloud and the average density of trapped atoms can be estimated from experimental images taken with an electron-multiplying charged-coupled device (EMCCD) camera.

The method used to determine atom numbers is to calculate the expected number of photons scattered by one atom for a given set of trap parameters and compare it with the total number of photons scattered from the atom cloud, which can be estimated from the number of photons registered by the camera and accounting for

losses due to the imaging system. The total number of photons scattered is divided by the expected number of photons from calculations to yield the total atom number of the cloud. The average density inside the cloud can then be calculated from a geometric analysis of the atom cloud images.

**Atom Number Estimation** Applying this approach, the atom number  $N$  can be calculated as

$$N = \frac{N_{\text{ph}}}{L_{\text{T}} \cdot t_{\text{exp}} \cdot G} \cdot \frac{1}{\Gamma_{\text{Ph}}}, \quad (2.35)$$

where  $N_{\text{ph}}$  is the photon count registered by the EMCCD camera,  $L$  is the total loss factor for the imaging system,  $t_{\text{exp}}$  is the exposure time,  $G$  is the electron-multiplying gain of the camera and  $\Gamma_{\text{Ph}}$  is the calculated photon scattering rate.

The EMCCD camera used to take images of the atom cloud works by counting the number of electrons generated by photons hitting each of the detector's pixels. To determine the number of photons which were registered by the camera that were scattered by the cloud  $N_{\text{ph}}$ , one determines the total number of counts of images of the atom cloud and subtracts the total number of background counts of images where the atom cloud is not present (which is achieved by switching off the magnetic field). Counts in the images without atom cloud come from different sources, such as stray light and dark counts of the EMCCD sensor.

The photon count  $N_{\text{ph}}$  is not the total number of photons scattered by the atom cloud, as losses due to the imaging system need to be considered as well. The loss factor  $L_{\text{T}}$  is the total imaging system loss and the product of geometric factor (i.e. the solid angle registered by the camera), losses due to the imaging system and camera sensitivity. The total imaging system loss  $L_{\text{T}}$  is calculated as

$$L_{\text{T}} = L_1 \cdot L_2 \cdot L_3 \cdot L_4 \cdot L_5 \cdot L_6 \cdot L_7, \quad (2.36)$$

where  $L_1 = 0.451 \pm 0.01$  is the loss due to chopping of the cooling laser beams,  $L_2 = 0.00762 \pm 0.0005$  is the loss due to the solid angle,  $L_3 = 0.93 \pm 0.02$  is the loss due to the view port glass,  $L_4 = 0.098$  is the loss due to the camera sensitivity,  $L_5 = 0.059 \pm 0.02$  is the loss due to the bandpass filter used to isolate the light from the atoms,  $L_6 = 0.84 \pm 0.02$  is the loss due to the microscope optics and  $L_7 = 0.484 \pm 0.05$  is the loss due to the PMT beam splitter cube inside the microscope. The total imaging system loss is then found as  $L_{\text{T}} = 7.5 \cdot 10^{-5} \pm 1.0 \cdot 10^{-5}$ .

Two factors are settings dictated by the camera program, which are the exposure time  $t_{\text{exp}}$  and the EM gain factor  $G$ . The gain is generally kept low ( $G \ll 200$ ), where it is behaving linearly. The photon scattering rate  $\Gamma_{\text{Ph}}$  is introduced in equation (2.15), where the excited state population is calculated from measuring the total intensity illuminating the atom cloud as well as the detuning settings.

**Average Atom Density Estimation** The average density of the atom cloud can be calculated assuming the density distribution follows an isotropic Gaussian distribution [116] of the form

$$n(r) = \frac{N}{\pi^{3/2}\omega^3} \exp\left(-r^2/\omega^2\right), \quad (2.37)$$

where  $\omega$  is the  $1/e$  radius of the cloud. The average density  $n_{\text{avg}}$  is found by integration of the product of the probability of an atom being at radius  $r$  and the density at that location, which results in

$$n_{\text{avg}} = \int \frac{n(r)}{N} n(r) dV = \frac{N}{2\sqrt{2}\pi^{3/2}\omega^3}. \quad (2.38)$$

A LabVIEW program was written for the atom number and density analysis, which is able to perform all steps automatically. The program is briefly described in the appendix in section B.4.2.

**Systematic Uncertainties in Atom Number and Density Estimation** The systematic uncertainty in the atom number and density estimation was evaluated using Gaussian error propagation. The uncertainty in scattering rate is a result from errors in laser intensity determination, the large error in saturation intensity (see section 2.2.1) and the estimated error in laser detuning. Uncertainty in the total imaging loss factor is stated above. For the photon counting of the EMCCD camera, a Poisson distribution was assumed, for which the standard deviation was estimated as the square root of the number of counts. An error of 5% was assumed for the radius determination of the atom cloud distribution. This resulted in an estimated relative systematic uncertainty in atom number of around 30 – 35%, which is slightly lower than previous stated uncertainty in atom number on this experiment of 44% [1].

## 2.4 Ion Trapping

In our experiment, a so-called linear Paul trap is used. It consists of 4 parallel rods arranged in a square and each rod is split into 3 segments. According to Earnshaw's theorem, charged particles cannot be confined by electrostatic potentials alone [110]. Because of this, Paul traps make use of a combination of radio-frequency and static potentials to dynamically trap ions. Figure 2.8 shows a schematic drawing of a linear Paul trap and explains the different electrical fields applied to the electrodes of the trap.

### 2.4.1 Equations of Motion

To understand the dynamics of the ions inside a linear Paul trap, the equation of motions are derived. Starting from a three-dimensional potential  $\Phi = \alpha x^2 + \beta y^2 + \gamma z^2$ , the Laplace equation

$$\nabla^2 \Phi = \frac{\partial^2 \Phi}{\partial x^2} + \frac{\partial^2 \Phi}{\partial y^2} + \frac{\partial^2 \Phi}{\partial z^2} = 0 \quad (2.39)$$

needs to be fulfilled, which leads to  $\alpha + \beta + \gamma = 0$ . One way this can be achieved is by setting  $\alpha = \beta = -2\gamma$  resulting in a trapping configuration that is radially symmetric.

The potential along the radial direction is generated by a radio-frequency voltage and takes the form of

$$V(x, y, t) = V_{0,\text{RF}} \left( \frac{x^2 - y^2}{r_0^2} \right) \cos(\Omega_{\text{RF}} t), \quad (2.40)$$

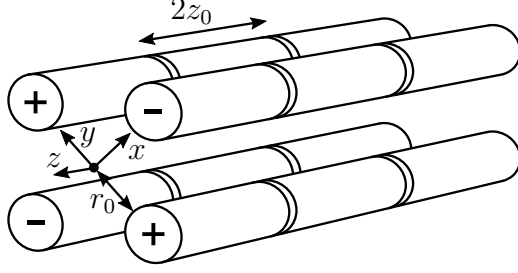


Figure 2.8: Schematic of a linear Paul trap as used in the experiment, which consists of 4 segmented rods arranged in a square pattern. The orientation of the coordinate system used is shown, where  $z$  is aligned along the central axis of the trap and  $x$  and  $y$  are pointing towards the rod centers. The shortest distance from the central trap axis to the surface of the rods is defined as  $r_0$  and the length of the central segment of each rod is defined as  $2z_0$ . To provide confinement radially (in direction of  $x$  and  $y$ ), radio-frequency voltage is applied to all four rods, where the ones labelled with  $+$  are in phase and  $180^\circ$  out of phase with the ones labelled  $-$ . Confinement along the axial direction ( $z$ ) is provided by applying dc voltage to the outer segments of each rod, referred to as endcap electrodes. Additionally, dc voltages can be applied to all 12 segments individually to counteract trap imperfections and optimise the ion position onto the trap axis.

where  $V_{0,\text{RF}}$  is the zero-to-peak amplitude of the applied radio-frequency voltage with frequency  $\Omega_{\text{RF}}$ . The potential along the axial direction due to the applied endcap voltage  $V_{\text{end}}$  is given by:

$$U(x, y, z) = \frac{\kappa V_{\text{end}}}{z_0^2} \left[ z^2 - \frac{1}{2}(x^2 + y^2) \right], \quad (2.41)$$

where  $\kappa$  is an experimentally determined geometrical factor and  $z_0$  is half the distance between the endcap electrodes.

The equations of motions can be derived from Newton's second law,  $F = ma$ , which states that the force  $F$  is the product of mass  $m$  and acceleration  $a$ . A force on a particle with charge  $Q$  by an electrical field  $\mathbf{E}$  is given as  $Q\mathbf{E}$  and the acceleration can be written as the second derivative of the displacement vector  $\mathbf{r}$ , resulting in equation

$$Q\mathbf{E} = m\ddot{\mathbf{r}}. \quad (2.42)$$

This leads to the Mathieu equation describing the motion of a trapped ion as

$$\frac{d^2}{d\tau^2}u + (a_u + 2q_u \cos(\Omega_{\text{RF}}\tau))u = 0, \quad (2.43)$$

with  $u = x, y, z$  and  $\tau = \frac{1}{2}\Omega t$ . The so-called Mathieu stability parameters  $a_u$  and  $q_u$  are given as

$$a_x = a_y = -\frac{1}{2}a_z = \frac{-4\kappa Q V_{\text{end}}}{m\Omega^2 z_0^2}, \quad (2.44)$$

$$q_x = -q_y = \frac{4Q V_{0,\text{RF}}}{m\Omega^2 r_0^2}, \quad q_z = 0. \quad (2.45)$$

For small values of the stability parameters  $|a_u| \ll 1$  and  $|q_u| \ll 1$ , the solution to the Mathieu equations can be approximated as

$$r_u(t) = r_{1u} \cos(\omega_u t + \phi) \left[ 1 + \frac{q_u}{2} \cos(\Omega t) \right]. \quad (2.46)$$

The motion can be seen as the combination of two oscillations, the first a slow, large-amplitude motion at a frequency  $\omega_u$  which is dependent on the mass of the ion. The second motion is a fast, smaller amplitude motion at frequency  $\Omega$  as a direct result of the RF fields acting on the ion.

The frequency of the slower of the two oscillatory motions is described by

$$\omega_u = \frac{1}{2} \Omega \sqrt{a_u + \frac{1}{2} q_u^2} \quad (2.47)$$

and takes different values for the radial and axial secular frequencies.

These secular frequencies are mass-dependent and therefore can be exploited to determine the mass-to-charge ratio of the ionic species inside the ion trap. This so-called resonant excitation mass spectrometry (REMS) works by applying an additional radio-frequency field to one or multiple electrodes of the Paul trap. By scanning the frequency of this field over the expected motional frequencies of ions inside the trap, a relatively crude mass-spectrum can be recorded [117]. The observable used to detect excitation is either a decrease or increase in fluorescence (depending on the laser cooling settings) as the motion of the ions is excited.

The secular motion of the ions is often described within the adiabatic approximation [118] as the motion inside a time-independent pseudopotential  $U_{\text{Pseudo}}$  which is given by [119] as

$$U_{\text{Pseudo}}(r, z) = \frac{1}{2} \omega_r^2 r^2 + \frac{1}{2} \omega_z^2 z^2, \quad (2.48)$$

with

$$\omega_r = \sqrt{a + \frac{1}{2} q^2}, \quad \omega_z = \sqrt{-2a} \quad \text{and} \quad r^2 = x^2 + y^2, \quad (2.49)$$

where  $\omega_r$  and  $\omega_z$  are the effective radial and axial secular oscillation frequencies within the pseudopotential. This appropriately describes the thermal motion of the ions within the trap, but time-dependent effects caused by the oscillating RF field are not included.

## 2.4.2 Coulomb Crystals

With laser cooling of ions inside the ion trap, a phase transition from a diffuse ion cloud to ordered structures called Coulomb crystals is observed. Coulomb crystals are three-dimensional arrangements of the ions. The laser-cooled ions inside the Coulomb crystal fluoresce, enabling the imaging of Coulomb crystals using sensitive electron-multiplying charged-coupled device (EMCCD) cameras attached to a microscope. Figure 2.9 a) shows an image of Coulomb crystal consisting of laser-cooled calcium ions.

For large crystals, a single laser beam for Doppler laser cooling can be enough, since all motional degrees of freedom are coupled by the Coulomb interaction between the ions. When other ions in addition to calcium are loaded into the trap, they are indirectly cooled by their Coulomb interaction with the laser-cooled calcium ions. A Coulomb crystal containing molecular oxygen ions is shown in Figure 2.9 b). The

molecular ions are lighter than the calcium ions and are thus confined more strongly, pushing them towards the trap center. The ionisation laser also produces some heavy ions, which are trapped less strongly and thus form a dark band around the calcium ions.

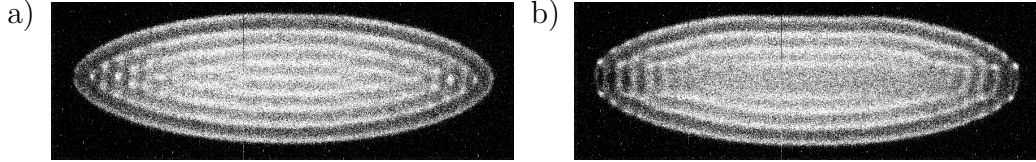


Figure 2.9: Fluorescence images of Coulomb crystals. a) A pure calcium Coulomb crystal. b) After loading molecular oxygen ions into the crystal, a dark core within the crystal appears. Heavy ions form a band around the calcium ions leading to indentations at the top and bottom of the crystal.

## 2.5 Hybrid Trap

The most important aspects in the combination of the magneto-optical trap and the ion trap will be briefly described here. Discussed are the determination of reaction rates and the calculation of the degree of overlap between the atom cloud and the ions. For a description of the experimental setup, see section 3.1.

### 2.5.1 Determination of Reaction Rate Constants

Coulomb crystals are overlapped with the atom cloud and the disappearance of ions is observed with the EMCCD camera. Since there are many more atoms than ions and the atoms are constantly reloaded from background, the reactions follow pseudo-first-order kinetics. The pseudo-first order rate constant is determined by observing the loss of ions over time, where the integrated rate-law is given as

$$\log \frac{V(t)}{V_0} = -k_{\text{pfo}}t. \quad (2.50)$$

Here  $V(t)$  is the volume of the ions after time  $t$ ,  $V_0$  is the volume at the start of reaction and  $k_{\text{pfo}} = n_{\text{avg}}k_{2\text{nd}}$  is the pseudo-first order rate constant which is the product of the average atom density  $n_{\text{avg}}$  and the second-order rate constant  $k_{2\text{nd}}$ .

In order to determine the second-order rate constant  $k_{2\text{nd}}$ , the logarithm of the relative volume loss is plotted against time and a straight line is fitted through the data, giving the pseudo-first-order rate constant as the slope. Dividing  $k_{\text{pfo}}$  by the average atom number  $n_{\text{avg}}$  results in the second-order rate constant  $k_{2\text{nd}}$ .

### 2.5.2 Calculating the Overlap

The ion density within the crystal can be approximately considered constant over the volume of the crystal. This is not given for the atom cloud, which is described by a three-dimensional Gaussian distribution. Using the average density to calculate the second order rate constants would lead to a systematic error. An additional random

error would be incorporated into the measurement because of varying crystal size and position relative to the atom cloud.

To avoid these systematic and random errors, an overlap factor is calculated which scales the overall average density of the atom cloud to the average density sampled by the crystal. This is done by numerically integrating the density distribution over the volume of the crystal to get the number of atoms within and dividing by the volume of the crystal. Position and size of the atom cloud and crystal are extracted from experimental images.

The first version of the numerical integration was implemented in Matlab to be used as a .m script used in Matlab's command line, where all the parameters needed to be determined beforehand and input by hand. Later, a Labview program was developed that incorporated automatic atom cloud analysis combined with manual size and position determination of the ion crystal, which made the process simpler and less prone to mistakes when copying results over from one program to the next. This program is described in the appendix in section B.4.3.

Here, the idea behind the numerical integration method will be briefly introduced. It was already described previously [120], where it was derived for ellipsoid crystals. When using molecular ions forming a string inside an ion crystal, an ellipsoid does not properly represent the shape the ion string. To better describe the ion string, a cylinder was used for the calculation of the estimated atom density sampled by the ions.

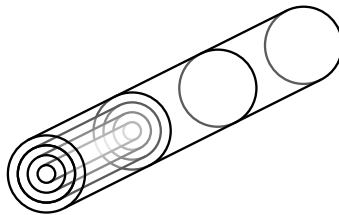


Figure 2.10: The principle of the calculation of the average rubidium atom density sampled by the cylinder encompassing the molecular ions inside a Coulomb crystal is shown. A cylinder is divided into segments longitudinally and each segment is divided into hollow cylinders (the hollow cylinders are shown for only one segment).

The basic idea behind the numerical integration is to divide a cylinder encompassing the ions into hollow cylinders of approximately constant density of rubidium atoms. As shown in Figure 2.10, the cylinder is divided into disks along its axis and each disk is divided into hollow cylinders. For small enough hollow cylinders, the atom density inside them is approximately constant over their volume, due to the rotational symmetry of the cylinders and the atom cloud distribution (assuming the centre of the atom density distribution lies on the central longitudinal axis of the encompassing cylinder). A few hundreds of divisions into disks and a few tens of divisions into hollow cylinders is enough for an adequate estimation of the average density sampled by the molecular ions. The average atom density is calculated by summing over the atom number inside each hollow cylinder and divide by the total volume of the cylinder.

## 2.6 O<sub>2</sub><sup>+</sup> state detection

As explained in section 2.2.5, molecular oxygen ions can be produced in selected vibrational states using resonance-enhanced multiphoton ionisation using suitable intermediate states in the neutral molecule. This technique has already been used in our group for the production of state-selected molecular nitrogen ions [97]. After the production of the ions, their internal state needs to be confirmed and the lifetime of that state needs to be measured.

### 2.6.1 Determination of Vibrational State

In the previous work in our group, a monitor gas was used to distinguish vibrationally excited ( $\nu \geq 1$ ) and non-excited ( $\nu = 0$ ) molecular nitrogen ions in laser-induced charge transfer used to probe the rotational distribution [97, 121, 122]. The reaction  $\text{N}_2^+ + \text{Ar} \rightarrow \text{N}_2 + \text{Ar}^+$  is only exothermic for vibrationally excited molecular nitrogen ions. The ionisation energy of molecular nitrogen is slightly below the one of argon, whereas it is higher for vibrationally excited molecular nitrogen ions, meaning in the ground state, the charge-transfer reaction does not happen. As this technique was already used and proven, adapting the technique for molecular oxygen ions was explored.

In molecular nitrogen ions, this technique was only used to distinguish the vibrational ground state from molecular ions in any excited vibrational state. Vibrationally excited molecular nitrogen ions react with neutral argon and are replaced with argon ions. The string of light molecular ions at the center of the crystal gets smaller, as the argon ions have approximately the same mass as calcium ions and diffuse into the crystal. Light ions that do not disappear are thus nitrogen ions in the vibrational ground state. This technique can be very sensitive, as losing just one or two light ions can already drastically change the appearance of the Coulomb crystals.

This technique can be extended to distinguish higher vibrationally excited states, by finding suitable reaction partners with ionisation energies in between the ones for molecular ions in its different vibrationally excited states. Table 2.2 shows suitable reaction partners that can be used to determine the the lowest three vibrational state of the O<sub>2</sub><sup>+</sup> ions. As an example, SO<sub>2</sub> will react with molecular oxygen ions with a vibrational state of  $\nu \geq 2$ , but not with  $\nu = 1$  or 0.

This scheme for the characterisation of the vibrational state of O<sub>2</sub><sup>+</sup> ions has been used by Böhringer and co-workers [123]. In their experiment, they used these three monitor gases to characterise their ion source used in ion drift tube experiments.

Table 2.2: The ionisation potentials of molecular oxygen ions in different vibrational states  $\nu$ . The last column shows reaction partners that have ionisation potentials between the vibrational state on the left and the next higher vibrational state.

IP O <sub>2</sub> <sup>+</sup> (eV)	$\nu$	does not react with
12.07	0	Xe (IP = 12.13 eV)
12.31	1	SO <sub>2</sub> (IP = 12.35 eV)
12.53	2	H <sub>2</sub> O (IP = 12.62 eV)



# Chapter 3

## The Shuttling MOT

This chapter provides an overview of the first part of this project, which was aimed at the development of a new kind of hybrid trap with better control over collision energies in reaction studies. The original idea and conceptualisation were introduced by Ravi Krishnamurthy, who also was responsible for the first implementation.

An inherent problem of hybrid traps is the difficulty in tuning the collision energies. Particles are cooled and stored in both traps, implying kinetic energies are generally low and constant. The problem of adjustable collision energy could be solved with the ability to add kinetic energy into the system in a controlled way. Optimally, this kinetic energy can be tuned over a large range with high accuracy and precision. Variable collision energies can be achieved by moving the two clouds relative to each other, where ideally only one of the two is moving.

Ions are easily moved by electric fields, making them seem like an optimal candidate for controlled movement. But since in hybrid experiments the ions are usually stored inside dynamic radio-frequency traps, moving them off-center from the trap axis introduces excess micromotion. This excess micromotion leads to an increased spread in their kinetic energy. Ions can be moved without the introduction of excess kinetic energy, if they are moved along the ion trap axis. This has been recently demonstrated in the group of Jonathan Home using time-varying electric potentials in a multizone segmented ion trap to move ions at velocities of  $7 \text{ m}\cdot\text{s}^{-1}$  and up to  $\pm 1000 \text{ }\mu\text{m}$  away from the trap center [124], but only with one or two independent ions at a time. So while ions can be moved easily, they are also easily disturbed and thus require very precise control over the electric fields used for trapping and manipulation.

On the other hand, cold atoms at rest are not moved as easily as ions, but several ways how atoms can be displaced exist. Possibilities include moving the center of a magnetic trap, moving an optical dipole trap or pushing atoms using scattering light. Section 1.1 in the introduction gives an overview of various concepts and implementations of experiments where these forces have been used to move atoms. For our experiment, using scattering light to push was chosen because it could be integrated into the current experiment with only modifications to the generation and distribution of the atom trapping light and no changes to the in-vacuum setup.

This chapter is separated into two major sections. The first section 3.1 deals with the technical implementation and methods of the shuttling atom trap and discusses the relevant experimental techniques. The second section 3.2 provides an overview of the performance of the shuttling magneto-optical trap and presents the first reaction

study between shuttling rubidium atoms and calcium ions in the hybrid trap. A final section summarises and concludes this chapter.

## 3.1 Technical Implementation and Methods

This section describes the technical implementation of the shuttling atom trap. It starts with a description of the experimental setup inside and around the vacuum chamber and the working principle behind the shuttling atom trap. The generation of the cooling, trapping and pushing light is explained, starting with the description of generating the laser light using an external-cavity diode laser, amplified by a tapered amplifier. Further, the manipulation of the light using a setup of acousto-optic modulators driven by a home-built radio frequency setup to create the necessary cooling and pushing light pulses is explained and the pulse sequence used and its generation are discussed. Also covered are the imaging systems used to analyse the dynamic atom cloud. To interpret the obtained data, simulations developed by Claudio von Planta and finalised by Alexander Dörfler are briefly introduced at the end of this section.

### 3.1.1 Experimental Setup

The original setup this work is based on was designed, built and characterised by Felix Hall and is described in detail in his PhD thesis [1]. The hybrid trap used in this experiment consists of a linear Paul trap in conjunction with a magneto-optical trap. An overview of the experimental setup is shown in Figure 3.1.

In the original MOT setup, a single laser beam at 780 nm was split up three times into retro-reflected cooling beams for the six beams needed for the magneto-optical trap. For the shuttling atom trap, this configuration was kept on two axes (designated  $y$  and  $z$ ), but for the third axis along  $x$ , the cooling beams were split into two individual beams. The magnetic coils in the vacuum have been left in their original configuration, but newly designed rubidium sources (described in appendix A.1) have been installed.

On the ion setup, two spatially overlapped, retro-reflected beams at 397 nm and 866 nm are aligned along the axis of the ion trap. Over the course of this thesis the old ion trap had to be replaced due to cracks in the ceramic holders. However, the reaction data presented in section 3.2.3 have been measured using the old trap. The new trap has the same relevant dimensions as the old trap, but with an updated design following the design of the ion trap used in Daniel Rösch's PhD thesis [125]. The calcium sources have also been replaced with updated designs and are described in appendix A.1 together with the new ion trap design in appendix A.2. A fibre on a translational stage can be moved into the ion trap center as a reference point for the alignment of lasers into the trap center.

### 3.1.2 Operation Principle

This section explains how the concepts of moving atoms with light introduced in section 2.3.2 can be used to generate a dynamic atom trap with control over the atom velocities. In a nutshell, atoms are shuttled between two off-center positions inside the MOT using scattering light forces to move the atoms.

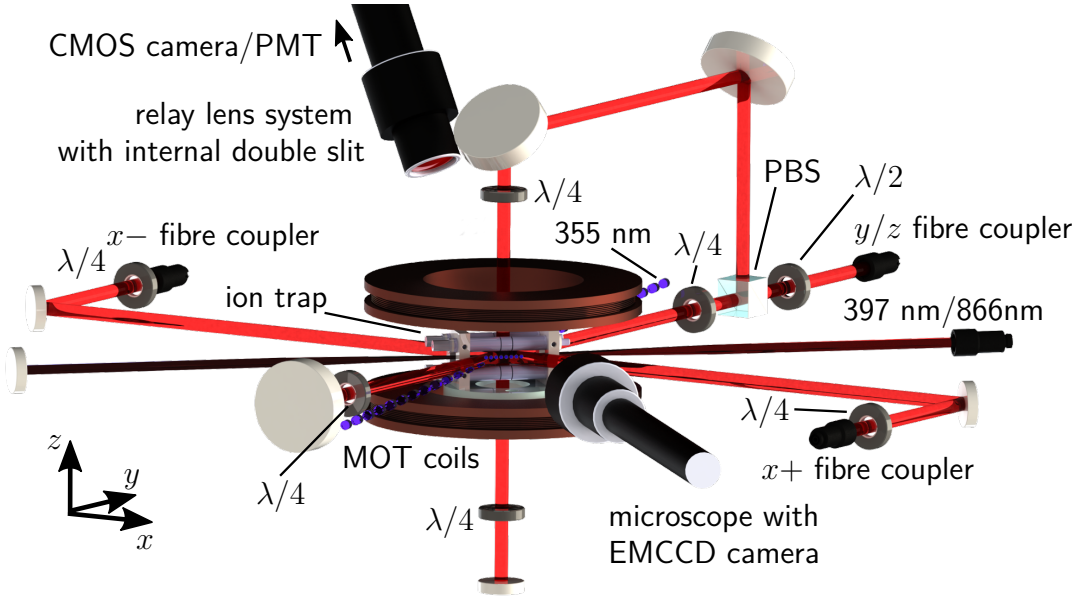


Figure 3.1: The experimental setup. The ion trap is located at the center, encompassed by two coils which provide the quadrupolar field for the magneto-optical trap. The frequency-tripled output of a Nd:YAG laser at 355 nm is used to generate calcium ions by non-resonantly ionising calcium atoms from an effusive oven (not shown). Two spatially overlapped laser beams at 397 nm and 866 nm aligned along the ion trap axis provide Doppler laser cooling light for the calcium ions. Cooling and trapping light for the atoms along the axes  $y$  and  $z$  is provided by a single beam split into two retro-reflected counter-propagating beams. Two individual counter-propagating beams are overlapped along the  $x$  axis in order to have control over the intensity and frequency of the two beams individually, which is necessary for the shuttling trap operation as described in section 3.1.2. The microscope connected to an EMCCD camera in the  $yz$  plane is shown, as well as the top-down relay lens system connected to a CMOS camera are shown and are described in detail in section 3.1.7.

Off-center atom clouds are produced by reducing the intensity of one of the  $x$ -axis laser beams. To push the atoms, the cooling laser beams along the  $x$ -axis are turned off, while simultaneously turning on a pushing laser originating from the side the atom cloud was off-set to. This push beam is on for approximately 200  $\mu$ s, which accelerates the atoms to speeds of a few metres per second depending on the push beam intensity used. The push beam duration is kept short in order to ensure that the atoms are in free flight when they pass the trap center. During this time, the cooling along the  $y$ - and  $z$ -axis is kept on to continuously cool and provide confinement along these axes.

Once the atoms have passed the trap center, the cooling laser beams along the  $x$ -axis are turned on again, with reversed intensities, trapping the atom cloud in an off-center position opposite the original one. From there, the atoms are pushed back to their original position, completing one shuttling cycle. Continuously driving the cycle results in a shuttling atom cloud that can be used for reaction experiments. A schematic of this process is shown in Figure 3.2.

During reaction experiments, the calcium ions in the ion trap also need to be laser cooled. Since the 397 nm laser used to cool the ions can ionise rubidium in

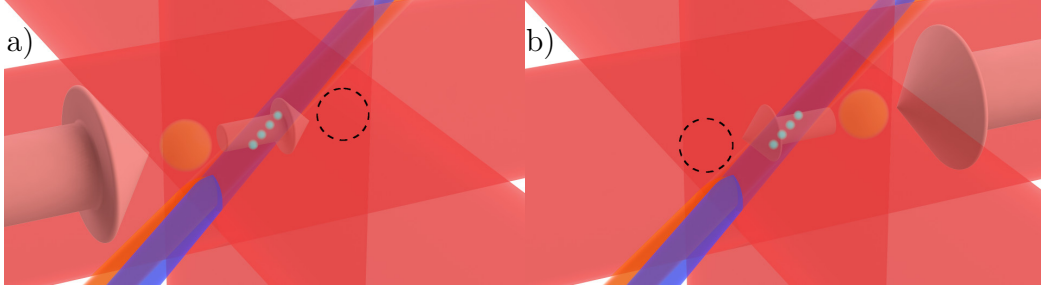


Figure 3.2: Schematic of the operation principle behind the shuttling hybrid trap. a) An off-center atom cloud in orange gets pushed and moves through ions laser-cooled in the ion trap in blue towards an off-center position on the other side. b) From there, the atom cloud is pushed back through the ions to the original off-center position, completing one cycle.

the excited state (as explained in section 2.2.4), the 397 nm und 780 nm laser must not be on at the same time. During the equilibration time of the atom cloud in the off-center position, the ions and atoms are both laser cooled by alternating between laser cooling of the two species in intervals of 200  $\mu$ s. During the pushing of the atoms and the subsequent free flight of the atom cloud, the ions are not laser cooled. For more details on the exact pulse sequences used see section 3.1.6 and Figure 3.6.

### 3.1.3 Light Generation

**780 nm** To generate the light used in the shuttling magneto-optical trap, a single commercial external-cavity diode laser (ECDL, model DL100 from Toptica Photonics) is operated at approximately 780 nm. Using saturated absorption spectroscopy [126, 127] on a glass cell filled with rubidium vapour, the laser is locked to the crossover line between the  $F = 2 \rightarrow F' = 3$  and  $F = 2 \rightarrow F' = 1$  transitions in the D2 line of rubidium-87 [111]. This locks the laser 212 MHz away from being resonant with the  $5s \ ^2S_{1/2} (F = 2) \rightarrow 5p \ ^2P_{3/2} (F' = 3)$  transition.

The laser light is amplified using a tapered amplifier (BoosTA by Toptica Photonics). Out of the approximately 30 mW coupled into the amplifier, over 1 W of laser power is produced, which is directly coupled into a fibre. The fibre provides mode-cleaning and transports the light to the optical assembly controlling the shuttling operation. The light generation setup for the atom trap is shown in Figure 3.3.

**397 nm & 866 nm** The light used to cool the calcium ions is produced by another two ECDL operating at 397 nm and 866 nm (DL100 pro and DL100, respectively, from Toptica Photonics). The 866 nm laser is shared with other experiments in the lab using beam splitters and its light is transported to the experiment using a fibre. The 397 nm laser is used exclusively for this experiment. Both lasers used for ion cooling are locked to a high-precision wavemeter (HighFinesse WS/U-30) using a home-built locking software called LaserLock written in LabVIEW and described in appendix B.1.

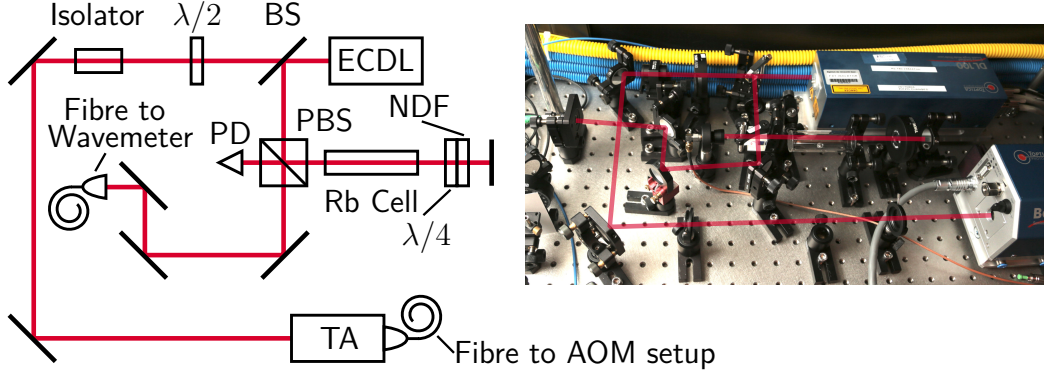


Figure 3.3: A schematic of the 780 nm laser setup on the left and a photograph of the experiment with an overlaid laser beam path in red on the right. The external cavity diode laser (ECDL) generates laser light at around 780.246 nm. A beam sampler (BS) reflects a small amount of laser light onto a polarising beam splitter (PBS) cube, which reflects a fraction of the beam to pass a glass cell filled with rubidium. The beam is attenuated and reflected back onto the ingoing beam and acts as the spectroscopy beam in the saturated absorption spectroscopy. The quarter-wave ( $\lambda/4$ ) plate is rotated such that it turns the polarisation of the spectroscopy beam by  $90^\circ$  with respect to the incoming beam. This makes the spectroscopy beam pass through the PBS and hit the photo diode (PD). The photo diode is connected to the laser controller, which uses a lock-in regulator to lock the laser. The initially transmitted part of the PBS is aligned into a fibre going to a wavemeter for simple verification of the lock and calibration of the wavemeter. The beam transmitted through the initial beam sampler directly after the laser is aligned through an isolator and into a tapered amplifier (TA). The TA's output is aligned into a fibre for mode cleaning and transportation of the laser light to the AOM setup.

### 3.1.4 Light Manipulation

To generate the light pulses at different frequencies and intensities as explained in section 3.1.2, the output of the fibre transporting the light from the tapered amplifier is split multiple times and sent through a setup of acousto-optic modulators (AOM). A schematic of this setup is shown in Figure 3.4.

The laser beam coming out of the fibre is split into two beams, where the first arm is used for cooling along the  $y$ - and  $z$ -axis. The beam is sent through an AOM to shift the light slightly to the red of the  $5s \ ^2S_{1/2} (F = 2) \rightarrow 5p \ ^2P_{3/2} (F' = 3)$  transition. The first-order diffracted output of the AOM is sent through an electro-optic modulator (EOM), which generates sidebands to repump population on the  $5s \ ^2S_{1/2} (F = 1) \rightarrow 5p \ ^2P_{3/2} (F' = 2)$  transition. The output of the EOM is then coupled into a fibre to transport the light to the experiment table, where it is split into two retro-reflected beams for  $y$  and  $z$ .

The second arm of the splitter after the fibre is used to generate the light for cooling and pushing along the  $x$ -axis. This beam is split into individual beams for both directions along the  $x$ -axis, where each of these two beams is split again into beams for cooling ( $xc+/xc-$ ) and pushing ( $xp+/xp-$ ). The AOM of the cooling beams are operated at the same frequency as the  $yz$  AOM mentioned above, whereas the AOM for the pushing beam is operated such that the light is shifted on resonance



### 3.1.5 Radio Frequency Generation and Manipulation

The radio frequencies (RF) powering the five AOMs (one for  $yz$ , and two each for pushing and cooling along both directions of the  $x$ -axis) are generated using a home-built setup made from Mini-Circuits components. For an explanation of the different RF components, see appendix C for more details and part numbers. The beams along the  $x$ -axis and the ones along the  $y$ - and  $z$ -axis have different requirements for their switching abilities, where the latter ones just need to be switched on and off. The cooling beams along the  $x$ -axis also have to be switched on and off, where the on state can either be high power or low power. The pushing beams along the  $x$ -axis need to be switched on and off too, where the power level of the on state needs to be continuously adjustable. An overview of the setup can be found in Figure 3.5.

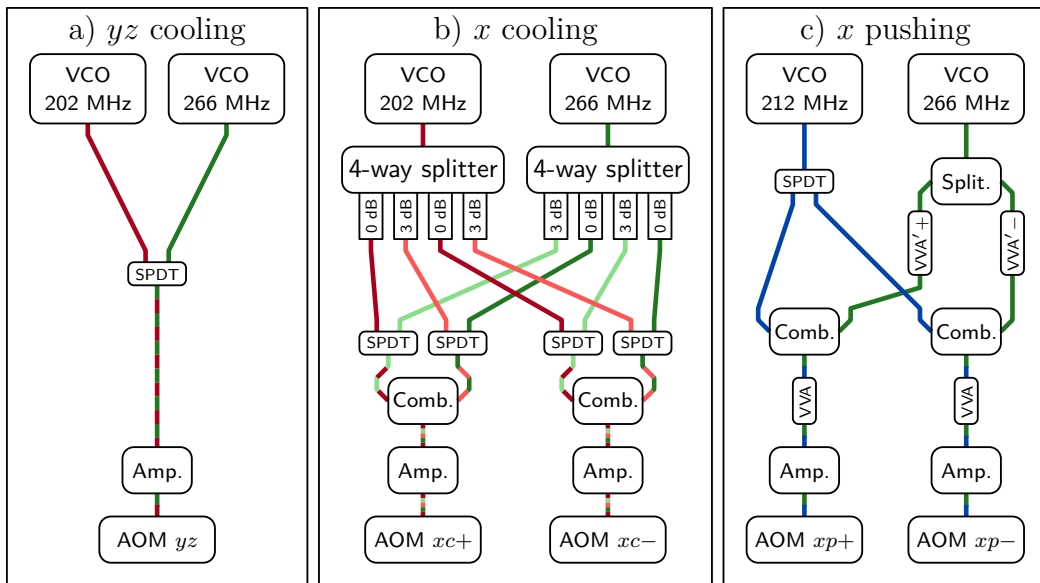


Figure 3.5: A schematic of the radio frequency setup powering the AOMs. See text for more details. a) Creating the cooling and compensation frequencies for  $yz$  only requires two voltage-controlled oscillators (VCO) and one single pole double throw (SPDT) switch to switch between the two radio frequencies. b) For cooling along  $x$ , the initial radio frequency at the cooling and compensation frequency are both split up into four, two of each are attenuated. Using two SPDT switches for pulse control and a single splitter as combiner (Comb.) per side, the radio frequencies are mixed before going into the amplifier (Amp.). c) For pushing along  $x$ , the pushing radio frequency is split and controlled using a single SPDT while the compensation radio frequency is controlled using a splitter and two voltage-variable attenuators (VVA) used as on/off switches. A splitter in reverse is again used as a combiner for each side, whose outputs are going into another set of voltage-variable attenuators (VVA) two continuously tune the push beam power.

The RF is generated using voltage-controlled oscillators (VCO). There are separate VCOs for the cooling along  $yz$ , the cooling along  $x$  and the pushing along  $x$ . The VCOs for the cooling AOMs were typically operated around 200 to 204 MHz, resulting in a cooling detuning from 12 to 8 MHz, while the VCO for the pushing AOMs was usually

kept at 212 MHz, shifting the diffracted beam on resonance with the  $5s \ ^2S_{1/2} (F = 2) \rightarrow 5p \ ^2P_{3/2} (F' = 3)$  transition.

Initial experiments revealed that the AOMs heat up due to the dissipation of the RF power, which leads to a change in the deflection angle of the deflected beam. In order to have stable operation conditions during switching operation, the amount of RF power dissipated in the AOMs should be constant over time [128]. For this reason, instead of switching the RF off to switch off the laser beam, the RF is switched to a different frequency sufficiently far away (266 MHz) from the typical operation frequencies. At this higher frequency, no light is deflected, but the RF power is still dissipated in the AOM. This ensures a steady operation of the AOMs. The RF at 266 MHz is generated by a second set of VCOs, one for every VCO generating the RF for cooling and pushing. From here on, this part of the RF setup will be referred to as compensation.

**Radio frequency setup for cooling along the  $y$ - and  $z$ -axis** Since the cooling along the  $y$ - and  $z$ -axis only needs to be switched on an off, the corresponding RF setup is comparably simple and is shown in Figure 3.5 a). The cooling RF and compensation RF are connected to the pole port of a single pole double throw (SPDT) switch<sup>1</sup>, which applies either frequency depending on the cooling laser beam along the  $y$ - and  $z$ -axis being on or off. The output of the SPDT is connected to the input of an amplifier, whose output is directly connected to the  $yz$  AOM.

**Radio frequency setup for cooling along the  $x$ -axis** Two separate AOMs are used for the two independent beams along the  $x+$ -axis and  $x-$ -axis, generating light at the cooling detuning with high intensity, low intensity or being turned off. The schematic for their RF generation is shown in Figure 3.5 b). The output from a single VCO is split into four equal parts using a four-way splitter. For the low-power operation of the AOMs, two fixed attenuators are connected to two of the outputs of the four-way splitter. This setup resulting in two RF outputs at high power and two at low power is copied with a VCO operating at the compensation frequency.

To generate the RF to be fed into the AOM for the cooling laser beams along the  $x$ -axis, one high-power output at the cooling frequency and one low-power output at the compensation frequency are connected to the throw inputs of an SPDT, and one low power output at the cooling frequency and one high power output at the compensation frequency are connected to the throw ports of a second SPDT. The switching logic of these two SPDT is shown in Table 3.1.

The outputs of the two SPDT are combined on a two-way splitter used in reverse whose output is connected to an amplifier which then connects to the AOM. This setup of combining 4 different radio frequencies using two SPDTs and one two-way splitter exists for both  $xc+$  and  $xc-$ .

**Radio frequency setup for pushing along the  $x$ -axis** The setup to generate the radio frequency for the AOMs creating the pushing pulses is shown in Figure 3.5 c). Since the two pushing beams are never on at the same time, a single SPDT is used to split and control which of the two amplifier receives the pushing radio frequency.

---

<sup>1</sup>An SPDT switch consists of one input (pole) and two outputs (throw) and two control inputs to switch which throw is connected with the pole. They can also be used in reverse. See Appendix C.4.

Table 3.1: Switching logic for  $xc+/xc-$  cooling and compensation RF. The throw ports of SPDT 1 has high cooling and low compensation RF connected, whereas SPDT 2 has low cooling and high compensation RF connected.

$xc+/xc-$ setting	SPDT 1	SPDT 2
high power	high cooling RF	no output
low power	low compensation RF	low cooling RF
off	no output	high compensation RF

The compensation frequency is split using a two-way splitter connected to two VVA (marked as VVA' in the figure), acting as on/off switches<sup>2</sup>. The switching logic for all the SPDT and two VVA' is summarised in Table 3.2.

One each of the outputs of the SPDT and the two-way splitter is combined on two-way splitters used in reverse. After combining the radio frequencies for compensation and pushing, two individual VVA control the total amount of radio frequency fed into the amplifier and thus intensity of the resulting pushing beam.

Table 3.2: Switching logic for  $xp+/xp-$  pushing and compensation RF. The throw ports of the SPDT route the pushing RF to one of the two amplifiers. The VVA' block the compensation RF when their control is set to low (i.e. 0 V) and let it through when set to high.

active AOM	SPDT	VVA'+	VVA'-
$xp+$	throw+	low	high
$xp-$	throw-	high	low
neither	no output	high	high

### 3.1.6 Pulse Sequence Programming

The setup generating the radio frequency for the AOMs introduced in the previous section contains multiple switches, which all have control inputs to change the states of the switches. For every SPDT switch, there are two control ports and the two VVA' in the  $x$  pushing setup each have one control port. With all six SPDT switches and two VVA to control, a total of 14 control inputs need to be triggered.

Originally, a Digital Delay Pulse Generator model 9528 by Quantum Composers was used to generate the necessary trigger pulses for the shuttling operation. As this pulse generator only has 8 outputs, additional home-built logic electronics were needed to trigger all 14 control ports. As this setup was reaching its limits with generating the pulse sequences for reaction experiments due to the limitations of the

<sup>2</sup>An “off” state of 0 V connected to the control port of the VVA results in an attenuation of > 40 dB, effectively blocking the RF. At the control voltages output by the pulse generator used, the attenuation is around 5 – 10 dB, effectively passing the RF through.

Quantum Composers pulse generator<sup>3</sup>, a new source for the generation of the control pulses was sought.

A new solution was found with the PulseBlaster programmable TTL pulse generator from SpinCore Technologies, which are available as PCI cards. They offer up to 24 channels which are individually controllable and arbitrary timing sequences can be programmed, making it much more versatile than the initially used Quantum Composers pulse generator. The PulseBlaster has a worse pulse resolution (10 ns versus 250 ps on the Quantum Composers pulse generator), but for the shuttling atom trap this is sufficient, as the usual duration of pulse instructions are on the order of a few to hundreds of microseconds.

A total of 14 out of the 24 channels of the PulseBlaster were used to control the RF setup, removing the need for external logic electronics and simplifying the setup. One additional channel is used to trigger the oscilloscope during TOF measurements and an optional channel can be used to trigger the EMCCD camera if needed.

The relevant part of a typical pulse sequence is shown in Figure 3.6. The three phases of equilibration of both atoms and ions, pushing of the atoms and free flight of the atom cloud are shown schematically and explained in the caption.

### 3.1.7 Imaging

Two different imaging systems were used to monitor the laser-cooling fluorescence of the ions and atoms. To see the position of both imaging systems in the experiment, see Figure 3.1. The first imaging system consisted of an electron-multiplying charge-coupled device (EMCCD) camera attached to a microscope with approximately 10 $\times$  magnification. This assembly lies in between the axes of the  $xy$  plane of the experiment and thus corresponds to a side-on view at a 45 $^\circ$  angle to the shuttling axis. Using exchangeable narrow bandpass filters inside the microscope, the fluorescence of either the ions or the atoms can be imaged. This imaging system is used to take images of the stationary atom cloud for analysis. During reactions, it is used to monitor fluorescence of the calcium ions (sample images are shown in Figure 2.9).

The second imaging system is installed from the top looking down, slightly angled from the  $z$  axis and perpendicular to the  $x$  axis. It consists of a 1:1 relay lens system, which by using a beam splitter simultaneously images the fluorescence of the atoms onto a complementary metal-oxide semiconductor (CMOS) camera and a photomultiplier tube (PMT). A schematic of this imaging system is shown in Figure 3.7 a). This imaging system is used exclusively to image the atoms and a sample image taken with the CMOS camera is shown in Figure 3.7 b). A double slit can be inserted into the relay lens system, which restricts the light scattered by the atom cloud. The light scattered as the atom cloud passes by the two slit positions results in a double peak in the PMT signal. From the time delay of the two peaks and the distance between the two slits combined with the magnification factor of the relay lens system, the velocity of the atom cloud between the two slits can be calculated.

The atom cloud can even be imaged using digital consumer cameras which had their IR filter removed. Such a sample image is shown in Figure 3.7 c) to give an impression of the scale of the experiment.

---

<sup>3</sup>With the model 9528 pulse generator all channels are synchronised to the programmable internal time period  $T_0$ , meaning that totally arbitrary pulse sequences are not possible, but such sequences are desirable for the exploration of more complex pulse sequences for future work.

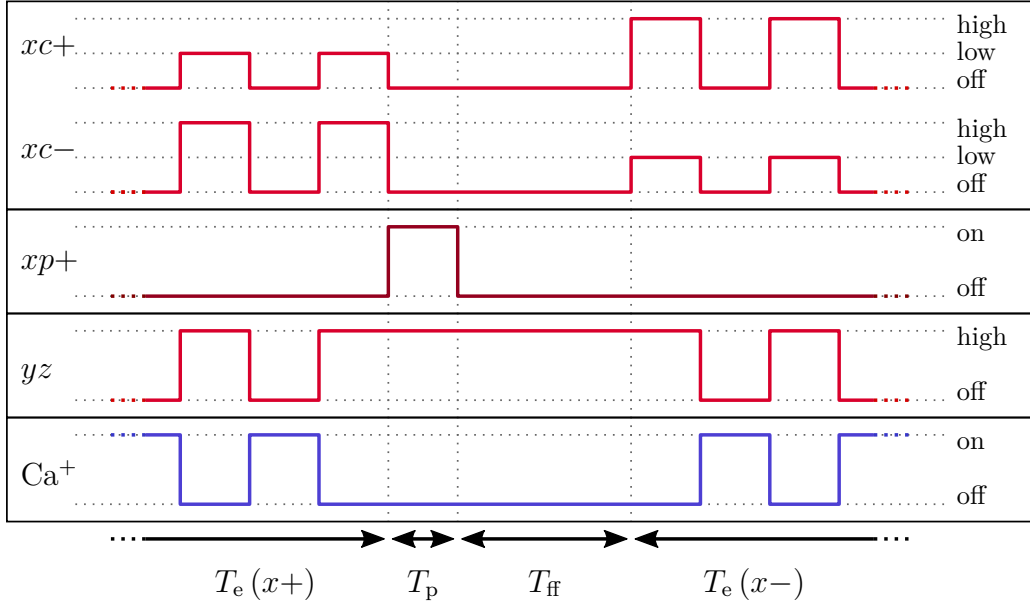


Figure 3.6: Pulse sequence for one pushing sequence used in the shuttling hybrid trap during reaction experiments. After equilibration of the atoms and ions during the equilibration time period  $T_e(x+)$ , where both species are cooled alternately, the atoms are pushed along the  $x$  axis towards the ions during pushing time period  $T_p$ . In the following free flight time period  $T_{ff}$ , the atoms move at constant velocity through the trap center, where they interact with the ions. Once the atoms have reached the other off-center equilibrium position, another equilibration time period  $T_e(x-)$  starts with reversed intensities along  $x$ . After  $T_e(x-)$  the atoms are pushed back again using the push beam from the opposite side and restarting the shuttling cycle. During reaction experiments, the equilibration time period was set to 39.2 ms, where the MOT cooling lasers along the  $x$  axis were on for 200  $\mu$ s, alternating with the  $Ca^+$  laser which was on for 160  $\mu$ s with 20  $\mu$ s of no laser light in between. Typical duration of the push beam period was 200  $\mu$ s, followed by free-flight period of 600  $\mu$ s.

### 3.1.8 Simulations

This section will briefly cover simulations of the shuttling process, which were originally developed by Claudio von Planta during his master thesis [129] and further developed by Alexander Dörfler.

The dynamics of the shuttling atom cloud were simulated using Monte Carlo trajectory simulations in two separate programs. The first program simulates a model atom cloud while taking into account all the relevant experimental parameters, such as laser beam profile, light frequency and magnetic field gradient. Values used for these parameters were measured values as used in the experiments. Typically around 20'000 Rb atoms were simulated using a velocity Verlet algorithm to integrate the equation of motions to obtain the classical trajectory of each atom. Atom-atom interaction were neglected because of the low densities of the atom cloud, which were on the order of  $10^8$  to  $10^9$   $cm^{-3}$ . In order to match experimentally observed geometric and thermal properties of the atom cloud, an adjustable stochastic heating force was implemented.

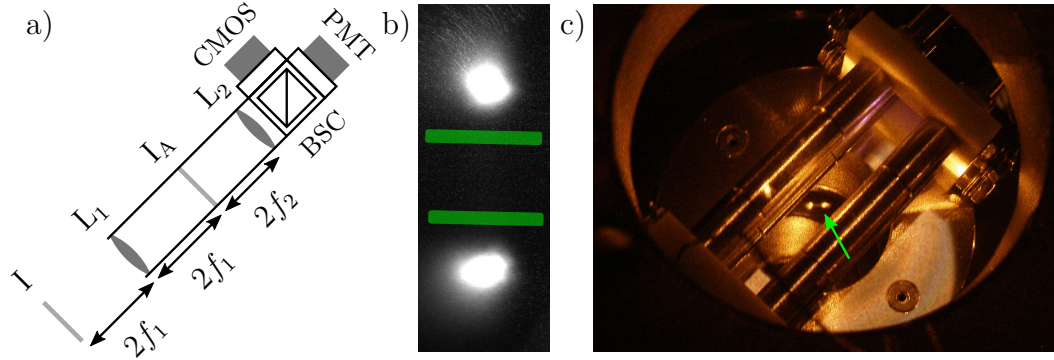


Figure 3.7: Top down shuttling imaging system and images of the shuttling atom cloud. a) Schematic of the one-to-one relay lens system used to image the shuttling atom cloud and record time of flight traces. Placing a lens  $L_1$  with focal length  $f_1 = 100$  mm at a distance corresponding to twice its focal length  $2f_1$  away from the image plane I will image the image plane I to a position behind the lens at a distance of another  $2f_1$ , creating an image plane  $I_A$ . A second lens  $L_2$  with focal length  $f_2 = 60$  mm at a distance  $2f_2$  from  $I_A$  relays the image onto two imaging sensors simultaneously using a beam splitter cube (BSC). A CMOS camera is used to image the atom cloud and a PMT is used to measure time-of-flight traces in conjunction with an optional double slit aperture inserted into the image plane  $I_A$ . b) Experimental images as seen by the CMOS camera connected to the top-down imaging system. The green bars indicate the positions of the double slit used for time-of-flight measurements. c) Image taken with a commercial digital camera with removed IR filter showing the shuttling atom cloud as two connected bright spots between the central ion trap electrodes, highlighted by a green arrow.

The second program simulates the actual pushing of the atom cloud. It takes the equilibrated atom cloud from the first program as input and applies the radiation pressure force generated by the on-resonance push beam. A fourth-order Runge-Kutta algorithm was used to integrate the equations of motion in this program. To compare with measured time-of-flight curves, atoms passing through the volume sampled by the slit aperture in the experiment were counted against time to generate simulated time-of-flight curves. The mean and width of the velocity distribution of atoms passing the trap center can be extracted from the trajectories of the atoms, giving insight into the inner dynamics of the atom cloud during shuttling operations.

## 3.2 Measurements and Results

This section presents the results from the characterisation of the shuttling atom cloud. First experiments were performed to measure the velocity range in which the shuttling atom cloud can be operated. Over the course of the optimisation process, various settings were changed to find the optimal experimental parameters. The detuning of the cooling and the pushing beam was varied, as well as cooling laser intensities and magnetic field gradient. A single measurement series performed usually consisted of a scan over the available range of push beam energies.

The result from these scans are time-of-flight spectra, which only contain the information of the speed of the atom cloud, but no other directly inferable parameters of the atom cloud such as expansion of the cloud or internal velocity distribution. To be able to get insight into the internal parameters of the atom cloud, the measured TOF spectra were compared to simulated spectra, where the relevant measured experimental parameters were used as input for the simulations.

The section is concluded with a first test of the shuttling atom cloud being used for reaction studies, where the reaction between laser-cooled calcium ions and neutral rubidium atoms was revisited. This system was already studied on this setup in detail before in the work of Felix Hall [1, 65, 75] using stationary atom clouds. The interaction time of the two clouds during reactions is calculated, which is used together with density estimations from reactions of molecular nitrogen ions with the shuttling atom cloud [130, 131] to determine the second-order rate constant for the reaction of calcium ions in the ground state.

### 3.2.1 Time-of-Flight Measurements

To evaluate the operation range of the shuttling atom cloud, time of flight (TOF) traces were measured at various experimental settings. Final settings were a cooling detuning of 10 MHz and an on-resonance push beam. One such TOF trace is shown in Figure 3.8. The alignment was optimised for symmetry of the shuttling atom cloud and maximum brightness of the atoms, which is crucial for the measurement of the time of flight traces. Only a bright enough atom cloud will produce enough signal on the PMT to make the measurement of TOF traces possible. The PMT signal was digitally filtered<sup>4</sup> on the oscilloscope and averaged over a few individual traces ( $< 10$ ). This greatly reduces noise in the PMT signal originating from various light sources in the lab (minimised by working in a dark lab) and stray light from 780 nm laser light reflections.

A program was written to automatically measure TOF traces over a range of push beam powers and generate TOF spectra. All relevant measurement parameters such as laser intensities and detunings are recorded and used as input for Monte Carlo trajectory simulations as explained in section 3.1.8. The resulting simulated TOF trace is shown in Figure 3.8 and shows good agreement with the experimental TOF trace. Insets in the figure show snapshots of the simulated atom cloud at various moments during the simulated free flight process.

The outcome of one such measurement generating a TOF spectrum is summarised in Figure 3.9, where experimentally determined kinetic energies of the atoms are compared with the corresponding results from simulations. The required powers in the experiment are matched with push beam powers used in the simulations to achieve the same kinetic energy of the rubidium atoms. The small discrepancies were attributed to experimental imperfections, such as non-optimal alignment of the laser beams and small performance variations in optical components along the  $x+$  and  $x-$  beam paths.

---

<sup>4</sup>The LeCroy WaveSurfer 64MXs-A oscilloscopes offer an ERES (Enhanced RESolution) filter, which applies a Finite Impulse Response (FIR) filter. A FIR filter works similar to a moving average and smooths out high-frequency noise [132].

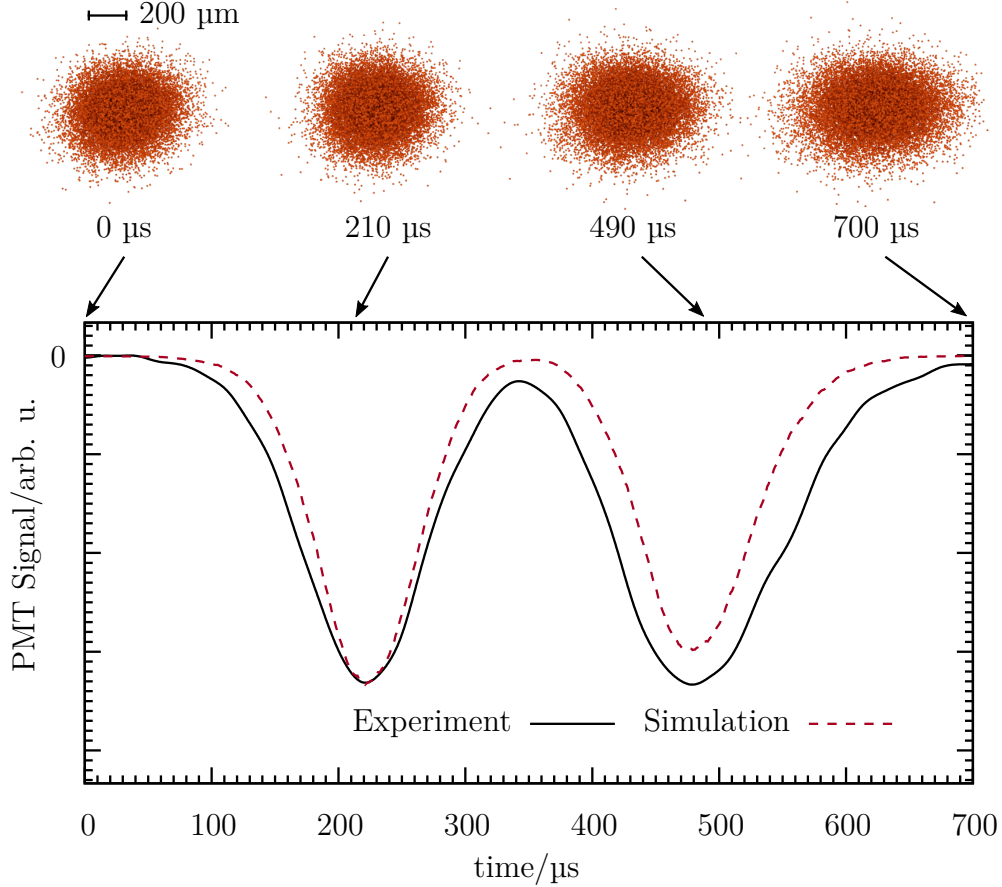


Figure 3.8: Comparison of a representative measured time-of-flight trace (solid black line) with the results from Monte Carlo trajectory simulations (dashed red line). Traces are inverted since the Signal of the PMT used has negative polarity. Images at the top show snapshots of the atom cloud at various time steps during the simulation and show the expansion of the cloud during the shuttling process. Simulation credit: Alexander Dörfler.

### 3.2.2 Results from Simulations

The measured TOF spectra only give insight into the average kinetic energies of the rubidium atoms. As demonstrated in the previous section, the simulations are able to reproduce the shape of the TOF curves (Figure 3.8) and the push beam power dependence (Figure 3.9) well, thus additional information can be extracted from the obtained trajectories. One important parameter to know is the spread in kinetic energy. The kinetic energy distributions of the simulated atom clouds passing the trap center are fit with a Gaussian distribution to obtain the standard deviation  $\sigma$  as the kinetic energy spread. The results from one such simulation series can be found in Figure 3.10, where they are summarised as spread in Rb kinetic energy and spread in collision energies of the  $\text{Ca}^+ - \text{Rb}$  system.

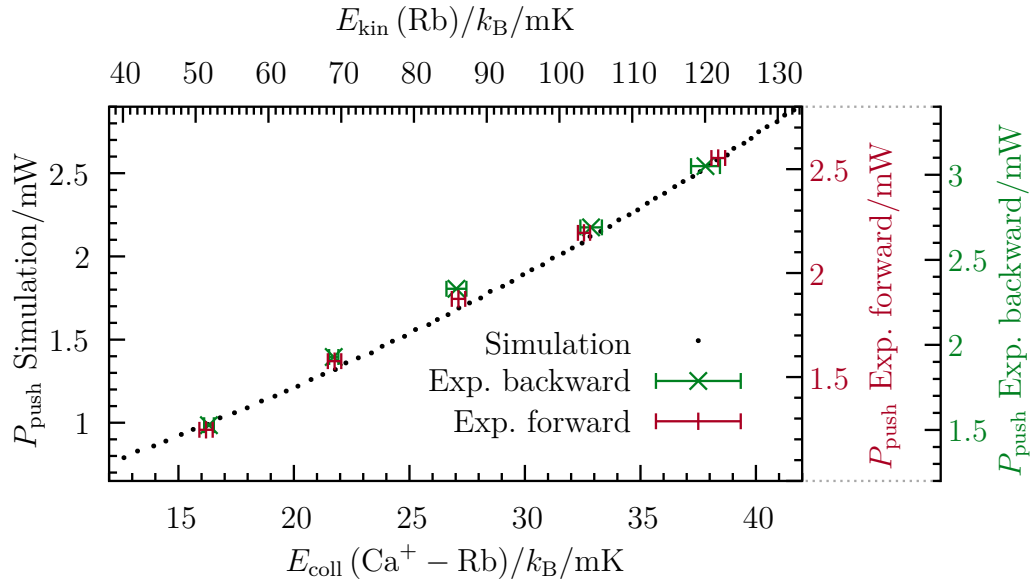


Figure 3.9: Required push beam powers versus the obtained collision energy for the  $\text{Ca}^+ - \text{Rb}$  system (assuming stationary calcium ions) on the bottom abscissa and corresponding kinetic energies of the rubidium atoms on the top abscissa. The push beam power on the left represents required powers in simulations to replicate the experimentally measured time of flights and thus collision energies. Experimental push beam powers are shown on the right for both flight directions. Horizontal error bars indicate one standard deviation over a series of ten measurements and indicate a good reproducibility of velocities of the shuttling atom cloud. Simulation credit: Alexander Dörfler.

### 3.2.3 Reactions with Ion Crystals

As a first test system for reaction studies, the reaction of neutral rubidium atoms with singly charged calcium ions was revisited. Coulomb crystals were loaded into the ion trap and moved axially out of the way of the shuttling atom cloud. The shuttling atom cloud was then turned on and after enough time for the atom cloud to reach equilibrium, the crystal was moved to the center and images of the crystal were taken in regular intervals. A LabVIEW program exists to monitor the velocity of the atom cloud during reaction measurements by recording TOF traces in a given interval and fitting them to determine the atom cloud flight time. The program and fitting procedure are described in the appendix B.3.3.

As described in Section 2.5.1, reaction rates are determined by observing the decrease in fluorescence, as laser-cooled and thus fluorescing calcium ions are replaced by dark product ions. Images taken during the reaction experiments (see insets in Figure 3.11) were analysed using a custom LabVIEW program described in Appendix B.4.1. Crystal volumes were obtained by fitting ellipses and flattened ellipses to the crystal shapes, from which the volume occupied by the crystals could be calculated.

Figure 3.11 shows a measurement series at rubidium kinetic energies  $E_{\text{kin}}/k_B$  of 80 mK, corresponding to a collision energy  $E_{\text{coll}}/k_B$  of 25 mK in the  $\text{Ca}^+ - \text{Rb}$  system, assuming calcium ions at rest. Averaging over four experiments, the pseudo-first order

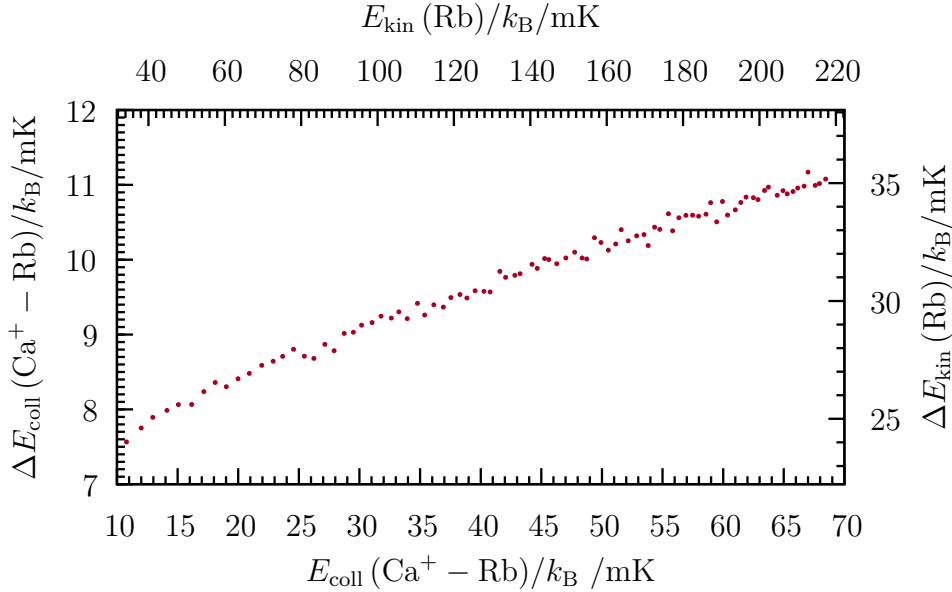


Figure 3.10: Data points shown are kinetic energy spreads obtained from fitting Gaussian distributions to kinetic energy distributions obtained from simulations of pushing atom clouds. Axes are representing either rubidium kinetic energy  $E_{\text{kin}}$  and kinetic energy spread  $\Delta E_{\text{kin}}$  or collision energy  $E_{\text{coll}}$  and collision energy spread  $\Delta E_{\text{coll}}$  in the  $\text{Ca}^+ - \text{Rb}$  system, assuming calcium ions at rest. Simulation credit: Alexander Dörfler.

rate constant was determined as  $k_{\text{pfo}} = 1.6(1) \times 10^{-4} \text{ s}^{-1}$ . The reaction rate constant obtained without a shuttling rubidium atom cloud present was found as  $5(2) \times 10^{-5} \text{ s}^{-1}$  and represents the reaction rate of calcium ions with background gas in the ultra-high vacuum chamber when no atom cloud is present (which was achieved by switching off the EOM).

### 3.2.4 Second Order Rate Constant Estimation

In order to calculate the second order rate constant from the pseudo-first order measurements presented in the previous section, the interaction time of the two clouds needs to be calculated and the density of the travelling atom cloud needs to be estimated.

**Interaction Time Estimation** Reactions only happen when the atom cloud and ion crystal are spatially overlapped, which in the shuttling atom cloud only happens during the free-flight time period as the atom cloud passes the ion trap center. This results in a much shorter interaction time compared to reactions with stationary atom clouds.<sup>5</sup>

<sup>5</sup>As a simple estimation for an interaction distance of approximately 300  $\mu\text{m}$  (the approximate size of the atom cloud) and a speed of 3.9  $\text{m}\cdot\text{s}^{-1}$  (corresponding to a kinetic energy  $E_{\text{kin}}/k_{\text{B}}$  of 80 mK as used in the reactions presented in the previous section), this results in a interaction time of only around 77  $\mu\text{s}$  per single shuttling event. At 25 shuttling events per second, this totals in an interaction time of only 1.9 ms per second of shuttling the atom cloud back and forth. In other

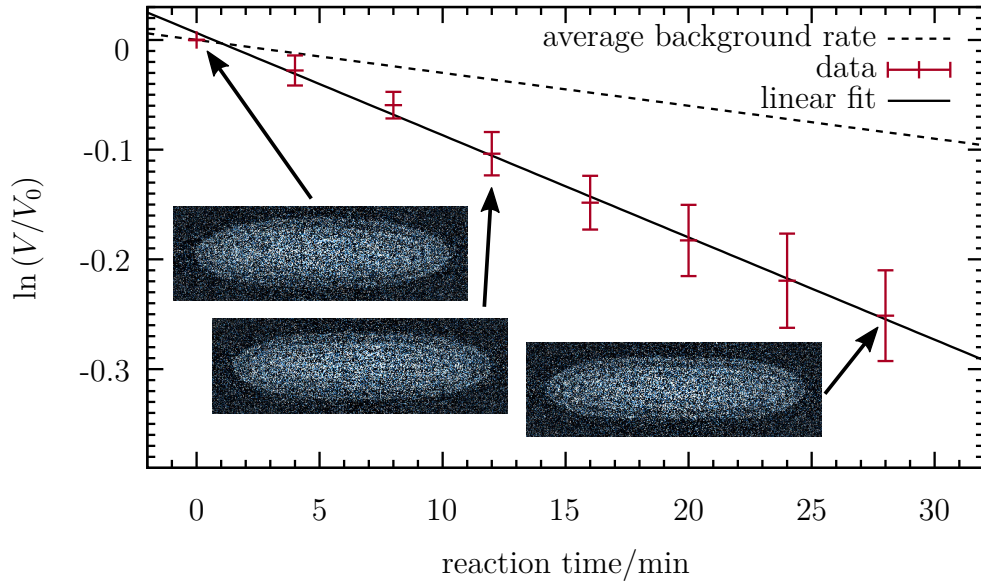


Figure 3.11:  $\text{Ca}^+$ -Rb pseudo-first order reaction rate with the shuttling rubidium cloud at rubidium kinetic energies  $E_{\text{kin}}/k_{\text{B}}$  of 80 mK, corresponding to a collision energy  $E_{\text{coll}}/k_{\text{B}}$  of 25 mK in the  $\text{Ca}^+ - \text{Rb}$  system. Data points represent averages over 4 experiments and error bars indicate one standard deviation  $\pm 1\sigma$ .

Since the atom distribution inside the atom cloud follows a three-dimensional Gaussian distribution and the crystal has the shape of an ellipsoid, the overlap calculation is not straight-forward. On top of that, the atom cloud is flying through the crystal at a  $45^\circ$  angle with respect to the long axis of the ellipsoid. To get a better estimate of the true interaction time, the overlap between the atom cloud and crystal is calculated at various positions as the two pass each other. The overlap factor as explained in section 2.5.2 is then multiplied with the time the atom cloud takes to move between two of the points where the overlap factor is calculated.

Summing up over all these scaled interaction times for enough total distance covered in the calculation (the overlap factor drops off quickly as the distance between the two clouds increases) gives an estimate for the effective interaction time for one shuttling event of 149  $\mu\text{s}$ . Multiplying this effective interaction time by 25 shuttling events per second results in a scaled interaction time factor of approximately 3.7 milliseconds per second, meaning that the interaction time of the crystal with the shuttling atom cloud is reduced by a factor of 1/268 compared to constant overlap with a stationary atom cloud. The measured pseudo-first order reaction rate is also reduced by this factor, thus dividing the pseudo-first order rate constant given in section 3.2.3 by 1/268 gives an estimate of the effective pseudo-first order rate constant as  $k_{\text{pfo}}^{\text{eff}} = 0.043(3) \text{ s}^{-1}$ .

**Density Estimation and Second Order Rate Constant** To calculate the second order rate constant, the effective pseudo-first order rate constant needs to be

---

words, the observed pseudo-first order rate constant is reduced by a factor of over 500 compared to reactions with a constantly overlapped stationary atom cloud.

divided by the density of the atom cloud, but estimating the density of the shuttling atom cloud is not straight-forward. The density in the off-center positions could be measured, but it is not clear how efficient the pushing process is and how many atoms are lost during the free-flight period. One way to estimate the density is to compare the reaction rates observed with already measured second order rate constants from reactions using stationary atom clouds.

Second order rate constants for the reactions between calcium ions and rubidium atoms have been studied in detail in the PhD thesis by Felix Hall [1, 65, 75]. In the experiments performed by Felix Hall, both the atom cloud and ions were stationary and both were constantly laser cooled during their interactions, different from the experiments here, where only the rubidium atoms are laser-cooled during the interaction. This means that in the experiments presented here, the calcium ions will never be reacting in the excited state, but the rubidium atoms can both react in the ground and excited state. In the system with stationary atoms and ions, it was found that the reaction rate is dominated by calcium ions in the excited  $4p\ ^2P_{1/2}$  state and reactions, but ions in the  $4s\ ^2S_{1/2}$  and  $3d\ ^2D_{3/2}$  level are much slower. Because of this, the reaction rate constants  $k_{s,d}$  for these states could only be estimated and only an upper bound of  $k_{s,d} \leq 3 \cdot 10^{-12} \text{ cm}^3\text{s}^{-1}$  is given, compared to the excited state reaction rate constant of  $k_p = 1.5(6) \cdot 10^{-10} \text{ cm}^3\text{s}^{-1}$ . The fraction of rubidium atoms in the excited state had no observable influence on the measured reaction rates.

Another system measured in the work of Felix Hall was the reaction of molecular nitrogen ions sympathetically cooled by a Coulomb crystal of calcium ions with a stationary atom cloud of rubidium. The observed reaction rates were faster than the ones measured in reactions between calcium ions and rubidium atoms. In work done by Alexander Dörfler [130, 131], the reactions between molecular nitrogen ions and rubidium atoms was revisited using the shuttling atom cloud. Using results from these experiments for the reaction rates together with the second order rate constants measured by Felix Hall, the density of the shuttling atom cloud could be determined and was calculated as approximately  $3.15 \cdot 10^8 \text{ cm}^{-3}$ . Dividing the effective pseudo-first order rate constant obtained in the previous paragraph by this density results in a second order rate constant of  $k_{2\text{nd}} = (1.4 \cdot 10^{-10} \pm 9 \cdot 10^{-12}) \text{ cm}^3\text{s}^{-1}$ .

Compared with the upper bound of the second order rate constant in the ground state of the calcium ions of  $k_s \leq 3 \cdot 10^{-12} \text{ s}^{-1}$  as measured by Felix Hall, the value obtained for  $k_{2\text{nd}}$  seems unreasonably high. Using this second order rate constant with the atom density obtained in the reactions of the shuttling atom cloud with  $\text{N}_2^+$  ions in reactions and assuming reactions with a stationary atom cloud, i. e. constant overlap, the expected pseudo-first order rate constant is calculated to be  $9.5 \cdot 10^{-4} \text{ s}^{-1}$ . For a shuttling atom cloud, this would be further reduced by a factor of  $1/268$  as calculated above, resulting in an expected pseudo-first order rate of  $3.5 \cdot 10^{-6} \text{ s}^{-1}$ , which is below the background rate observed with no atom cloud present.

Possible error source arise at every step of these calculations. The measured pseudo-first order rate constants presented above are really low, at the limit of what is measurable on this experiment. The calculation of the overlap factor and the assumptions made for the calculation of the effective interaction time might be off. It also has to be noted that a few months passed between the measurement of the reactions of calcium ions with the shuttling atom cloud and the reaction of nitrogen ions with the shuttling atom cloud used to determine the atom density. However all of these factors can not account for the two orders of magnitude difference in the second-

order rate constant for ground state reactions as measured in the work of Felix Hall and the second order rate constants as measured in reactions of the shuttling atom cloud calculated using the atom density as measured in the nitrogen ion experiments.

The most probable explanation for the reaction rate observed is a local increase in background rubidium present in the chamber when an atom cloud is loaded into the MOT. These background reactions can happen constantly and not just when the atom cloud is shuttling through the ion crystal, which also leads to reactions with calcium in the excited state. Since these reactions are very fast, a small increase in local rubidium density can lead to an increase in the observed rate.

### 3.3 Summary and Conclusion

The results presented here show the first implementation of a new hybrid trap system, directly aimed at better control over collision energies in hybrid trapping experiments. It was shown that the shuttling of an atom cloud between two off-center positions in a magneto-optical trap is a viable method to introduce control over the collision energies inside the hybrid trap. The rubidium kinetic energies could be varied between 50 and 120 mK with good reproducibility. Simulations indicate a comparatively large spread in kinetic energy, which could be improved by reducing the temperature of the atom clouds in the off-center positions. So far, this has proved challenging, as the alignment of the shuttling MOT is very delicate.

It was shown that the observed characteristics of the atom cloud could be well reproduced by simulations, where the only adjustable parameter not directly inferable from the experiment was the stochastic heating force. The time-of-flight traces as well as the dependence of the velocity of the atoms on the push beam power could both be well reproduced.

For the first reaction measurements, the reaction between calcium ions and rubidium atoms was revisited. As laid out in section 3.2.4, the effective interaction time between the atom cloud and Coulomb crystal greatly reduced the expected reaction rate, making the observation of this slow reaction impossible. Fast reactions, such as reactions with molecular ions, can still be measured. The density estimation of the shuttling atom cloud during the free-flight period also remains a challenging problem. Measurements using known second-order rate constants to determine the density of the shuttling atom cloud would optimally be performed alternately with measurements for which one wishes to determine the second order rate constant.



# Chapter 4

## Molecular Oxygen Ions

This chapter discusses progress towards incorporating state-selected molecular oxygen ions into the hybrid trap with the goal of measuring the influence of the internal states such as rotational and vibrational states of the molecular ion on the reaction rate. Initial work on including molecular ions into the hybrid trap was performed by Felix Hall, where nitrogen ions were loaded from nitrogen gas leaked into the chamber [1, 72]. These nitrogen molecular ions were loaded in the vibrational ground state at a thermal rotational-state distribution. When loading from background gas leaked into the chamber, state-selective loading is not possible, as collisions with background nitrogen molecules during loading lead to vibrational and rotational state redistribution. For state selection to work, molecular ions have to be loaded in a collision free environment, conditions only achieved using a molecular-beam setup.

Molecular oxygen ions were chosen as a new reaction target due to promising previous work [99], showing the possibility of the selective generation of vibrational states. Since molecular oxygen ions play an important role in the chemistry of the upper atmosphere, it is already a well-studied system, but so far no studies were performed using selected vibrational states at low collision energies. An overview of previous studies involving molecular oxygen ions can be found in the introduction.

To generate the molecular oxygen ions selectively as reported in [99], the spectrum of the  $1,3\Phi$  states needed to be measured and assigned. For this, a molecular beam setup was built, which was a copy of the beam machine used on another experiment in our lab [97, 98] and is described in section 4.1. Measurements of molecular oxygen spectra performed using the molecular beam setup are described in section 4.2, where also failed loading attempts from the molecular beam are described. Section 4.3 describes preliminary results from reactions using molecular oxygen ions and stationary atom clouds.

### 4.1 Molecular Beam and REMPI Setup

This section describes the molecular beam machine setup, which consists of two differentially pumped vacuum chambers. It was used as a resonance-enhanced multiphoton ionisation (REMPI) spectrometer. The full vacuum chamber setup is shown schematically in Figure 4.1.

The section starts with a description of the first chamber, designated source chamber, where a pulsed molecular beam is formed using piezo valve. Also described is the ionisation chamber, which houses the time-of-flight mass spectrometer setup and

is reached by the molecular beam after passing a skimmer connecting the two chambers. The ionisation chamber houses the repeller electrodes which accelerate the ions, generated by a focused ionisation laser, through a flight tube and onto a microchannel plate detector. The generation of the ionisation laser light used for the REMPI spectroscopy is discussed as well as the experiment control and signal acquisition.

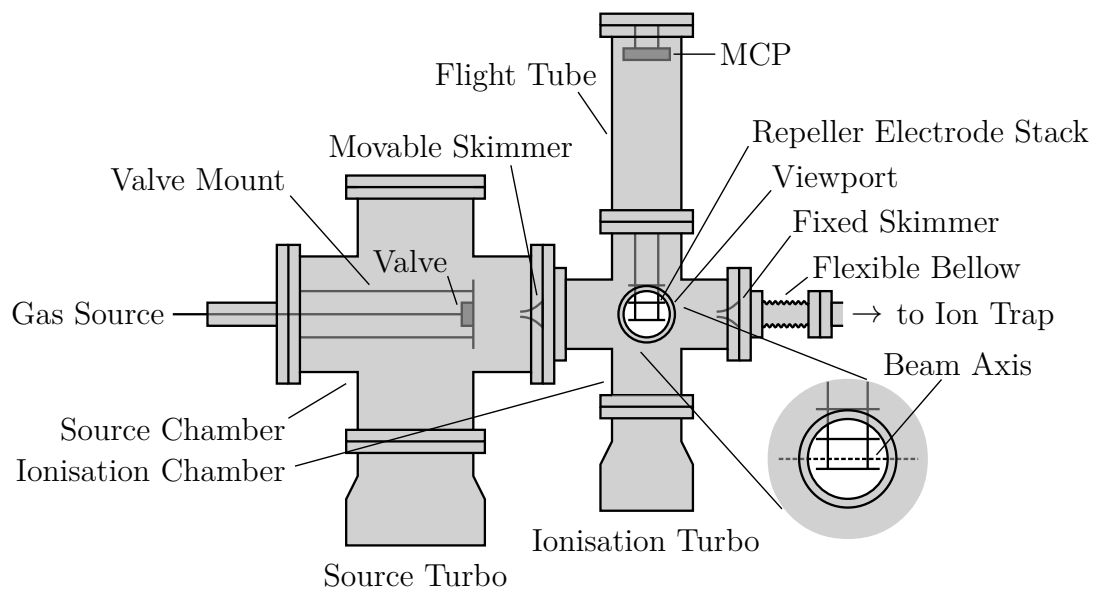


Figure 4.1: The molecular beam machine setup consisting of two connected vacuum chambers. The source chamber on the left houses a pulsed valve on a movable mount. A movable skimmer centred on a flange connects the source chamber to the ionisation chamber on the right. The ionisation chamber houses a standard Wiley-McLaren time-of-flight spectrometer consisting of 3 repeller electrodes underneath a flight tube with a microchannel plate (MCP) at the top. Both chambers have a turbo pump connected to provide the vacuum. A flange with a fixed skimmer at the centre connects the ionisation chamber to the main experiment over a flexible bellow. The whole beam machine is mounted on a movable frame allowing the alignment of the beam machine axis onto the ion trap centre.

#### 4.1.1 Pulsed Valve and Source Chamber

The valve used in the molecular beam machine is a modified piezo valve originally designed by Dieter Gerlich [133]. The valve body is machined from stainless steel. Opening and closing of the valve is achieved by means of piezo actuation, which presses or releases a rubber seal against the opening of the valve. The valve opening diameter is  $300\ \mu\text{m}$  in the form of a straight cone with an opening angle of 40 degrees. A cross-section of the valve is shown in Fig. 4.2.

To operate the piezo, the valve has one electrical connection, which is connected with a wire to an electrical feedthrough. From outside the vacuum, the feedthrough is connected to a custom-built piezo driver box which supplies the 200 V pulses necessary to operate the piezo. The high voltage pulses of the piezo driver box are controlled by a pulse generator controlling the timing of the various parts of the REMPI spectrometer.

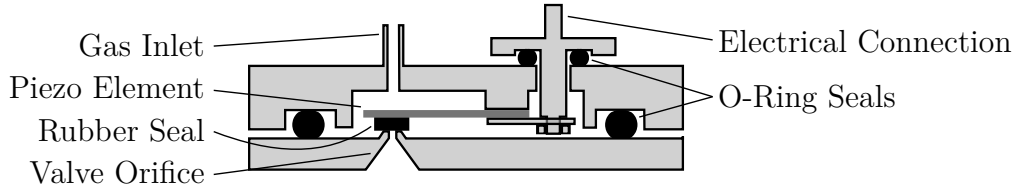


Figure 4.2: A schematic of the piezo valve, reproduced from [133]. The two stainless steel plates are held together by screws and sealed by an O-ring. Another O-ring is used to seal the electrical feedthrough, which is isolated from the steel housing. The piezo element is clamped between the electrode and the steel housing. A piece of rubber glued onto the piezo element seals the valve orifice. The application of 200 V to the piezo element bends it away from the orifice and opens the valve.

The opening time of the valve can be varied from tens of microseconds to as long as desired at repetition rates of up to 3 kHz [133]. For REMPI measurements and ion loading the valve was operated at 10 Hz, limited by the maximum repetition rate of the laser source. Gas pulse length was typically in the range of 1 to 10 ms at backing pressures between 1 and 2 bar overpressure.

The valve is installed inside the source chamber using a three-legged mount built by the mechanical workshop. In theory, the mount allows lateral and vertical movement of the valve as well as moving the valve along the axis of the molecular beam. This works well when outside of vacuum, but under vacuum, the springs providing the force to move the mount horizontally and vertically are not strong enough. Also, trying to move the valve along the axis of the molecular beam twists the whole mount and thus misaligns the valve. A new valve mount is currently under construction.

The base pressure in the source chamber reaches low  $10^{-7}$  mbar with the valve off, whereas valve operation increase the pressure to a few  $10^{-4}$  mbar, depending on the exact settings.

#### 4.1.2 Time-of-Flight Spectrometer and Ionisation Chamber

The time-of-flight spectrometer is housed in the second vacuum chamber, referred to as the ionisation chamber, and is separated from the source chamber by a skimmer on an movable mount, which allows lateral and vertical movement of the skimmer from outside of the vacuum chamber. The skimmer has an opening diameter of 500  $\mu\text{m}$  and can be moved vertically and laterally. The base pressure in the ionisation chamber is in the low  $10^{-8}$  mbar, whereas during valve operation it can reach a few  $10^{-7}$  mbar, depending on the exact settings.

The time-of-flight spectrometer consists of 3 repeller electrodes inside the ionisation chamber, above of which there is a flight tube with a microchannel plate (MCP) at the end. The repeller electrodes are aligned in such a way that the molecular beam passes through the bottom two electrodes, with a third electrode above them. The vertical distance between the bottom and centre electrode is the same as the distance between the centre and the top electrode. The molecular beam passes at a distance of a third from the bottom electrode, see the inset in Figure 4.1.

Each of the electrodes is connected to a high-voltage feedthrough using shielded Kapton coaxial cable. The flight tube is approximately 50 cm long with the MCP

at the end. The MCP is operated at around -2.2 kV, supplied by high-voltage DC power supply (MCP 14-3500, FuG Elektronik GmbH). To accelerate the ions, only the bottom repeller electrode was used, where the high-voltage pulses at 1 kV were supplied by a home-built high-voltage switch controlled by the pulse generator.

On the other side of the ionisation chamber opposite of the movable skimmer, there is a non-movable skimmer (300  $\mu\text{m}$  opening) on a fixed flange. After the skimmer, there is a gate valve, allowing the main vacuum chamber and the beam machine to be operated independently of each other. This second skimmer does not need to be movable, since the whole molecular beam machine rests on a movable frame. The movable frame allows lateral and vertical movement as well as control over the pitch of the beam machine.

### 4.1.3 REMPI Laser Setup

A tunable dye laser (NarrowScan, Radiant Dyes) was used to generate the laser light used for the measurement of the REMPI spectra. The laser was operated with a dye solution containing coumarin 1 (also known as coumarin 47 or 460). This dye is tunable from around 445 nm to 475 nm and after frequency doubling is able to cover the whole range necessary for the measurement of the ground and first two vibrationally excited states of the  $^1,^3\Phi$  states of neutral molecular oxygen in a [2 + 1] REMPI scheme<sup>1</sup>. The dye laser was pumped at 355 nm using the frequency-tripled output of a Nd:YAG laser (SpitLight 1500, InnoLas) at 10 Hz repetition rate. The firing of the flashlamp and the Pockels cell delay of the Nd:YAG laser were both controlled by the pulse generator.

A small fraction of the dye laser fundamental is split off and transported via fibre to a wavemeter (WS6, HighFinesse) for wavelength calibration. The dye laser fundamental is frequency doubled to produce light of around 230 nm. The frequency-doubled output of the dye laser is separated from the fundamental using a single prism and is then guided to the molecular beam machine using right-angle prisms. A 250 mm UV fused silica lens (Thorlabs) in front of the ionisation chamber focuses the laser beam onto the molecular beam. After passing the ionisation chamber, the laser beam is dumped into a thermal power sensor (S302C or S470C, Thorlabs) connected to a power meter (PM100D, Thorlabs).

### 4.1.4 Measurement Control and Signal Acquisition

The whole REMPI setup was controlled from a computer using LabVIEW to interface the various components. The computer connects to the dye laser to scan the wavelength, to the wavemeter to read out and confirm the wavelength of the dye laser, a power meter to measure the power of the ionisation laser, a pulse generator controlling the timing sequences of the REMPI measurements and the oscilloscope for acquisition of the MCP signal.

Four channels of the pulse generator (Digital Delay Pulse Generator model 9528, Quantum Composers) are used for timing control. One channel is used to control the valve by applying a trigger to the high-voltage switch that generates the pulses for the piezo. Two more channels are used to trigger the flashlamp and Pockels cell,

---

<sup>1</sup>The [2 + 1] indicates a two-photon absorption of the neutral oxygen molecule to an intermediate state, from which the molecule is ionised by a third photon of the same wavelength.

where the laser power is controlled with the delay between the flashlamp trigger and the Pockels cell trigger. A fourth channel triggers the high-voltage switch connected to the bottom repeller electrode.

For a REMPI measurement, the computer connects to the dye laser to set the wavelength to the desired value. The wavelength is confirmed using a wavemeter (WS6, HighFinesse) and is corrected iteratively until the desired value is reached, which was necessary as the mechanics of the laser proved to be not reliable enough to consistently reach the correct wavelength. The computer then reads out the amplified MCP signal from the oscilloscope (WaveSurfer 64MXs-A, LeCroy) and integrates the signal. The integrated signal is recorded together with the laser power obtained using a thermal power sensor (S302C or S470C, Thorlabs) connected to a power-meter (PM100D, Thorlabs). The program repeats this process until the wavelength range specified by the user is covered.

## 4.2 Measurements using the Molecular Beam

This section describes the measurements involving the molecular beam machine. First, the resonance-enhanced multiphoton ionisation spectrum of oxygen was measured, specifically the spectrum of the ground and first two vibrationally excited  ${}^3\Phi_{2,3}$  Rydberg states. These states were first described in the group of Chupka [113,114]. Also presented is the alignment of the components of the molecular beam machine, as well as the alignment of the beam machine axis onto the ion trap centre. The section is concluded by showing failed attempts of efficient loading using the molecular beam machine.

### 4.2.1 O<sub>2</sub> REMPI Spectra Analysis and Interpretation

The spectra were recorded using a LabVIEW program, described in appendix B.3.2. For the measurements, the backing pressure on the valve was set to around 2 bar of pure oxygen. Opening time of the valve was 10 ms at a repetition rate of 10 Hz, leading to a background pressure of around  $1.4 \cdot 10^{-4}$  mbar in the source chamber. The ionisation laser was delayed by 7 ms with respect to the start of the valve opening and typical laser powers after passing the molecular beam machine were between 5 and 9 mW.

A typical time of flight (TOF) trace is shown in Figure 4.3, where the flight time has been converted to the mass-to-charge ratio of the ions. There is a clear and strong peak at 32 amu/e (atomic mass units per elementary charge unit), corresponding to molecular oxygen ions O<sub>2</sub><sup>+</sup>. Other peaks most probably correspond to mineral oil impurities in the vacuum chamber originating from the oil backing pumps that were used on the setup initially.

To obtain a spectrum, the peak corresponding to molecular oxygen in the TOF trace was integrated while scanning the wavelength of the ionisation laser. The spectrum of the vibrational ground state of the O<sub>2</sub>  ${}^3\Phi_{2,3}$  state was measured at a fundamental ionisation laser frequency of around  $21210 \text{ cm}^{-1}$  (471.5 nm) corresponding to transition frequencies around  $84840 \text{ cm}^{-1}$ . The first vibrationally excited state was measured around  $21680 \text{ cm}^{-1}$  (461.3 nm) for transition frequencies around  $86720 \text{ cm}^{-1}$  and the second vibrationally excited state was measured around  $22140 \text{ cm}^{-1}$  (451.7 nm) for transition frequencies around  $88560 \text{ cm}^{-1}$ . For each of these states, the wavelength

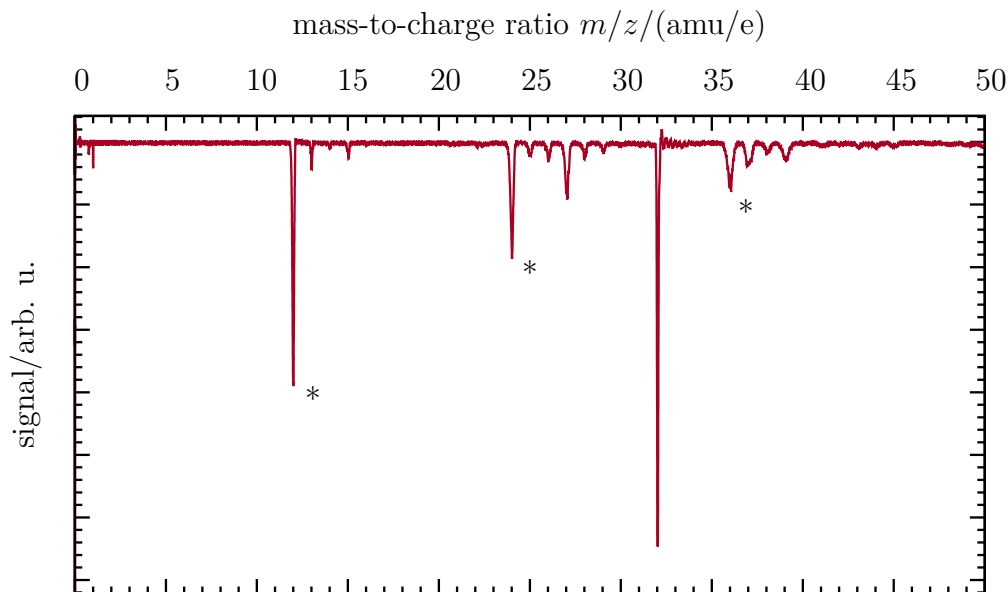


Figure 4.3: Time-of-flight trace, where the flight time has been scaled to mass over charge  $m/z$  in units of atomic mass units per elementary charge units (amu/e). The peak at 32 amu/e corresponds to molecular oxygen ions at a flight time of approximately 9  $\mu$ s. The background peak progressions marked with an asterisk (\*) most probably correspond to  $C^+$ ,  $C_2^+$  and  $C_3^+$  fragments with varying numbers of hydrogen atoms attached. These fragments are formed by the ionisation laser dissociating mineral oil traces in the vacuum chamber originating from the foreline oil pump.

of the fundamental was scanned over approximately  $50 \text{ cm}^{-1}$  to cover the relevant part of the spectrum.

The measured spectra were assigned according to calculations presented in section 2.2.5. Molecular constants used in the calculations were obtained from Herzberg for the ground state [115], whereas values determined in the work of Chupka and co-workers were used for the excited states [113, 114]. The three measured spectra and their assignments are summarised in Figures 4.4 to 4.6.

## 4.2.2 Molecular Beam Alignment and Failed Loading

The whole alignment process consisted of two steps. First, the molecular beam machine components (the valve and two skimmers) need to be aligned with respect to each other and then in a second step, the axis of the beam machine needs to be aligned onto the ion trap centre. Both these steps were performed by aligning a pilot laser through the molecular beam machine and then align the beam machine onto the fibre at the centre of the ion trap. The molecular beam was aimed at a crystal at the trap centre to confirm the alignment using the heating effect of gas molecules colliding with the ions (see below).

To align the movable skimmer, the beam machine was separated from the main chamber and vented. The flange holding the valve and its mount was removed and the pilot laser was aligned through the centre of the open flanges on both ends of the beam machine. The position of the movable skimmer was then optimised by observing

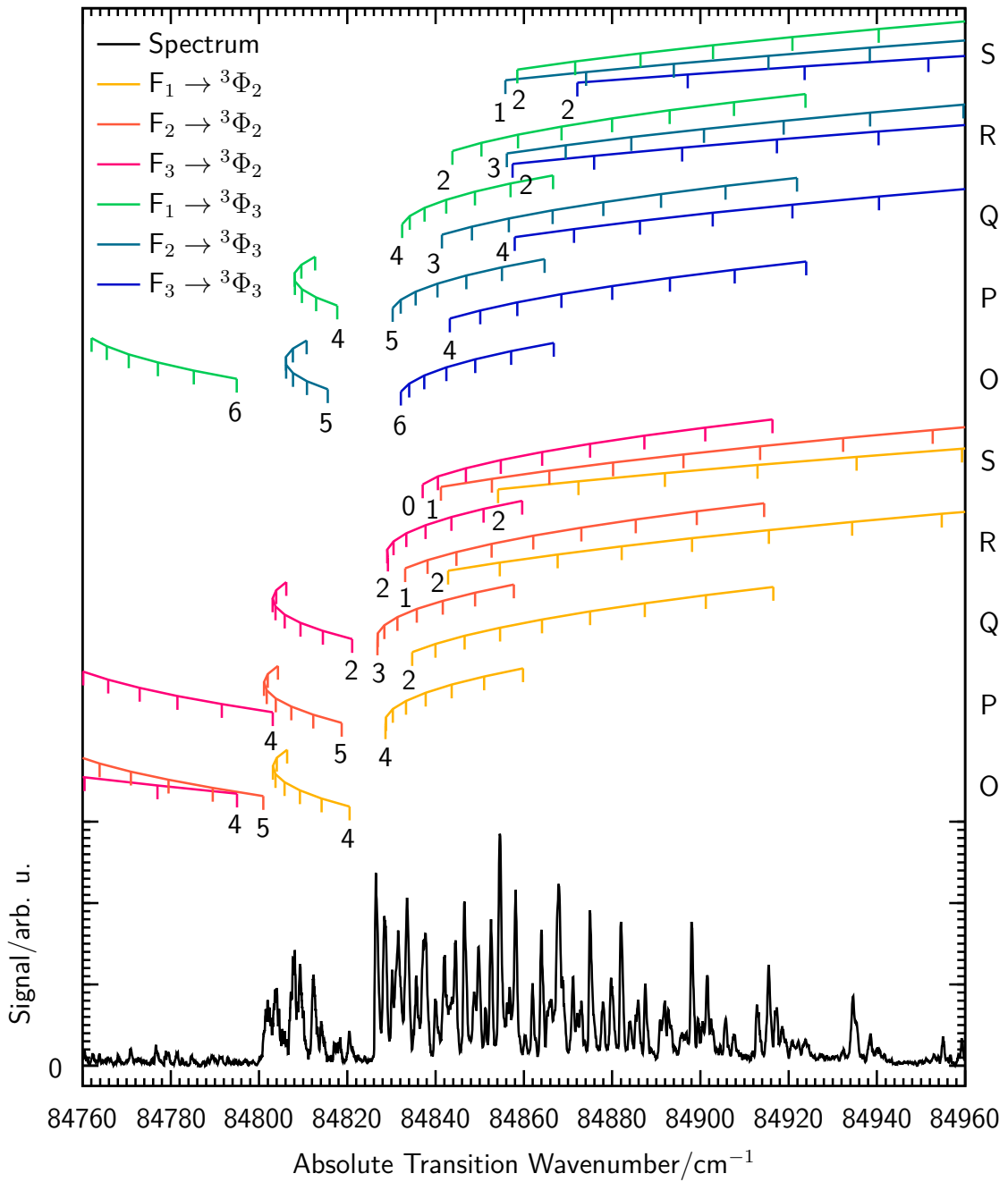


Figure 4.4: Measured spectrum of the  $\text{O}_2$   ${}^3\Phi_{2,3}$  ( $\nu = 0$ ) state in black at the bottom. Assignments at the top are separated into transitions to the  ${}^3\Phi_2$  and  ${}^3\Phi_3$  states and split for the O, P, Q, R and S transitions, where colours indicate which spin-rotation component  $F_i$  in the ground state is addressed. Numbers next to the first transition in each rotational progression indicate the lowest rotational quantum number addressed in the ground state.

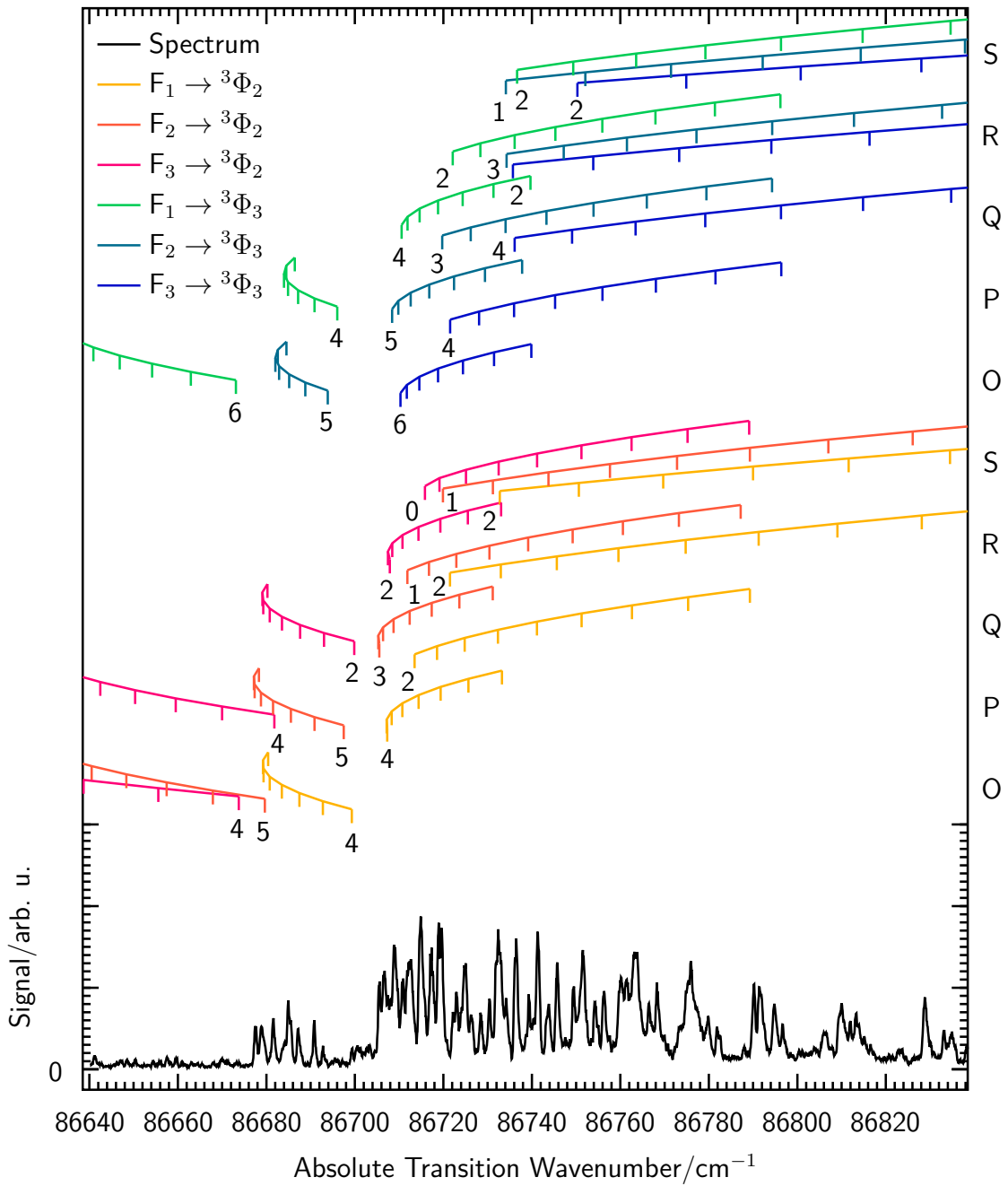


Figure 4.5: Measured spectrum of the  $O_2$   ${}^3\Phi_{2,3}$  ( $\nu = 1$ ) state in black at the bottom. Assignments at the top are separated into transitions to the  ${}^3\Phi_2$  and  ${}^3\Phi_3$  states and split for the O, P, Q, R and S transitions, where colours indicate which spin-rotation component  $F_i$  in the ground state is addressed. Numbers next to the first transition in each rotational progression indicate the lowest rotational quantum number addressed in the ground state.

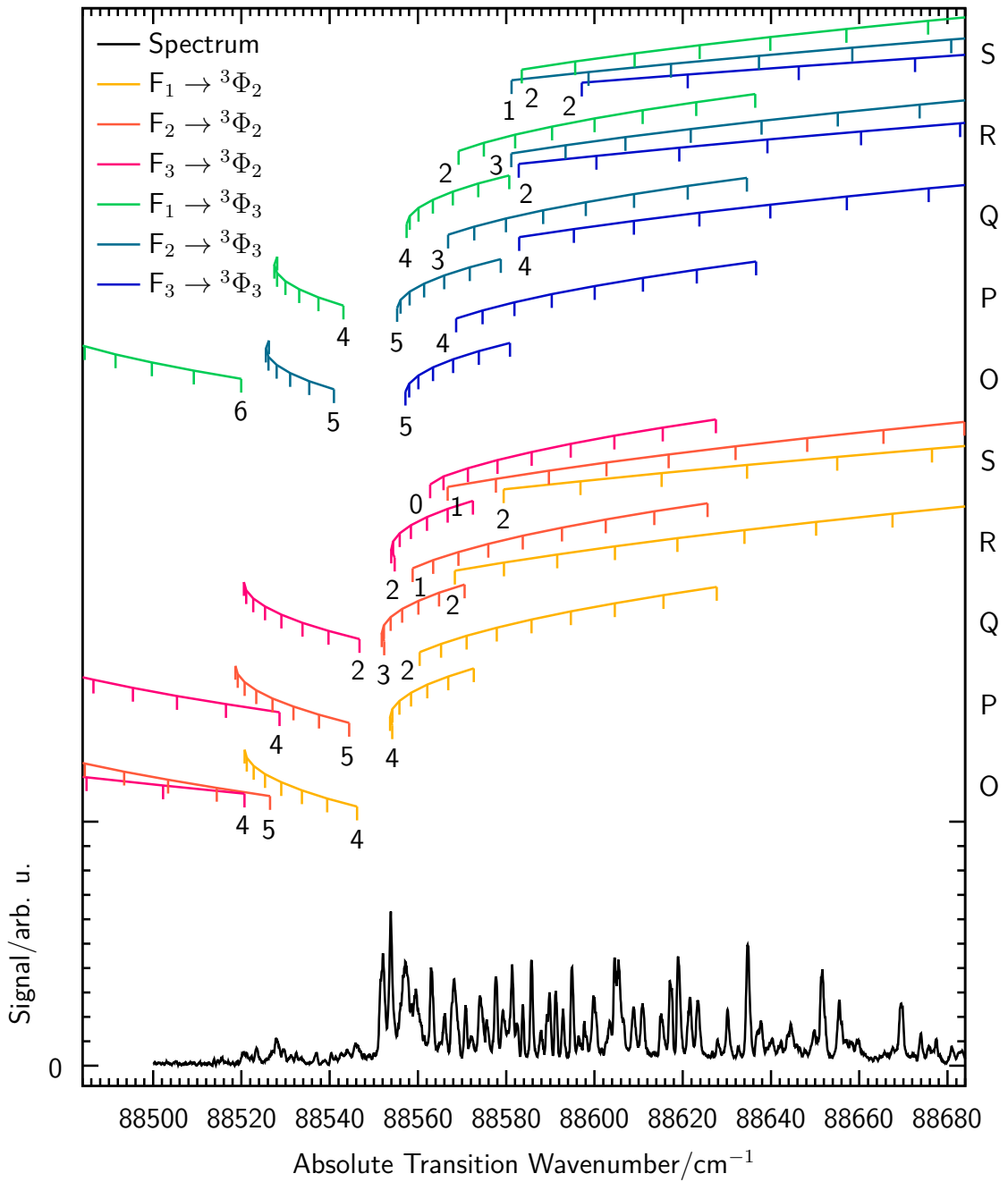


Figure 4.6: Measured spectrum of the  $\text{O}_2$   ${}^3\Phi_{2,3}$  ( $\nu = 2$ ) state in black at the bottom scaled by a factor of 3 compared to the previous two figures. Assignments at the top are separated into transitions to the  ${}^3\Phi_2$  and  ${}^3\Phi_3$  states and split for the O, P, Q, R and S transitions, where colours indicate which spin-rotation component  $F_i$  in the ground state is addressed. Numbers next to the first transition in each rotational progression indicate the lowest rotational quantum number addressed in the ground state.

the beam on a beam profiler (BC106N-VIS/M, Thorlabs) installed at the end of the beam machine.

Then, with the pilot laser still aligned, the beam machine was closed using a large viewport in place of the flange with the valve. The other end of the beam machine was connected to the main vacuum chamber. After pumping the beam machine over night, the gate valve between beam machine and main chamber was opened. The EMCCD camera and microscope were removed and a beam profiler (BC106N-VIS/M, Thorlabs) was put in their place. With this setup, the pilot laser was aligned onto the fibre in the trap centre using the beam profiler to observe the shadow cast by the fibre and the diffraction pattern of the laser.

During this alignment process, it was found that the lateral movement of the beam machine is not perfectly parallel, but there is also a yaw movement where the beam machine twists around its vertical axis. In other words, when moving the beam machine laterally, the front moves less compared to the back, because the movement is constrained by the flexible bellow connecting the beam machine to the main chamber. A lateral movement of 9 mm at the back of the beam machine corresponds to a movement of the beam axis at the ion trap center of approximately 4 mm at the position of the fibre.

To confirm the alignment after reinserting the valve inside the source chamber, the molecular beam was aimed at a crystal at the fibre position. The gas molecules in the beam hit the crystal and heat the ions. Depending on the laser cooling settings for the ions, this heating can be observed as a darkening of the fluorescence and increased blurriness of the ions in the images. As is shown in Figure 4.7, no heating was observed when the beam machine was moved laterally, off-setting the beam from the crystal. This confirmed the presence of the beam and proper alignment.

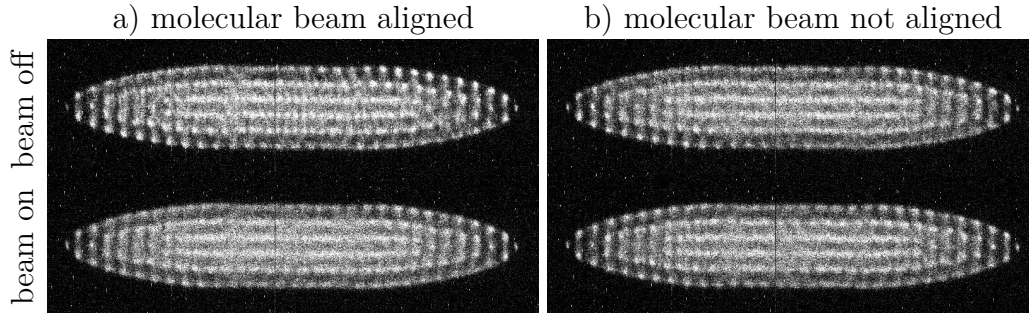


Figure 4.7: Molecular beam alignment using Coulomb crystals. a) Molecular beam aligned with the ion trap centre. Blurring due to heating of the ions is observed in the bottom image, where the molecular beam is present versus the top image, where the molecular beam is turned off. b) The molecular beam machine is moved to the left, which makes the molecular beam miss the trap centre. No difference in appearance of the crystal is observed whether the molecular beam is turned off or on.

While trying to load from the molecular beam, it was discovered that the wavelength used for ionisation of the molecular oxygen also produces a lot of dark ions when there is no oxygen present. These dark ions most likely correspond to fragments of the form  $C_nH_m^+$  with  $n = 1$  and  $m = 0 - 3$  or  $n = 2$  and  $m = 0 - 5$  which form when

mineral oil present in the vacuum chamber<sup>2</sup> is dissociated by the UV laser (see the background ions in the TOF spectrum in Fig. 4.3). This is a problem if the loading rate from the beam is slow. During all attempts of loading from the molecular beam no significant increase in loading rate was observed with the molecular beam present compared to loading from the background. Figure 4.8 shows the best achieved loading rates compared to loading rates from background.

The too slow loading rate was attributed to a too low density generated by the valve. Compared to previous experiments on a similar setup in our group with the same type of piezo valve [98], the distance between the valve and the ion trap center is increased from approximately 80 cm to 120 cm due to constraints in the vacuum setup, which reduces the density of the molecular beam at the trap center. Additionally, their valve had an orifice diameter of 800  $\mu\text{m}$ , which results in larger particle densities. The particle density in a super-sonic expansion at a position  $x$  behind a valve with a backing particle density of  $N_0$  can be estimated as [134]

$$N(x) = N_0 \left( 1 + \frac{\gamma - 1}{2} M(x)^2 \right)^{-\frac{1}{\gamma-1}}, \quad (4.1)$$

where  $\gamma = c_P/c_V$  is the ratio of specific heats ( $\gamma = 7/5$  for  $\text{O}_2$  and  $\text{N}_2$ ).  $M(x)$  is the Mach number at position  $x$ , which for  $\gamma = 7/5$  and a valve orifice diameter  $d$  is estimated as

$$M(x) = 3.65 \left( \frac{x}{d} - 0.4 \right)^{2/5} - 0.82 \left( \frac{x}{d} - 0.4 \right)^{-2/5}. \quad (4.2)$$

Combining equations (4.1) and (4.2) with the parameters in the present experiment of a valve orifice diameter of  $d = 300 \mu\text{m}$ , a beam travel distance  $x = 120 \text{ cm}$  and a backing pressure of 2 bars at room temperature, this results in an estimated beam density of  $\approx 2.7 \cdot 10^{11} \text{ cm}^{-3}$ . Using the parameters of the other experiment in our group of  $d = 800 \mu\text{m}$ ,  $x = 80 \text{ cm}$  and a backing pressure of 1.5 bars [98], the beam density at the trap center is estimated as  $\approx 3.2 \cdot 10^{12} \text{ cm}^{-3}$ , which is over an order of magnitude higher.

### 4.3 Reactions using $\text{O}_2^+$ in the Vibrational Ground State

As described in section 4.2.2, loading from the molecular beam was possible, but the loading rate was too slow and loading unwanted ions from background was comparably fast. This section describes experiments using molecular oxygen ions loaded from oxygen gas leaked into the chamber. Due to collisions during the loading rotationally state-selective loading was made impossible, but the vibrational ground state of molecular oxygen ions could be studied.

First, the loading from molecular oxygen ions is discussed and compared with loading from background or with nitrogen gas present. As introduced in section 2.6, reactions with xenon gas to ensure that loaded molecular oxygen ions are in the vibrational ground state are presented. Then, a summary of reactions of the stationary rubidium MOT at different laser-cooling parameters leading to a range of excited-state

---

<sup>2</sup>Mineral oil is present due to the foreline rotary vane pump using oil. This pump has since been replaced by an oil-free pump stand using a combination of a membrane pump and a turbo pump.

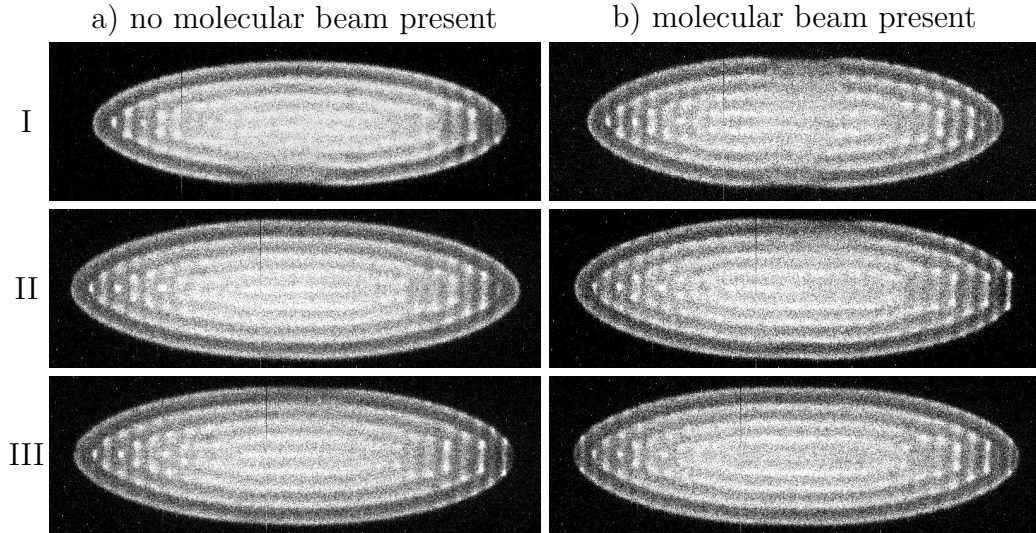


Figure 4.8: Loading from the molecular beam was difficult. a) Turning the oxygen ionisation laser on for 15 s loads light ions from background. In all three experiments, approximately the same amount of light ions was loaded. b) Loading with the molecular beam present will result in loading from the beam, but the amount of ions loaded is not reproducible and just barely above background.

population fractions intended to probe the influence of the excited state of rubidium on the reaction rate is shown. The section is concluded with a discussion on the observed reactivity, where long-range effects as well as short-range effects in terms of energy levels of the different entrance and exit channels in the  $\text{O}_2^+ + \text{Rb} \rightarrow \text{O}_2 + \text{Rb}^+$  reaction system are compared to previous measurements of  $\text{N}_2^+ + \text{Rb}$  in this setup.

### 4.3.1 Loading and Vibrational State Determination

Molecular oxygen ions were loaded from background by leaking  $\text{O}_2$  gas into the hybrid trap chamber and focussing the ionisation laser beam into the trap centre using a 500 mm UV fused silica lens (Thorlabs). The ionisation laser was tuned to the transition of the  $^3\Phi$  ( $\nu = 1$ ) Rydberg state, as more laser power was available there compared to transitions to the  $\nu = 0$  vibrational state leading to more efficient loading. In Figure 4.9, loading rates from leaking either background  $\text{O}_2$  or  $\text{N}_2$  gas into the chamber are compared to loading from background. The loading rate with leaked  $\text{O}_2$  is by far the highest, confirming the loading of mostly  $\text{O}_2^+$  ions into the Coulomb crystal.

Loading molecular oxygen ions from background gas leads to collision of the ions with neutral molecules during the loading process. Some of these collisions can result in quenching of the vibrational state of the ionic molecule. Böhringer and co-workers examined the collision between molecular oxygen ions and various neutral molecules including neutral molecular oxygen [123]. They state a Langevin collision rate of  $7.4 \cdot 10^{-10} \text{ cm}^3\text{s}^{-1}$  and a quenching rate from the first vibrationally excited state to the ground state of  $3 \cdot 10^{-10} \text{ cm}^3\text{s}^{-1}$ . At  $\text{O}_2$  background pressures of around  $1.5 \cdot 10^{-8} \text{ mbar}$ , this corresponds to a quenching rate of  $0.11 \text{ s}^{-1}$ .

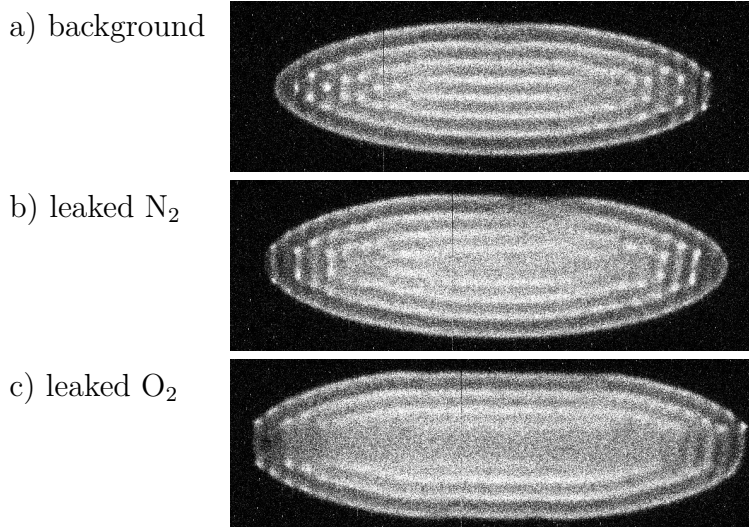


Figure 4.9: Loading with the ionisation laser for 15 s. a) Loading with no gas leaked into the chamber is slow and only very few light ions are loaded from the background gas present in the chamber. b) As a control experiment, nitrogen gas at a pressure of approximately  $1.5 \cdot 10^{-8}$  mbar was leaked into the chamber while trying to load with the ionisation laser. Compared to background, some more ions were loaded, possibly trace amounts of oxygen left over in the gas line. c) Leaking in oxygen at a pressure of approximately  $1.5 \cdot 10^{-8}$  mbar results in many more light ions being loaded into the trap, most of which are molecular oxygen ions.

The high background O<sub>2</sub> pressure during loading ensured quenching of all molecular oxygen ions to their vibrational ground state. During the usual loading times of around 10 to 20 s, this creates molecular oxygen ions in the vibrational ground state even though they are ionised using the first vibrationally excited intermediate state. To confirm that the molecular oxygen ions are in the vibrational ground state, xenon gas was leaked into the chamber, which reacts with molecular oxygen ions if they are vibrationally excited, but not if they are in the vibrational ground state, as explained in section 2.6. As presented in Figure 4.10, this was confirmed by observing few to no reactions when xenon gas was leaked into the chamber, indicating that indeed molecular oxygen in the vibrational ground state was loaded.

### 4.3.2 Reactions with a Stationary Atom Cloud

The goal of these experiments was to measure the reaction rate of molecular oxygen ions in the vibrational ground state with rubidium atoms in varying excited state populations. For this, atom clouds at different laser cooling settings were generated by varying the detuning and power of the MOT cooling laser beams. At a detuning of 10 MHz, atom clouds were generated at powers of 1 mW, 2 mW, 3 mW and 4 mW on each of the arms of the MOT, while at 15 MHz detuning, atom clouds were generated at 3 mW and 5 mW. The resulting calculated excited state fractions according to equation (2.14) are summarised in Table 4.1. For each of these MOT cooling settings, 12 reactions with molecular oxygen ions were performed.

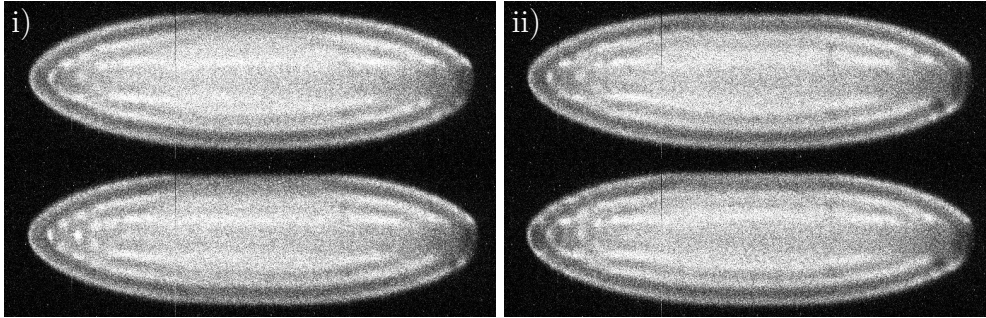


Figure 4.10: Using xenon to determine the vibrational state of the molecular oxygen ions after loading. After loading molecular oxygen ions during 15 s at a pressure of  $1.5 \cdot 10^{-8}$  mbar, xenon gas was leaked into the chamber at a pressure of  $1.5 \cdot 10^{-8}$  mbar for several minutes. Two examples are shown. The upper images are after loading molecular oxygen ions and the bottom images are after 5 minutes of interaction with xenon. As can be seen, the reaction of only a few molecular oxygen ions i) or none ii) is observed, confirming that most molecular oxygen ions are quenched to the vibrational ground state during loading.

Table 4.1: A summary of cooling beam power  $P$  and detuning  $\delta$  resulting in calculated excited state fractions  $\rho_{ee}$  following equation (2.14) for all six measurement series.

$P$	$\delta$	$\rho_{ee}$
1 mW	10 MHz	7.5%
3 mW	15 MHz	9.6%
2 mW	10 MHz	13.5%
5 mW	15 MHz	14.5%
3 mW	10 MHz	17.5%
4 mW	10 MHz	20.8%

For every MOT cooling setting, the cooling lasers needed to be optimised again to ensure well-formed atom clouds at the right position. Overlap between atom cloud and Coulomb crystal in the image plane of the EMCCD camera is straight-forward, as both species can be imaged on this camera. For overlap verification out of plane of the EMCCD's image plane, two methods were used in conjunction. The top-down imaging system is not sensitive enough to image the ions, so the overlap needed to be checked indirectly using the fibre tip that can be inserted into the ion trap centre. By illuminating the tip with 780 nm laser light the position of the fibre tip can be imaged on the top-down imaging system (see Figure 3.1), which can then be compared with the position of the atom cloud. As the resolution of this imaging system is much lower than the EMCCD, the overlap was also confirmed using the 397 nm to deplete the atom cloud. As explained in section 2.2.4, rubidium atoms in the excited state can be ionised by 397 nm photons. If the atom cloud is overlapped with the 397 nm laser beam, atoms will be lost from the trap due to the aforementioned effect. This decreases the fluorescence of the atoms significantly. By comparing the fluorescence

level with and without 397 nm laser present, the overlap between the the atom cloud and the ion trap centre can be estimated and compared during experiments.

Ions were loaded at around  $6 \cdot 10^{-8}$  mbar of oxygen gas leaked into the chamber during 10 s of illumination of the fundamental of the REMPI laser tuned to  $21678.8 \text{ cm}^{-1}$ , which corresponds to a term energy of  $86715.2 \text{ cm}^{-1}$ . Typical laser powers during loading were from 6 to 8 mW. To ensure enough time for quenching all molecular oxygen ions to the vibrational ground state, oxygen pressure was kept at this high level for another 20 s after loading. The quenching rate of the first vibrational state to the ground state at the  $\text{O}_2$  loading pressure is approximately  $0.44 \text{ s}^{-1}$ , corresponding to a half-life time of 1.6 s.

After the ions were loaded, the rubidium atom source was turned on for 3 minutes to ensure reaching equilibrium temperature of the atom source.<sup>3</sup> After this time passed, the crystal was moved axially away from the trap centre and the cooling lasers of the MOT were turned on for 30 s to form an equilibrated atom cloud. As equilibrium of the atom cloud was reached, the crystal was moved back to the trap centre and immediately images were started to be recorded in 1 s intervals.

After all the molecular oxygen ions had reacted away, images of the atom cloud were taken and all MOT cooling laser beam powers were recorded. An additional set of images of the atom cloud and depleted atom cloud using the 397 nm laser as explained above was recorded to ensure continuous overlap over the course of a measurement series. After some of the reactions, mass spectra of the crystal were recorded using resonance-excitation mass spectrometry to determine the product species.

### 4.3.3 $\text{O}_2^+ + \text{Rb}$ Reaction Rate Measurements Summary

To analyse the recorded data described in the previous section, the pseudo-first order rate constants had to be determined, for which the volume occupied by the molecular oxygen ions over time needs to be determined. They form a string in the middle of the crystal creating a dark core (see Figure 4.10), whose volume is proportional to the length of the cylinder occupied by the molecular oxygen ions. It is thus enough to determine the length of the dark core and plot the logarithm of the length of the core  $L$  divided by the length of the core at the start of the reaction  $L_0$  against time to carry out the reaction rate determination as described in section 2.5.1.

Atom densities were determined from the atom cloud images taken after every measurement together with the laser powers recorded. A LabVIEW program was written to automatically analyse a full dataset consisting of images and a single text file containing the laser powers for every measurement. The program reads in the laser powers from the file, fits a two-dimensional Gaussian distribution to the atom cloud images and together with the photon counts of the EMCCD camera determines the atom number and density of the atom cloud. To calculate the overlap factor as described in section 2.5.2, a second program using the same two-dimensional Gaussian fitting routine was used with an interface to approximate the volume of the molecular ions inside the Coulomb crystal by hand.

---

<sup>3</sup>It is not expected that the molecular oxygen ions are affected during this time. The three gases with highest partial pressures and masses lower than calcium present in the vacuum chamber are  $\text{H}_2$ ,  $\text{H}_2\text{O}$  and  $\text{N}_2$ .  $\text{H}_2$  does not react with  $\text{O}_2^+$  in the ground state [135] and also  $\text{H}_2\text{O}$  does not react [123]. The ionisation potential of  $\text{N}_2$  is too high for reactions to occur.

From the pseudo-first order rate constants, the average densities and the overlap factors, the second order rate constants could be determined for every measurement, a summary of which can be found in Figure 4.11. The average reaction rate over all different measurement series was found to be  $3.00 \cdot 10^{-9} \pm 1.40 \cdot 10^{-9} \text{ cm}^3\text{s}^{-1}$ , which is very close to the Langevin collision rate that was calculated as  $3.33 \cdot 10^{-9} \text{ cm}^3\text{s}^{-1}$  for the  $\text{O}_2^+ + \text{Rb}$  system. The population of rubidium atoms in the excited state does not seem to influence the reaction rate. Using the method devised by Felix Hall [1], the extended theoretically expected excited-state rate including charge-quadrupole interactions to account for the quadrupole moment of rubidium in the  $^2\text{P}_{3/2}$  state (see section 2.1.4) was calculated as  $k_p^{\text{th}} = 1.66 \cdot 10^{-8} \text{ cm}^3\text{s}^{-1}$  at an average collision energy of  $E_{\text{coll}}/k_B = 20 \text{ mK}$ .

The systematic uncertainties of the second order rate constant calculations was estimated by Gaussian propagation of uncertainty and found to be between 33 % and 37 % for the different measurement series. The main source of systematic uncertainty is the atom number determination that was discussed in section 2.3.3. The total uncertainty was estimated as the root-mean-square value of the systematic uncertainty and statistical standard deviation. The vertical error bars in Figure 4.11 represent the total uncertainty.

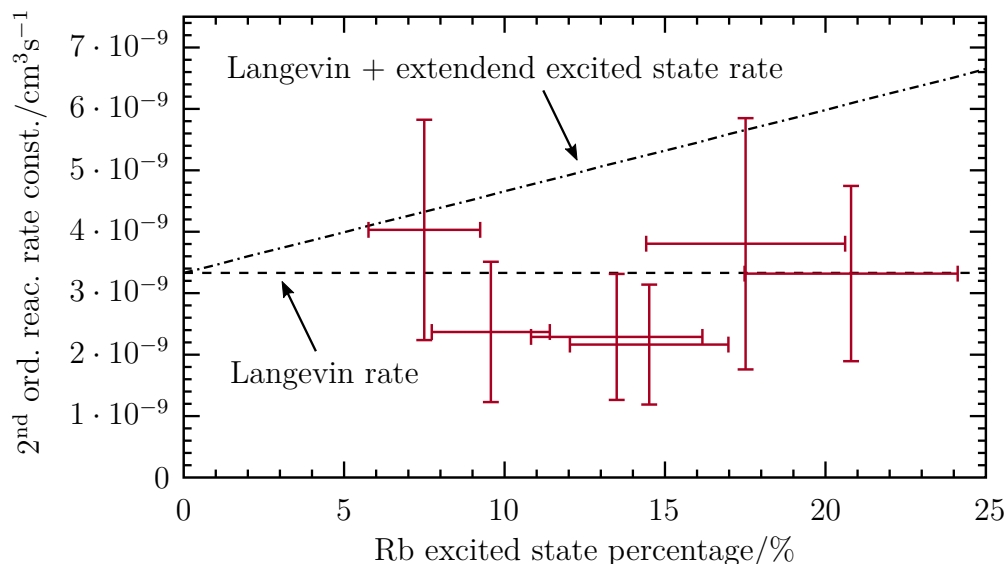


Figure 4.11: Summary of the reactions between sympathetically cooled molecular oxygen ions and stationary rubidium atoms in the hybrid trap. Intensities and detuning of the MOT cooling laser beams have been varied to achieve different excited state populations in the atom cloud. The dashed line indicates the magnitude of the Langevin collision rate in this reaction. Taking into account the extended excited state reaction rate as discussed in section 2.1.4, the dashed-dotted line is obtained, which predicts an increase in the reaction rate at higher excited state fractions. The measured reaction rate data in red does not seem to follow a trend with regard to the excited state population. The vertical error bars indicate the total error estimated from the root mean square of systematic uncertainty and one statistical standard deviation. Horizontal error bars indicate the systematic uncertainty in the excited state population.

### 4.3.4 Reaction Product Analysis

After some of the reactions, mass spectra were recorded using resonant excitation mass spectrometry (REMS) to identify reaction products. For each of these measurements, a mass spectrum of the pure calcium crystal before  $\text{O}_2^+$  loading was recorded as a reference spectrum. After loading  $\text{O}_2^+$  and letting it react away completely, a second mass spectrum was recorded for the identification of reaction products. In a next step, all the heavy product ions cooled by the crystal were ejected by lowering the amplitude of the trapping radio-frequency to a point where calcium ions are still stably trapped, but the heavier product ions are not trapped and thus ejected from the trap. Rubidium ions were then loaded from background by simultaneously letting the 397 nm and 780 nm laser and another mass spectrum was recorded. This mass spectrum indicates that the only product ions observed in reactions between molecular oxygen ions and rubidium atoms are rubidium ions, as this spectrum looks identical to the one recorded with the product ions. The three mass spectra are shown in Figure 4.12.

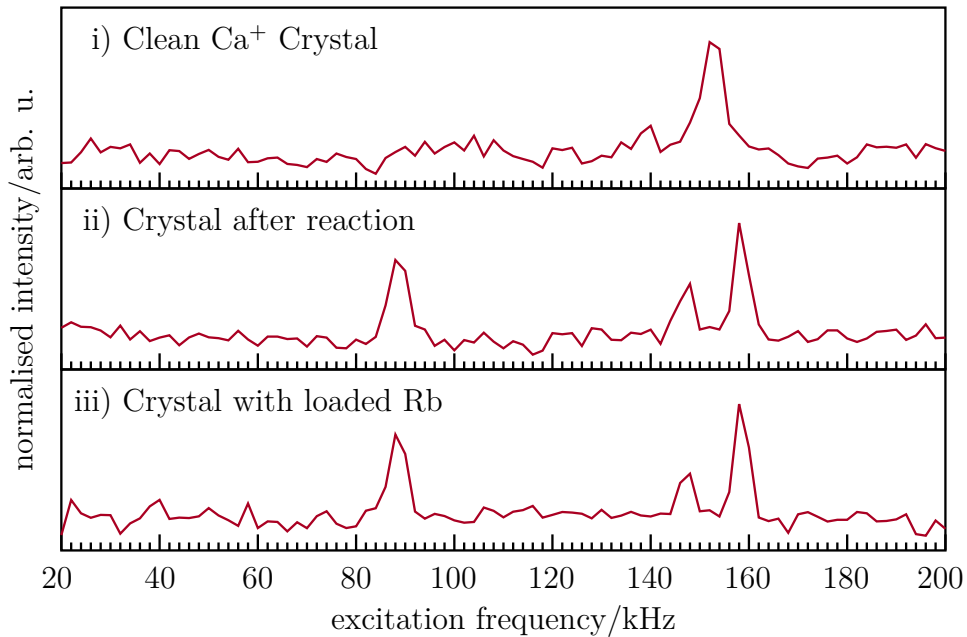


Figure 4.12: Resonance-excitation mass spectra of different Coulomb crystals for the determination of product ions in the  $\text{O}_2^+ + \text{Rb}$  reaction. i) Reference spectrum of a Coulomb crystal containing only calcium ions. The single peak corresponds to the radial frequency of the calcium ions in the trap. ii) Spectrum after all previously loaded molecular oxygen ions have reacted away with rubidium atoms. iii) After cleaning the heavy product ions of the crystal of the second spectrum, rubidium ions were loaded from background by simultaneously letting the 397 nm and 780 nm into the vacuum chamber. The spectra in ii) and iii) are identical, indicating no other products than  $\text{Rb}^+$  are formed.

### 4.3.5 Possible Reaction Mechanisms

As presented in section 4.3.3 and summarised in Figure 4.11, the measured reaction rates do not seem to be influenced by the excited state population of the rubidium atoms in the atom cloud. This stands in contrast to the measurements of molecular nitrogen ions with rubidium atoms performed on this setup by Felix Hall, where the fraction of rubidium atoms in the excited state seemed to dominate the reactions [1, 72].

**Summary of Previous  $\text{N}_2^+ + \text{Rb}$  Measurements** The channel-averaged rate constant in the  $\text{N}_2^+ + \text{Rb}$  system was reported as  $k_{2\text{nd}} \approx 2 \cdot 10^{-9} \text{ cm}^3\text{s}^{-1}$  [1], a value similar to the one reported above for the  $\text{O}_2^+ + \text{Rb}$  system. For the  $\text{N}_2^+ + \text{Rb}$  system, the second order rate constant was found to increase in reactions with a larger fraction of rubidium atoms in the excited state. A fit of the measured excited-state-dependent reaction rates to a rate equation model yielded a rate constant of  $k_p = 2.4 \cdot 10^{-8} \pm 1.3 \cdot 10^{-8} \text{ cm}^3\text{s}^{-1}$  for rubidium atoms in the excited state and an upper bound for the ground state rate of  $k_s \leq 2 \cdot 10^{-10} \text{ cm}^3\text{s}^{-1}$ .

The measured upper bound for the reaction rate constant  $k_s$  of the  $\text{N}_2^+ + \text{Rb}$  system for rubidium atoms in the ground state is over an order of magnitude lower than the calculated Langevin collision rate constant of  $k_L^{(s)} = 3.5 \cdot 10^{-9} \text{ cm}^3\text{s}^{-1}$ . This discrepancy was explained by the inefficiency of the charge transfer, as the closest product channel in the neutral nitrogen molecule was the  $\text{C } ^3\Pi_u$  valence state which requires a reordering of the electron configuration for the reaction to happen. Additionally, there is a relatively large difference in energy between the entrance and the exit channel to form neutral nitrogen molecules in the C state [1]. Previous studies of keV molecular nitrogen ions reacting with caesium atoms in a gas cell already reported that charge transfer is most efficient for transfer of the electron into a Rydberg orbital in a near-resonant process [136].

The reaction rate constant  $k_p$  of the  $\text{N}_2^+ + \text{Rb}$  system for rubidium atoms in the excited state was found to be approximately four times larger than the Langevin collision rate constant in the excited state of  $k_L^{(p)} = 6.6 \cdot 10^{-9} \text{ cm}^3\text{s}^{-1}$ . The Langevin rate constant  $k_L$ , which usually determines an upper bound for the interaction rate in a given ion-neutral system, only assumes interactions between charge and induced-dipole and gives a collision-energy independent estimate for the collision rate constant. To explain the large magnitude of the reaction rate of rubidium atoms in the excited state  $k_p$ , an additional intermolecular interaction had to be taken into account. The anisotropic charge distribution of the  $^2\text{P}_{3/2}$  state in rubidium gives rise to a quadrupole moment, which results in an additional charge-quadrupole interaction affecting the ion-neutral interaction potential. The addition of this interaction leads to a collision-dependent intermolecular force, which can be calculated (see section 2.1.4). The resulting extended theoretical excited-state collision rate in the  $\text{N}_2^+ + \text{Rb}$  system was calculated as  $k_{\text{ee}}^{(p)} = 1.7 \cdot 10^{-8} \text{ cm}^3\text{s}^{-1}$  (at an average collision energy of  $E_{\text{coll}}/k_B = 23 \text{ mK}$ ), agreeing well with the measured excited state rate within uncertainties.

The agreement between the measured excited state rate and the calculated extended theoretical excited state rate indicates an efficient charge transfer in the excited state, which was rationalised with the presence of matching excited states in the neutral molecular product resulting in near-resonant product channels. In addition to being nearly resonant, these states are also Rydberg states building on the ground

and first excited state of the molecular nitrogen ion, facilitating charge transfer. It has to be noted that the F state in molecular nitrogen, which is closest in energy to the excited state entrance channel, is not built on the ground state of the molecular ion, but it is heavily mixed with the G state at slightly lower energies. The G state is a Rydberg state built on the ground state of the molecular nitrogen ion.

**The Situation in Molecular Oxygen** The effects of the long-range part of the potential are expected to be very similar in reactions rubidium atoms with molecular oxygen ions compared to reactions with molecular nitrogen ions, as the only change from one system to the other is the reduced mass. Since molecular oxygen at 32 atomic mass units is only slightly heavier than molecular nitrogen at 28 atomic mass units, the Langevin and extended excited-state collision rates are very similar in magnitude. This similarity in the long-range interactions is not reflected in the observed reactivity. In reactions of molecular oxygen ions with rubidium atoms, the excited state of the rubidium atoms seemingly had no influence on the reactivity, contrary to the reactions of molecular nitrogen ions, where the excited state dominated the measured reactions.

As both long- and short-range effects are important for understanding the reactivity of a system, the short-range situation was examined in terms of comparison of possible entrance and product channels as it was done for the  $\text{N}_2^+ + \text{Rb}$  system. Figure 4.13 gives an overview of the closest asymptotes in the available entrance and product channels in the reactions of rubidium atoms with molecular oxygen ions with entrance channels on the left and exit channels on the right. The term energies for the excited state in neutral molecular oxygen have been taken from the NIST Chemistry WebBook [137]. The valence orbitals of the ground-state configuration of molecular oxygen in the simple molecular-orbital (MO) model are described by

$$(1\sigma_g)^2 (1\sigma_u)^2 (2\sigma_g)^2 (2\sigma_u)^2 (3\sigma_g)^2 (1\pi_u)^4 (1\pi_g)^2,$$

which in its lowest energy configuration leads to a  ${}^3\Sigma_g^-$  state. Removal of one of the electrons in the  $(1\pi_g)$  MO leads to the  $X^+ {}^2\Pi_g$  ground state of the molecular oxygen ion.

The two states in molecular oxygen on the product channel side that are closest to the entrance channel state where the rubidium atom is in the ground state are the C and d states. Both of these states are 3s Rydberg states built on the ground state of the molecular oxygen ion, which should facilitate charge transfer, but they are both higher in energy than the ground state entrance channel and not enough additional energy is present to overcome this energy difference. However, there exist energetically possible charge-transfer asymptotes, corresponding to excited states (A, A' and c states) in molecular oxygen at much lower energy than shown in Figure 4.13, which cross the potential energy curve of the  $\text{O}_2^+ - \text{Rb}$  system at its minimum, allowing for efficient charge transfer [138].

The product channels closest in energy to the entrance channel with rubidium in the excited state mostly correspond to 3p Rydberg states built on the ground state of the molecular oxygen ion. There are multiple states available at energies slightly below the level of the excited state entrance channel, which should result in efficient charge transfer. It is not exactly clear why this is not represented in the measured data shown in Figure 4.11, which does not show any trend of the reaction rate constant with regard to the rubidium atom excited-state fraction. This would indicate that the excited state reaction is not very efficient, which would bring down the excited

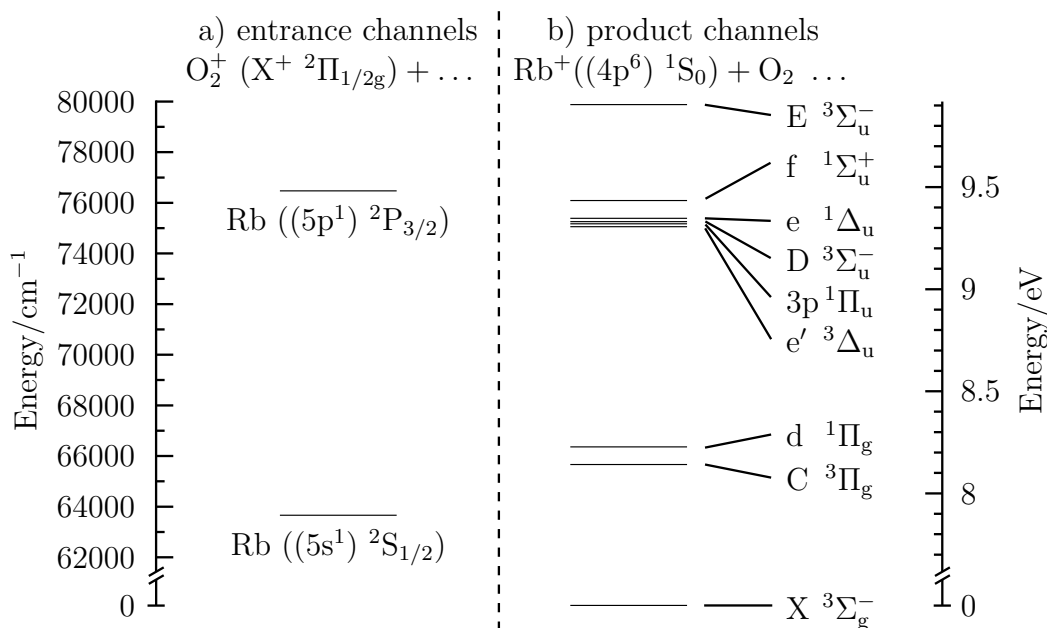


Figure 4.13: A comparison of the total electronic energies of the entrance and exit channels in the reactions of molecular oxygen ions and neutral rubidium atoms. a) The two possible entrance channels for  $\text{O}_2^+$  ( $X^+ \ ^2\Pi_{1/2g}$ ) and Rb in either its ground state ( $(5s^1) \ ^2S_{1/2}$ ) or excited state ( $(5p^1) \ ^2P_{3/2}$ ). b) Possible exit channels of a rubidium ion in its ground state ( $(4p^6) \ ^1S_0$ ) with oxygen molecules in various excited electronic states.

state reaction rate constant to the same order of magnitude as the ground state rate constant.

## 4.4 Summary and Conclusion

Initial work towards state-selected reactions of molecular oxygen ions with rubidium atoms at low collision energies was presented. Building on work by Chupka and co-workers [113, 114], the  $\text{O}_2 \ ^3\Phi_{2,3}$  states were measured for the ground and first two excited vibrational states. The molecular beam machine and time-of-flight spectrometer to achieve this were introduced.

The alignment of the molecular beam onto the ion trap center was achieved, but it was found that the loading rate of molecular oxygen ions out of the beam was too slow compared to loading unwanted ions from the background gas present in the vacuum chamber. An almost identical setup in our group was used successfully before [98], but compared to their setup, the valve on the setup presented here is approximately 50 % further away from the ion trap center. Combined with a smaller valve orifice diameter, this reduces the density of the molecular beam at the trap center by approximately one order of magnitude.

Loading molecular oxygen ions from gas leaked into the vacuum chamber was presented as an alternative to measure reactions of the vibrational ground state of the molecular ions with rubidium atoms. Using xenon gas it was shown that the

molecular oxygen ions were indeed loaded in the vibrational ground state, as only very few to no reactions were observed between the two species.

Molecular oxygen ions loaded from background gas were then used to measure their reaction rate with neutral rubidium atoms, where the fraction of atoms in the excited state was varied. It was found that the reaction with rubidium atoms in the excited state was not faster than in the ground state, even though the theoretical extended excited-state rate including quadrupole-ion interactions predicts a higher collision rate in the excited state than the Langevin rate predicts for the reactions of the rubidium atoms in the ground state. This shows the importance of considering short-range effects in the reactivity of these system.

Possible charge-transfer exit asymptotes to lower-lying valence state exist for the reactions with rubidium in the ground state. Charge transfer to these states is efficient due to a crossing at the minimum of the  $\text{O}_2^+$ -Rb potential energy surface. This also suggests that no big effect of vibrational excitation on the rate constant for  $\text{O}_2^+$  and Rb atoms in the ground state would be expected. In the  $\text{N}_2^+$ -Rb system, no such crossing exists, which is reflected in the low measured rate constant for the ground state of rubidium in that system.

For  $\text{O}_2^+$ -Rb, it is not entirely clear why the excited state reactions are much slower than the predicted rate from theory. There exist several close 3p Rydberg states in molecular oxygen as exit channels, so charge transfer is expected to be very efficient, but the experiments do not reflect that. This stands in contrast to the very similar situation of entrance and product channels for neutral rubidium atoms in the excited state in reactions with molecular nitrogen ions where the measured excited state reaction rate matched the theoretically calculated collision rate, indicating an efficient charge-transfer mechanism. The comparably slow reaction rate of molecular oxygen ions with rubidium atoms in the excited state could point to a very weak non-adiabatic coupling between entrance and exit channels. Another possibility is a too strong non-adiabatic coupling, leading to strongly avoided crossings and thus making reactions slow.

To solve the difficulties in loading from the molecular beam, a new Amsterdam pulsed valve will be implemented into the beam machine, together with larger skimmers. This should greatly improve the densities of the molecular beam at the ion trap center and thus improve the loading rate. It is clear that further studies are needed to fully understand the reactivity of molecular oxygen ions with rubidium atoms in the ground and excited state. Theoretical calculations for the  $\text{O}_2^+ + \text{Rb}$  system are currently being performed by Michał Tomza [138] and should give more insight into the underlying reaction mechanism.



# Chapter 5

## Conclusion and Outlook

**The Shuttling MOT** This thesis presents the successful implementation of a novel type of hybrid trap with increased control over the collision energies. Increased control over the kinetic energies of the atoms was achieved by shuttling the atom cloud between two off-center positions within a magneto-optical trap. By changing the intensity of the laser that pushes the atoms from one off-center position to the other, atoms at well-defined velocities were obtained. Measurements of the time of flight of the atoms were compared with Monte Carlo trajectory simulations and good agreement was found.

Drawbacks of the shuttling atom cloud are the short interaction times and low densities. This made the observation of the reaction between  $\text{Ca}^+$  ions in the ion trap and the shuttling Rb atoms impossible. However the comparably much faster reactions of Rb atoms with molecular ions such as  $\text{N}_2^+$  and  $\text{O}_2^+$  can still be studied. The density estimation of the shuttling atom cloud is also still a challenging problem. A sensitive and accurate measurement will be needed, since at high kinetic energies the atom cloud is moving fast and interaction times will be short.

**Molecular Oxygen Ions** Molecular oxygen ions have been introduced into the hybrid trap by means of resonance-enhanced multiphoton ionisation. For this, the spectra of the  $3d\delta$   $^3\Phi$  Rydberg states have been measured using a  $[2 + 1]$  photon ionisation scheme. Unfortunately, loading from the molecular beam was not achieved. The valve used in the molecular beam machine setup generated an oxygen density at the trap center that was too low, which was attributed to a combination of a too long flying distance and too small opening diameter of the valve. Molecular oxygen ions were loaded into the ion trap from background gas leaked into the chamber, which restricted the accessible vibrational level of the molecular oxygen ions to the ground state. After loading of the molecular oxygen ions into a Coulomb crystal and sympathetic cooling, they were overlapped with a stationary Rb atom cloud for an initial study of the reactivity. Reaction rate constants were determined for various excited-state population fractions of the rubidium atoms.

Even though generation of vibrationally excited molecular oxygen ions was not successful, new insight into the reaction mechanism has been gained. The observed reactivity between molecular oxygen ions in the vibrational ground state and rubidium atom was surprising. After earlier measurement using molecular nitrogen ions, where a clear dependence of the reaction rate on the excited state of the rubidium atoms was observed and ground state reactions were slow, a similar dependence was

expected in the experiments presented in this thesis. But what was found instead, is that the reaction rate of molecular oxygen ions reacting with ground state rubidium atoms is comparable to the Langevin collision rate, indicating a very efficient reaction mechanism. As the excited state population of the Rubidium atoms increased, the observed reaction rate stayed constant. This indicates an inefficient reaction mechanism in the excited state, since from theory a higher collision rate for excited state rubidium atoms is expected. Electronic structure calculations show that there exists a significant electronic barrier for the  $\text{N}_2^+ + \text{Rb}$  system in the ground state, whereas in  $\text{O}_2^+ + \text{Rb}$ , no such barrier is present [130], explaining the fast reaction rate. The reason for the inefficient reaction of  $\text{O}_2^+$  ions with Rb atoms in the excited state is still an open question. A theoretical study has not yet been performed due to the difficulty and high computational cost for excited state quantum-chemical computations in this system.

**Outlook** After the work described in this thesis, improvements aiming at increasing the stability of the experimental setup were implemented by Alexander Dörfler. Most notably, this included changes to the optical setup around the vacuum chamber. Measurements were performed of reactions of both molecular nitrogen ions and molecular oxygen ions with shuttling rubidium atoms inside the moving trap. A detailed discussion and comparison of their reactivities can be found in [130, 131].

For future work, the experiment would optimally be redesigned. The problem of slow reaction rates could be solved by increasing the density of the atom cloud substantially. A lower average temperature of the off-center atom cloud would also help with the spread in collision energy. For optimal collision energy control, the switch could be made to a moving optical molasses configuration, but this would require substantial changes to the experimental setup. If a new setup were to be designed, one could also think about using 2D MOTs to load the 3D MOT from where the atoms are launched towards the ions. This could further increase the density of atoms within the trap. If efficient loading can be achieved, a higher duty cycle would also further help with slow effective reaction rates.

# Appendix A

## New In-Vacuum Components

Over the course of this thesis, some of the in-vacuum components of the setup were replaced. The mount for the rubidium alkali metal dispenser sources needed to be replaced, as the original one broke. New commercially available calcium sources were acquired, for which new oven mounts needed to be designed. The design of both new atom source mounts is discussed in section A.1. As the frame of the old ion trap broke too, a new ion trap with the same relevant dimensions and an updated design was installed. The new ion trap is discussed in section A.2.

### A.1 New Calcium and Rubidium Sources

Initially the vacuum chamber hosted three atom sources: one rubidium alkali metal dispenser source (SAES Getters) and two homebuilt ovens consisting of resistively heated metal tubes filled with either calcium or barium powder.

For electrical connection on the old rubidium source holder, a screw through a threaded hole in the isolating Macor piece was used to clamp together the electrical connection with the alkali metal dispenser. This puts stress on the Macor holder, which broke after trying to replace an empty rubidium source with a new one. It was decided to redesign the holder of the alkali metal dispenser and, due to an initiative by Alexander Dörfler, at the same time also switch to commercially available ovens for calcium and barium (Alvatec, replaced by AlfaVakuo), for which a new oven holder needed to be designed. Both new sources are shown in Figure A.1, where the design idea behind both is detailed.

Both types of atom sources work by resistive heating by passing a current through them, for which they have two electrical connections each. On the original setup, six connections on vacuum feedthroughs were used to supply the three sources with power. To increase redundancy, the switch was made to a total of four sources, two rubidium sources and two Ca ovens. Since no additional connections on feedthroughs were available, for both, the alkali metal dispenser and the ovens, two of their connectors were combined on a single feedthrough, while the other connectors were connected to individual feedthrough connectors. To select one of the pair of the two identical sources, the common and one of the individual connections on the feedthrough are connected to the current power supply. This passes the current through just one of the two sources and leaves the other one floating. As no experiments with barium were planned, two calcium ovens were installed as well as two rubidium alkali metal dispensers.

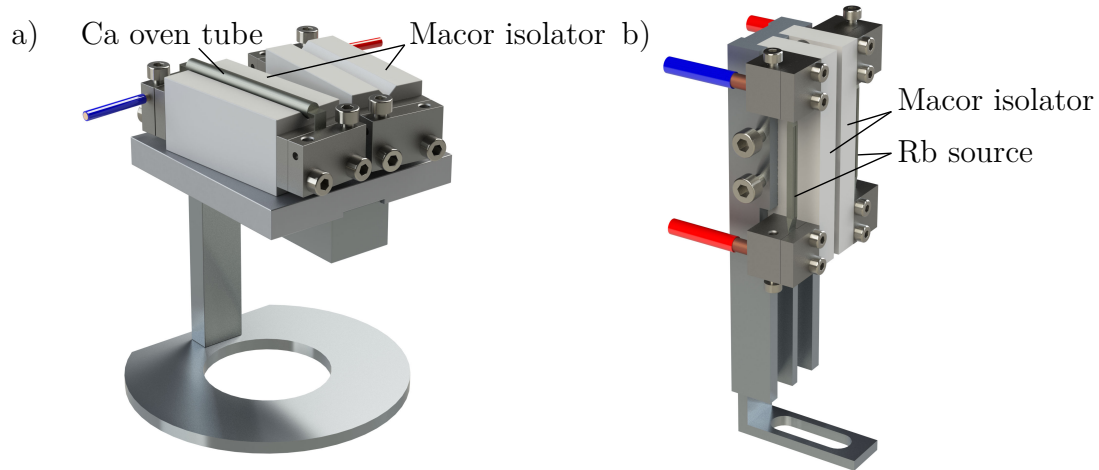


Figure A.1: Computer-generated images of the new atom sources. Both source mounts follow the same design idea, where the electrodes of the atom sources are clamped in between two metal pieces, fastened by screws. A different set of screws is used to connect the wires supplying the current and the metal pieces are attached to the Macor insulator using a third set of screws. This design allows for the screws responsible providing the electrical connection to be tightened for good contact, without putting stress on the Macor insulator. a) The calcium oven tubes (only one is shown) are resting on a Macor frame with a v-shaped groove. The two ovens are slightly angled towards each other, such that they both point at the ion trap center where the atom beams cross with the 355 nm laser beam used for ionisation. The Macor frames are mounted on a metal plate, which is itself connected to a metal stand that is clamped to the base of the vacuum chamber. b) The alkali metal dispenser sources containing rubidium are mounted vertically, hanging freely between two metal clamps. The metal clamps are connected to two Macor pieces, which themselves are connected to a metal stand.

## A.2 New Ion Trap

The ceramic holder of the old ion trap cracked as well, leading to a bad contact on one of the electrodes. This was a known flaw in the old design of the ion trap, where the endcap electrodes were connected with a screw through a threaded hole in the Macor frame. This created a weak point in the Macor piece which would lead to cracks. Figure A.2 shows a computer-generated image of the new ion trap and discusses the new design.

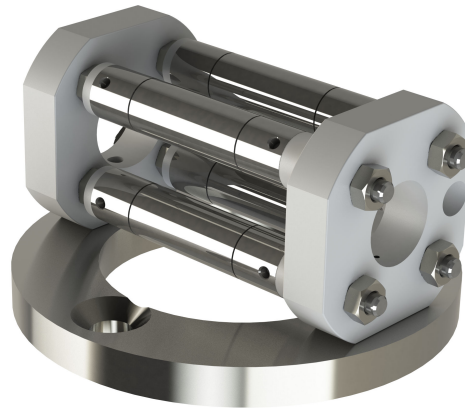


Figure A.2: A computer-generated image of the new ion trap, which was adapted from the design of the new ion trap used by Daniel Rösch [125]. Threaded holes in the endcap electrodes are used for their electrical connection. The central electrode extends through the hollow endcap electrodes and is fastened to the Macor frame using nuts. Additional Macor spacers isolate the electrodes from each other. The two Macor frames are fastened to a ground plate which is attached to the chamber base. A fibre tip mounted on a translation stage can be inserted into the trap center through a hole in the Macor frame.



# Appendix B

## LabVIEW Programs

LabVIEW is a visual programming language developed by National Instruments (<http://www.ni.com>). It is a fully functional programming language and one of its strengths lies in the simplicity of interfacing with all kinds of internal and external hardware, where libraries to do so are provided by many manufacturers. Another strength of LabVIEW is the easy creation of a user interface (UI).

Over the course of this thesis, many LabVIEW programs were written to interface with hardware and simplify a lot of aspects of the experiment. The first of the two big projects was LaserLock, a software suite consisting of a server application and various clients to lock and control many of the diode lasers in our lab. LaserLock and its design is described in section B.1. The second big project was a custom camera software to interface with the EMCCD (electron-multiplying charge-coupled device) camera, which improves productivity with features such as auto-saving of image series and quick access to change settings. The custom camera software is described in section B.2. Various other smaller programs to interface with other hardware were written and are described in section B.3. Programs written for data analysis are described in section B.4.

### B.1 LaserLock

Many of the diode lasers in our lab are locked using high-precision wavemeters (WS-U, HighFinesse). A small fraction of each laser's light is split off and sent through a fibre into to one of two fibre switches. One fibre switch is using single-mode (SM) fibres for light around 400 nm, whereas the other fibre switch uses multi-mode (MM) fibres. Each fibre switch has four input ports and one output connected to their respective wavemeters.

When the lab was initially set up, only two diode lasers needed to be locked, which was achieved with a single MM fibre switch and a single wavemeter. After the lab started to grow, more lasers needed to be locked, which was initially achieved with a program written by Matthias Germann and running on a dedicated computer. As the number of lasers needed to be locked grew even further, the original program could not handle the increased number of lasers. There was a demand for a new solution.

When the above-mentioned SM fibre switch was acquired<sup>1</sup> together with a second wavemeter, a new program LaserLock was written to accommodate the two fibre switches and two wavemeters. The new program builds on the core of the old programs and uses the same proportional-integral (PI) feedback routine for the locking. The rest however was rewritten from scratch, while maintaining a similar UI.

LaserLock was designed to be as flexible as possible. A screenshot of the main program is shown in Fig. B.1 a). There is a panel for each of the four input ports (channels) on the two fibre switches, resulting in a total of eight panels. Individual channels can be activated or deactivated as needed, so that the program only switches to channels where lasers are connected that are currently in use. The settings for the laser on a specific channel are entered in the panels corresponding to that channel. Lasers are identified by a four-letter code, a combination of their wavelength and a single letter to distinguish multiple lasers at the same wavelength.

The lasers can be locked by turning on the feedback, which can be done independently for each channel. The stabilising feedback is implemented as a PI controller, which compares the measured wavelength to the wavelength set point and applies appropriate feedback. A DAC (digital-to-analogue converter) card applies the feedback as a voltage to the laser controller to be applied to a piezo-electrical element inside the external-cavity diode lasers to finely tune the wavelength.

Before LaserLock, a screen-sharing program was used to connect to the computer where the old laser-locking software was running to change settings such as the wavelength the laser is locked to. Since screen-sharing programs are usually computationally intensive and have a lot of overhead for this application, the new laser-locking program was also designed to solve this problem. The laser-locking program acts as a server and sends all the relevant data (most importantly current wavelength, target wavelength, interferogram as measured by the wavemeter amongst other values) over the local area network<sup>2</sup> to the various experiment computers.

For the experiment computers, small and lightweight client programs were written (see Fig. B.1 b) for a screenshot), which receive the data from the server and can also send commands back to the server<sup>3</sup>. The clients can turn the locking on or off, the wavelength setpoint can be changed and channels can be activated or deactivated. A second client is used to display the interferogram used by the wavemeter to determine the wavelength (see Fig. B.1 c) for a screenshot). Every client receives all data from all lasers currently active on the server side. The four-letter codes mentioned above are used to choose the laser whose data is displayed.

---

<sup>1</sup>It was found that the UV lasers were more stably locked when the light was only guided through single mode fibres, thus a fibre switch with singlemode switches for light around 400 nm was acquired. All 397 nm lasers used in the lab are locked with this fibre switch.

<sup>2</sup>The data is sent over UDP (User Datagram Protocol), a minimal messaging protocol which does not check if the data is received or not. This simplifies the process, as the server does not need to check if the client is active or not. Dropped packets also do not disturb the client.

<sup>3</sup>To send commands, the clients use TCP/IP (Transmission Control Protocol over Internet Protocol), which provides a reliable way to share data over the network to ensure commands are received by the server.

## B.2 Custom Andor EMCCD Camera Program

The EMCCD (electron-multiplying charge-coupled device) camera program provided by the manufacturer Andor is not very well optimised for our applications, so it was decided to write a custom camera program which suits our needs. Features missing the most were easy switching of settings and automated saving of images. A camera program was written from scratch with these features in mind, resulting in the program shown in Fig. B.2. As the laser cooling of calcium ions produces only very little light, images acquired by the camera are very noisy. It is thus common to display a running average over the last few images recorded for better image quality.

Settings (exposure time, EM gain and averaging) can be changed on the fly, without interrupting the image acquisition. These settings can also be saved and recalled later for easy switching between different settings. Images are saved with the click of a single button as TIF image files where both a 16 bit version storing the actual pixel count data and an auto-scaled 8 bit version for easy viewing and printing are created. Additionally an ASCII text file is saved with the exposure, gain and averaging settings. File name is concatenated from a custom name as specified by the user, the time-stamp and a millisecond timer. The three generated files are distinguished by an additional u8, u16 and txt added to the file name for the 8 bit, 16 bit and text files, respectively.

Auto-saving of images was implemented, where images are taken in fixed time intervals as specified by the user. Images can either be recorded indefinitely until the user stops the auto-saving or a limit can be set on how many images should be recorded, where a sound cue can be played when the desired number of images is reached. The user can choose to save just a part of the image to save disk space in cases where the full sensor information is not needed (e.g. for crystal images).

Some features have not been implemented, such as binning of pixels (where multiple pixels are combined to create a larger pixel, increasing sensitivity and decreasing noise) and configuring an external trigger for the camera. As these features are generally only needed rarely (for example in temperature measurements of the atom cloud), they were not implemented. A version of the program exists that also interfaces with a function generator (TG2000, TTi (Thurlby Thandar Instruments)) to record resonance-excitation mass spectra.

## B.3 Experiment Control

Over the course of this thesis, many aspects of the experiment have been made remotely controllable from the experiment computer. For this, various LabVIEW programs have been written, some of which will be introduced below.

### B.3.1 Hybrid Trap Control

**Ion Trap Control** There are two programs to control the ion trap, one for the DC voltages applied to the electrodes and a second one that controls the power supply of the radio-frequency generator. The program that controls the DC voltages on the trap was originally written by Anatoly Johnson and is shown in Fig. B.3 a).

The second program was written when the switch was made to a new, remotely controllable power supply for the radio-frequency generator and is shown in Fig. B.3 b).

The program connects to the power supply over USB. It was kept very simple and is able to turn the generator on and off, load different radio-frequency voltage settings and turn on ramping of the voltage. The program also monitors the measured voltage and current fed into the radio-frequency generator in real time.

**MOT Coil Control** Similarly to the program that controls the power supply of the radio-frequency generator, this program controls the DC power supply that provides the current for the MOT coils. The program is shown in Fig. B.3 c). The maximum voltage and current can be set and the power supply can be turned on and off. The program also monitors the measured voltage and current fed into the MOT coils in real time.

**Oven and Shutter Control** The calcium ovens and rubidium getters are heated using simple AC power supplies able to provide a few amperes of current to the atom sources. Initially they were switched on and off with a physical switch, but a relay was installed to be able to remotely control them. The LabVIEW program shown in Fig. B.3 d) was written to interface with an Arduino board, whose digital outputs were used to control the relay inside the oven power supplies. It also remotely controls the laser beam shutter in the 355 nm beam line used to ionise calcium.

**Atom Shuttling Light Control** The required pulse sequences controlling the AOM setup as discussed in section 3.1.5 and 3.1.6 are generated using a PulseBlaster programmable TTL pulse generator from SpinCore Technologies inside a dedicated computer. A LabVIEW program on that dedicated computer is used to program the pulse generator as desired. Some sequences are fixed (e.g. loading a stationary MOT in a centre or off-centre position) while other sequences are customizable and parameters can be changed (e.g. changing the hold time in an off-centre position of a shuttling sequence).

This program acts as a server and can receive commands to switch between different sequences from the experiment computer. A client program was written for the experiment computer to send commands to the computer with the PulseBlaster installed. The program is shown in Fig. B.4 a). Commands are used to load different preprogrammed sequences, where parameters for customizable sequences are also sent over the network.

### B.3.2 REMPI Program

The program shown in Fig. B.4 b) was written to record REMPI-TOF spectra. It interfaces with the dye laser used for the ionisation, a wavemeter, an oscilloscope connected to the MCP and a laser power meter. Wavelength scans are performed by sending a command to the dye laser to set it to the desired wavelength, confirming the wavelength with the wavemeter and adjusting the wavelength if the set point and measured wavelength do not match. Then the scope's waveform with the TOF signal from the MCP is read out and the desired peak is integrated, where the integration window is set manually. For each measured point, the laser power is recorded using a power meter (PM100D, Thorlabs) connected over USB. After the spectrum is measured, all the recorded data is saved into a text file, from which the program automatically generates an image file of the plotted data.

### B.3.3 Atom Cloud Time-of-Flight Monitoring

This program interfaces with the LeCroy oscilloscope to read out the atom cloud time-of-flight traces to do long-time monitoring of the time of flight of the atom cloud, for example during reaction measurements. The oscilloscope records a total of 100k data points (photo-multiplier tube voltage versus time) over 100 ms to capture both double peak structures corresponding to forwards and backwards shuttling of the atom cloud.

The peak finding and fitting routine is rather simple. First, the trace containing the 100k data points is split into two, where each double peak structure falls into one of the two halves of the data set. Since the peaks have negative polarity, the peaks are found by finding the data points below a relative threshold. The peaks are very similar in intensity, thus this will find data points from both peaks. Taking the average time step of these data points, a time step in between the two peaks is found. The data points before this time step correspond to the first peak and the data points after this time step correspond to the second peak. It is enough to just analyse a few hundred time steps each by fitting a Gaussian distribution to determine the exact center of the two peaks. Knowing the center of the two peaks, the time of flight can be calculated. From the time of flight, the program calculates the velocity and collision energies and saves them in a text file.

## B.4 Analysis Software

Various programs were written to analyse various data sets that were recorded. Some already existed as other individual programs or scripts that were inconvenient to use. The programs presented here were all written to make data analysis simpler and automate as much as possible, which also reduces human error when manually transferring data from one program to another.

### B.4.1 Fitting Tools for Crystal Analysis

In order to determine the rate constant of the measured reaction rates, the volume of different crystals needs to be calculated. Since crystals are rotationally symmetric ellipsoids, the volume is determined by fitting a rectangle around the crystal to determine the long and short axis of the ellipsoid, from which the volume is calculated. As the reaction progresses, the shape of the remaining calcium ions changes from an ellipsoid to a flattened ellipsoid. The volume of this flattened ellipsoid can be calculated by calculating the volume of the inner cylinder and calculating the volume of the two cut ellipsoid caps for which horizontal line can be fitted to determine all the necessary dimensions for the calculation of the volume of the crystal.

All the parameters of the crystal, the long axis, short axis, radius of the flattened ellipsoid, volume of the total ellipsoid and volume of the flattened ellipsoid are constantly stored in the clipboard in real time as the various parameters are adjusted. This allows for the parameters to be easily pasted into a text file or excel for further analysis.

There is a second version of the program for the analysis of molecular ion strings inside crystals and is shown in Fig. B.5 a). Instead of fitting a horizontal line to a flattening crystal, a vertical line is fitted by hand to match the amount of molecular ions. Since the number of ions is proportional to the length of the string, instead

of saving the volume of the string, the total length (corresponding to the long axis of the crystal) and the current length is saved, together with the other parameters mentioned above. Additionally, the millisecond time stamp of the images (extracted from the file name) is saved too, since reactions with molecular ions tend to be faster and images are taken in quick succession.

To quickly analyse a lot of pseudo-first order data and make plots of all the measured reactions, another program was written that takes text files in the format produced by the programs described above and calculates a linear fit of the data to extract reaction rates.

## B.4.2 MOT Atom Number and Density Analysis

The process described in section 2.3.3 to estimate atom number and density of the atom cloud was originally done by hand, which was later somewhat automated in a combination of Matlab and bash scripts. During the course of this work, this process was further simplified and written as a standalone LabVIEW program, which is shown in Fig. B.5 b).

The program executes the full analysis of atom number and density automatically. The laser powers can either be manually typed in or read from a file, whereas detuning and camera settings (exposure time and gain) need to be put in by hand.

For the geometric analysis of the the atom cloud images, there are two modes. In the first mode, two separate one-dimensional vertical and horizontal Gaussian distributions are fitted to slices through the centre of the intensity distribution. The approximate center of the cloud is found by determination of the centroid of the brightest pixels (where the threshold for this can set by the user). The average of the  $\omega_{1/e}$  radius of both distributions is used for the density estimation. The second mode fits a symmetric two-dimensional Gaussian distribution to the full image to extract the  $\omega_{1/e}$  radius.

The number of photons scattered by the atom cloud is found by integrating the counts of the images with the atom cloud present and subtracting the integrated counts from images without the atom cloud present. From this, the atom number and density is calculated as described in section 2.3.3. The loss factors are hard-coded into the program, as they only change if the optical setup changes, which rarely happens.

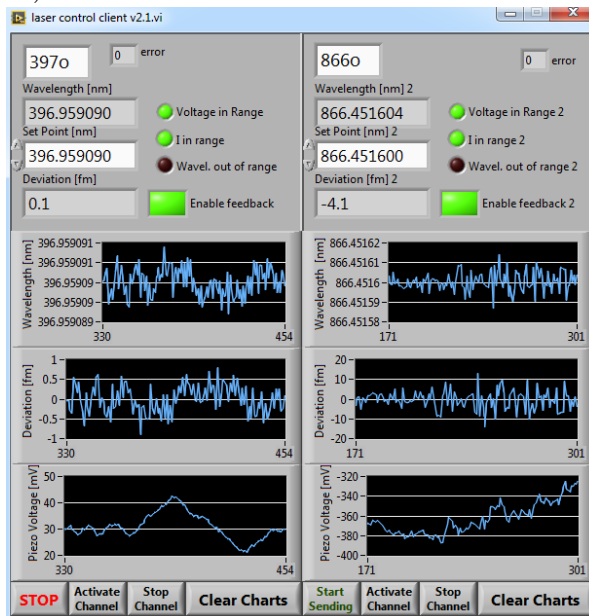
## B.4.3 Crystal and Atom Cloud Overlap Calculation

As described in section 2.5.2, an important factor in estimating reaction rates is the degree of overlap between the Coulomb crystal and the atom cloud. Originally, a Matlab script was written to calculate the overlap factor, where all necessary values had to be determined beforehand and were entered by hand. To simplify this process, a LabVIEW program with an intuitive graphical user interface, as shown in Fig. B.6, was written. The position of the atom cloud is determined automatically using the same routines as the program described in section B.4.2, whereas the size and position of the ion crystal has to be specified by hand.

a)



b)



c)

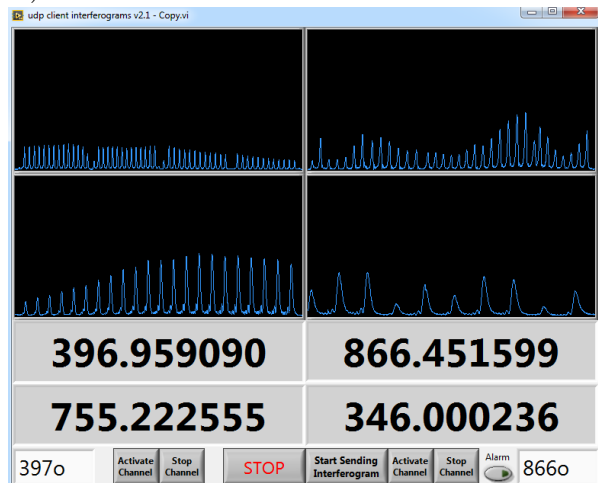


Figure B.1: LaserLock server and clients. a) The LaserLock server program. There are four channels at the top corresponding to the four channels on the single-mode (SM) fibre switch and 4 channels on the bottom corresponding to the four channels on the multi-mode (MM) fibre switch. Individual channels can be activated in the top right corner of each channel and locking is turned on with the “Enable feedback” button. Interferograms as measured by the wavemeters are displayed on the left, one each for one of the lasers connected to the SM switch (top) and one connected to the MM switch (bottom). b) The LaserLock control client which copies the look of the server panels. c) The LaserLock interferogram client which display the interferograms as measured by the wavemeters, the wavelength and the frequency of the lasers. Both clients can easily be modified to show more channels.

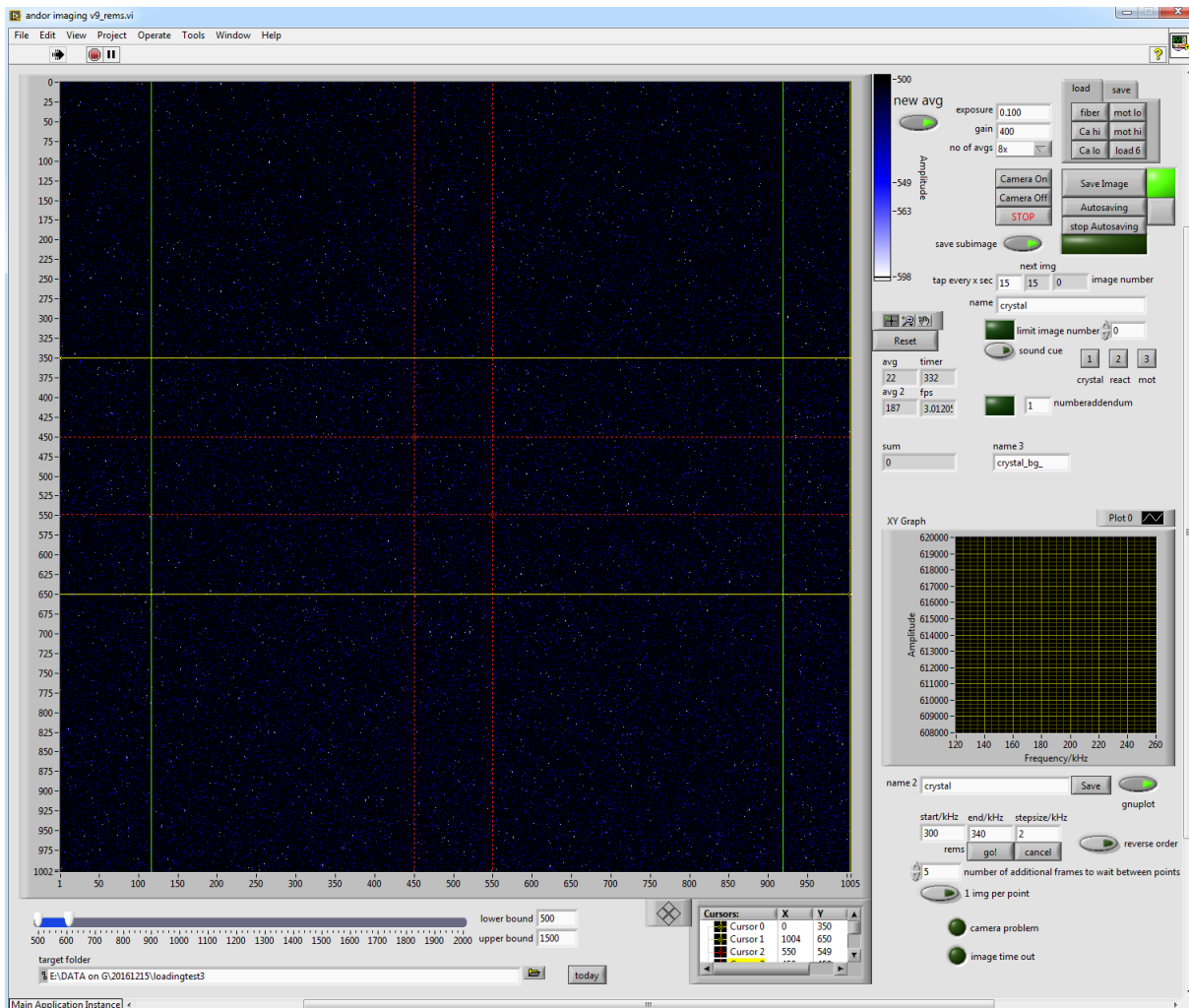


Figure B.2: Custom EMCCD (electron-multiplying charge-coupled device) camera software. The EM gain, exposure time and averaging settings are controlled in the top right corner and can be saved and recalled. There are buttons to either save single images or take images in a given interval and the user can choose to save the whole image or only part of the image. On the bottom right side are controls for measuring resonance-excitation mass spectra (REMS). The black and white point of the displayed image can be changed in the bottom left, where also the current working directory in which data is saved to can be controlled. The yellow cursors in the live image are used to set the boundary for saving only a part of the image. The red cursors set the region of interest in which the fluorescence for measuring REMS is recorded and the green cursors are used as visual guides.

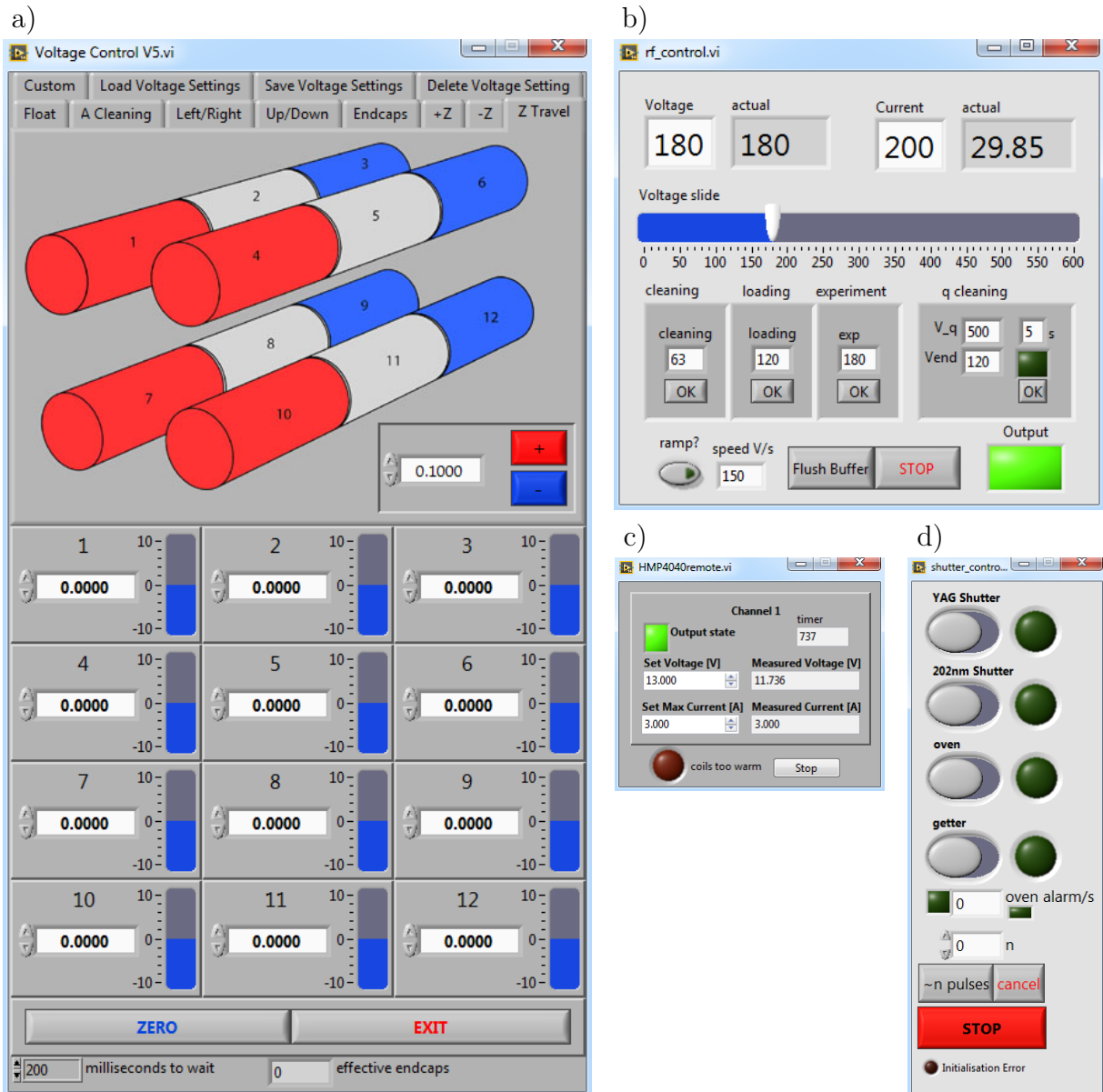
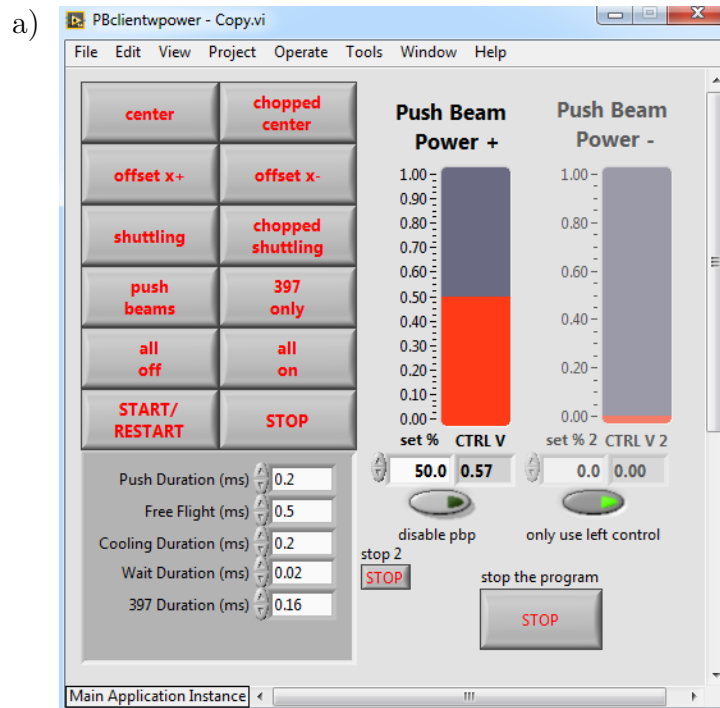


Figure B.3: a) Ion trap DC voltage control. DC voltages can either be entered by hand at the bottom or by using the different functions with the tabs at the top. Voltage settings can be saved and recalled. b) Ion trap RF voltage control. The voltage can be set in the top right corner or with the slide underneath it. Preset voltages can be entered below the slide on the left and loaded with the click of the OK button. Ramping of the voltage can be turned on in the bottom left and there is an option for q-cleaning (ejecting light ions at very high RF amplitudes) on the right. c) MOT coils DC control. The upper bound for voltage and current can be set and the power supply output can be turned on or off. d) Ionisation laser shutter and oven control. The power supplies for the calcium oven and the rubidium alkali metal sources can be turned on and off and the shutter in the beam line of the laser used to ionise the calcium can be controlled.



b)

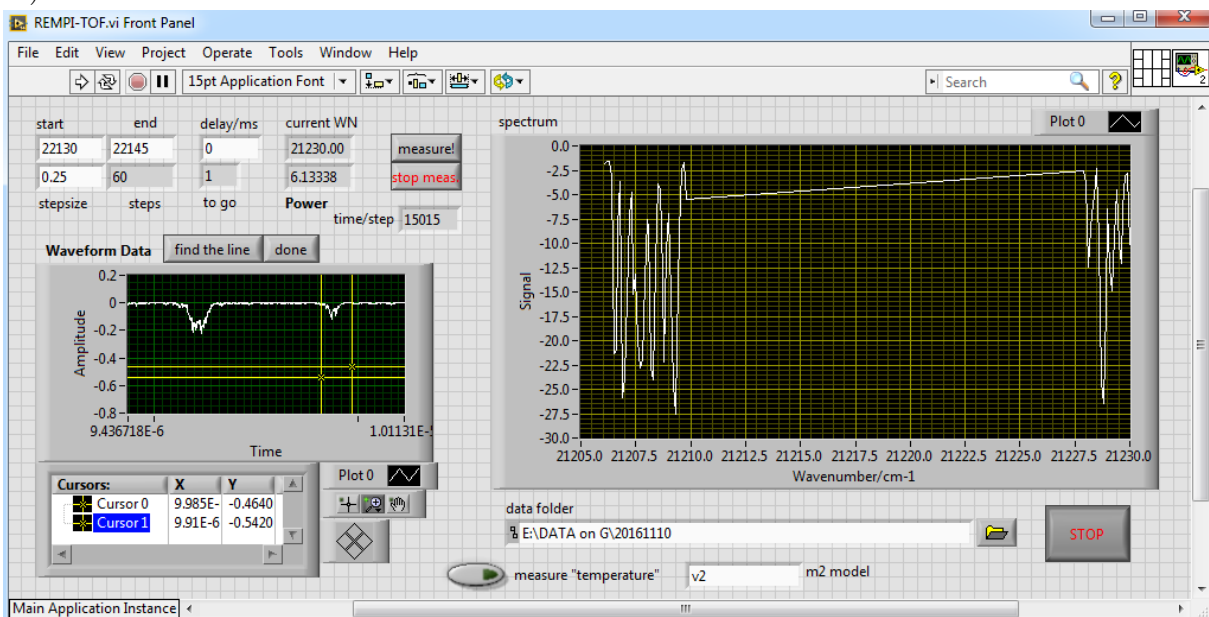


Figure B.4: a) Shuttling light control program. Different pre-programmed settings can be chosen. The program communicates with a second program running on the computer where the PulseBlaster pulse generator is installed to switch between the pulse sequences. The intensity of the pushing beam can be chosen on the right, either applying the same control voltage to both or applying individual control voltages. Hidden from view are the controls to change the cooling frequencies, as they are not changed frequently. b) Program that performs resonance-enhanced multiphoton spectroscopy. The desired wavenumber range and step size can be entered in the top left, the program then connects to the laser to perform the scan, to the oscilloscope to read out the time-of-flight traces and to a power meter to measure the laser power. After a scan is finished, the data is stored in a text file and a plot of the measured spectrum is generated automatically.

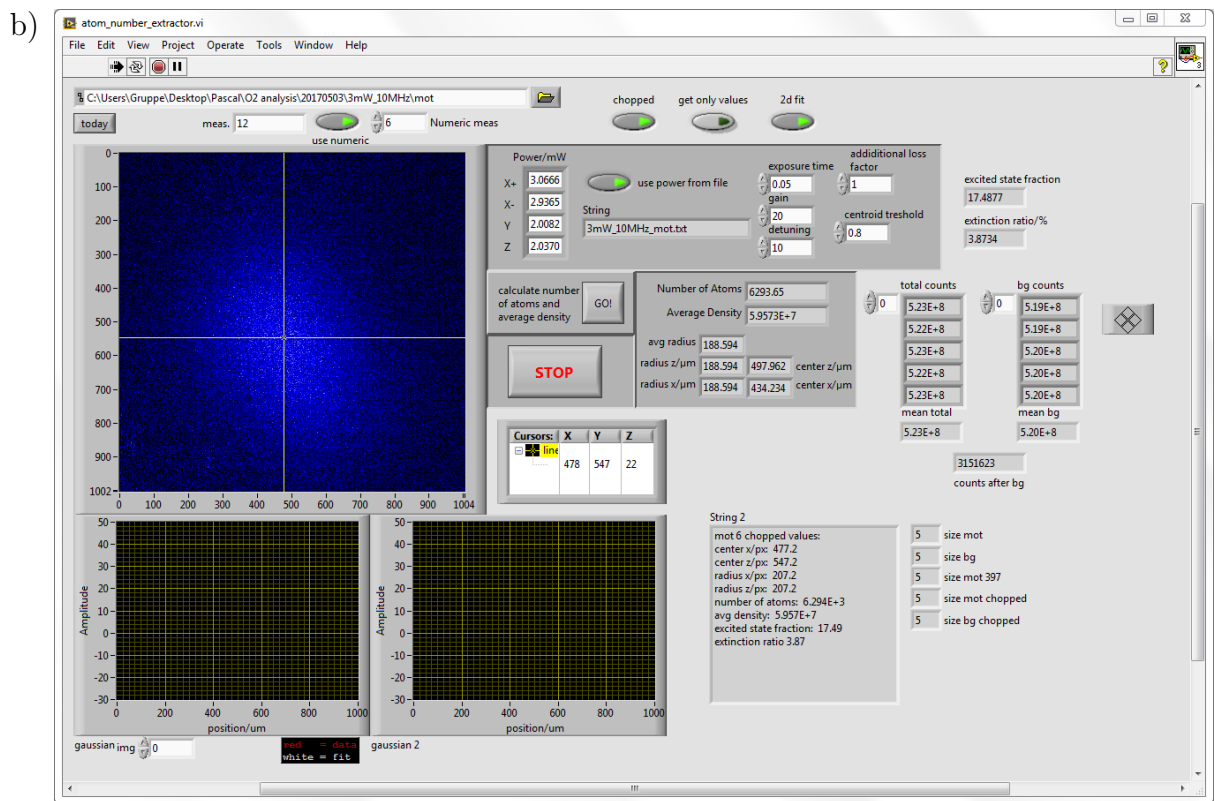
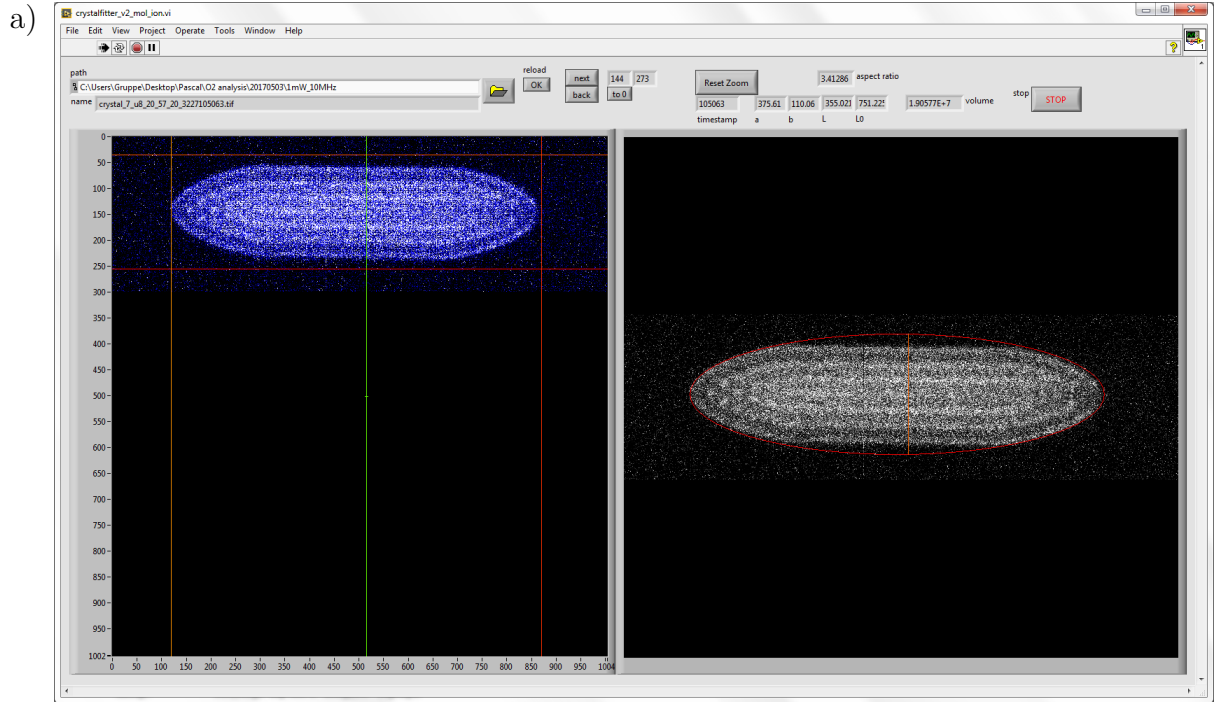


Figure B.5: a) Crystal fitting program. Images in the folder specified in the top left are loaded, were two buttons are used to switch to the next or previous image. On the left image, the red cursors are used to fit a bounding box for the ellipse of the crystal by hand, where the image on the right is used to confirm a good fit of the ellipse. The vertical green cursor on the left is used to fit the length of the string of dark ions within in the crystal. b) Atom number and density calculator. The laser powers can be entered by hand or read from a file. The atom cloud images can be fit by a two-dimensional Gaussian distribution or by a vertical and horizontal Gaussian distribution through the centroid of brightest pixels of the intensity distribution.

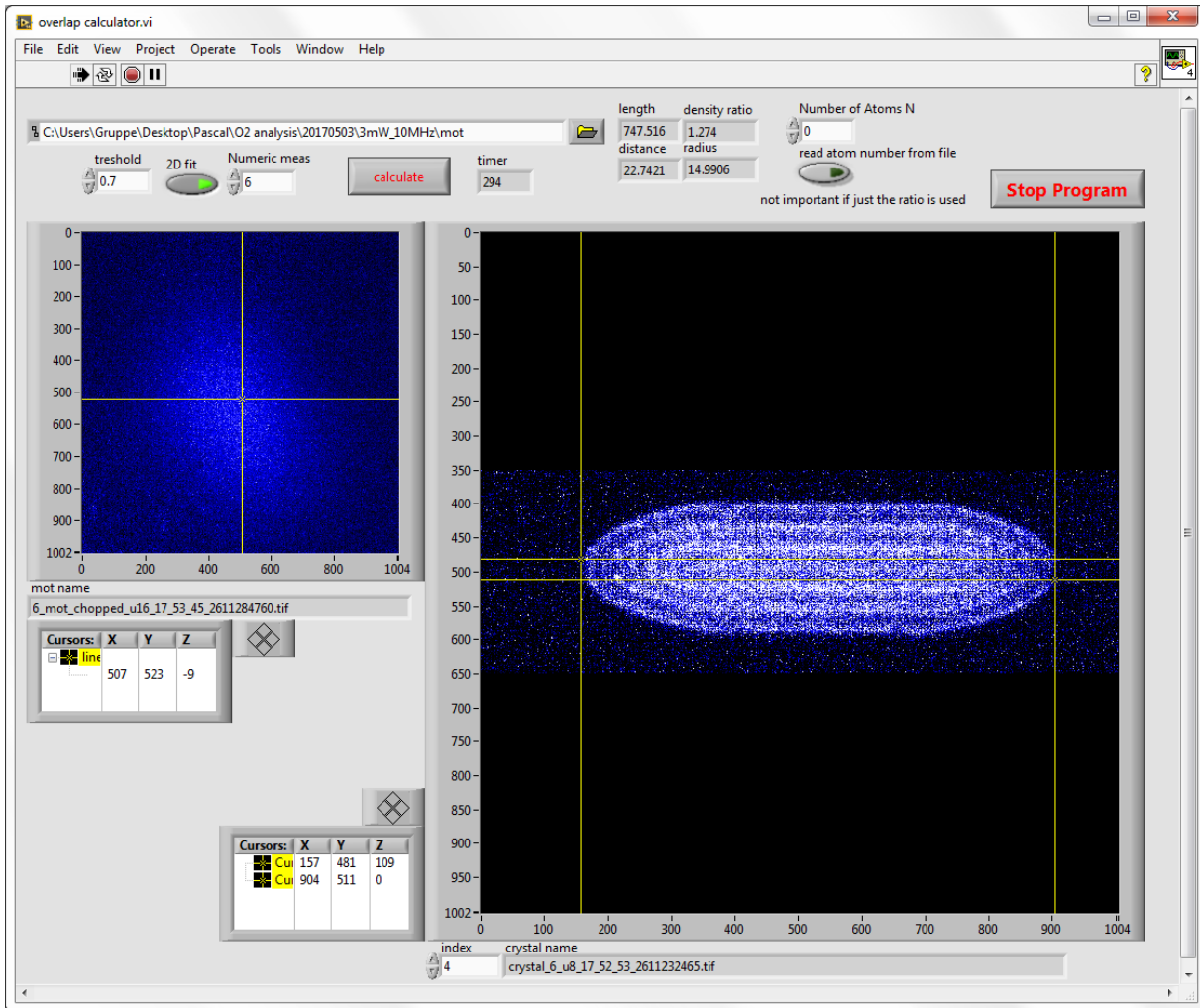


Figure B.6: A program to estimate the overlap of a dark core of light ions inside a Coulomb crystal with the atom cloud. The dimensions of the atom cloud are fit with the same routines as used by the program that estimates the atom number and density. Two yellow cursors are used to approximate the size of the dark core in the Coulomb crystal image.

# Appendix C

## Mini-Circuits Radio-Frequency Components

This section is intended as a short overview of the different radio-frequency (RF) components used in the setup that drive the various acousto-optic modulator (AOM) in the experiment. The setup is explained in detail in section 3.1.5. All the components listed were bought from Mini-Circuits and model numbers are given below.

### C.1 Voltage-Controlled Oscillator (VCO)

The radio-frequency used for the experiment is generated using voltage controlled oscillators (VCO), model ZOS-300+. They are able to produce radio-frequency at oscillation frequencies between 150 and 280 MHz, where the exact frequency is controlled by a DC voltage potential at the control port. The DC control voltages are supplied by either a dedicated power supply for the whole RF setup (in the case of RF at the pushing and compensation frequency) or by the DAC card that also supplies the DC voltages for the ion trap (in the case of the RF at cooling frequencies, allowing easy tuning of the cooling detuning from the experiment computer).

### C.2 Fixed and Voltage-Variable Attenuators

Fixed attenuators are used to reduce the RF power by a fixed amount and are used to balance the RF power in the setup. They are used in various places in the setup, but most importantly in front of the amplifiers to limit the RF power output to the AOMs. As the AOM have an upper limit on the RF power that can be dissipated of 1 W, care needs to be taken not to connect too much power. The fixed attenuator come in various levels of attenuation and have model number BW-SNW2+, where  $N$  is an integer corresponding to their attenuation in dB.

Voltage-variable attenuators (VVA) are attenuators with a control port to allow for tunable attenuation depending on the DC voltage potential applied. They are used to control the power level of the RF at the pushing frequency, which controls the intensity of the pushing laser beam. Additionally, VVAs are also used as on/off switches, because at zero voltage applied to the control port the attenuation is over 30 dB, effectively blocking the RF. The model number of the VVAs used is ZX73-2500-S+.

### **C.3 Two-Way and Four-Way RF Splitter**

Passive splitters have a single RF input, which is split equally into the desired amount of outputs. They can also be used in reverse, where multiple RF sources are combined into one single output. In our setup two-way (ZFRSC-42-S+) and four-way (ZB4PD1-500-S+) splitters are used.

### **C.4 Single Pole Double Throw Switches**

Single pole double throw (SPDT) switches have two RF inputs, one RF output, and two control inputs. The SPDT switches have model number ZX80-DR230-S+. If none of the control inputs is set to high, the output is grounded and setting either one of the two control inputs to high results in the corresponding input being wired to the output. They can also be used in reverse to route a single RF input to either of the two throw ports.

### **C.5 Amplifiers**

To get enough power into the AOM, the RF is amplified using broad-band amplifiers with model number ZHL-1-2W-S+, which work from 5 to 500 MHz. These amplifiers can produce up to 2 W of RF power, but the power limit of the AOM of 1 W should not be exceeded. The output power is controlled using various fixed attenuators at the input of the amplifier.

# Bibliography

- [1] F. H. J. Hall, *Cold ion-neutral reactions*, PhD thesis, University of Basel, 2013.
- [2] A. Einstein, *Phys. Z.* **18**, 121 (1917).
- [3] R. Frisch, *Z. Phys.* **86**, 42 (1933).
- [4] A. Ashkin, *Phys. Rev. Lett.* **25**, 1321 (1970).
- [5] J.-L. Picqué and J.-L. Vialle, *Opt. Comm.* **5**, 402 (1972).
- [6] R. Schieder, H. Walther, and L. Wöste, *Opt. Comm.* **5**, 337 (1972).
- [7] T. W. Hänsch and A. L. Schawlow, *Opt. Comm.* **13**, 68 (1975).
- [8] D. Wineland and H. Dehmelt, *Bull. Am. Phys. Soc.* **20**, 637 (1975).
- [9] W. Neuhauser, M. Hohenstatt, P. Toschek, and H. Dehmelt, *Phys. Rev. Lett.* **41**, 233 (1978).
- [10] D. J. Wineland, R. E. Drullinger, and F. L. Walls, *Phys. Rev. Lett.* **40**, 1639 (1978).
- [11] A. Ashkin, *Phys. Rev. Lett.* **40**, 729 (1978).
- [12] G. A. Askar'yan, *Sov. Phys. JETP* **15**, 1088 (1962).
- [13] V. Letokhov, *JETP Lett.* **7**, 272 (1968).
- [14] J. E. Bjorkholm, R. R. Freeman, A. Ashkin, and D. B. Pearson, *Phys. Rev. Lett.* **41**, 1361 (1978).
- [15] J. Prodan, A. Migdall, W. D. Phillips, I. So, H. Metcalf, and J. Dalibard, *Phys. Rev. Lett.* **54**, 992 (1985).
- [16] W. Ertmer, R. Blatt, J. L. Hall, and M. Zhu, *Phys. Rev. Lett.* **54**, 996 (1985).
- [17] A. L. Migdall, J. V. Prodan, W. D. Phillips, T. H. Bergeman, and H. J. Metcalf, *Phys. Rev. Lett.* **54**, 2596 (1985).
- [18] S. Chu, L. Hollberg, J. E. Bjorkholm, A. Cable, and A. Ashkin, *Phys. Rev. Lett.* **55**, 48 (1985).
- [19] S. Chu, J. E. Bjorkholm, A. Ashkin, and A. Cable, *Phys. Rev. Lett.* **57**, 314 (1986).
- [20] E. L. Raab, M. Prentiss, A. Cable, S. Chu, and D. E. Pritchard, *Phys. Rev. Lett.* **59**, 2631 (1987).

- [21] M. A. Kasevich, E. Riis, S. Chu, and R. G. DeVoe, *Phys. Rev. Lett.* **63**, 612 (1989).
- [22] J. R. Zacharias, unpublished (1953); work mentioned in: *Phys. Rev.* **94**, 751 (1954).
- [23] N. F. Ramsey, *Phys. Rev.* **78**, 695 (1950).
- [24] M. Kasevich, D. S. Weiss, E. Riis, K. Moler, S. Kasapi, and S. Chu, *Phys. Rev. Lett.* **66**, 2297 (1991).
- [25] M. A. Lombardi, T. P. Heavner, and S. R. Jeffer, *NCSLI Measure J. Meas. Sci.* **2**, 74 (2007).
- [26] A. Clairon, S. Ghezali, G. Santarelli, P. Laurent, S. N. Lea, M. Bahoura, E. Simon, S. Weyers, and K. Szymaniec, in *Proc. 5th Symp. Freq. Standards and Metrology*, edited by J. C. Bergquist, p. 45, World Scientific, 1996.
- [27] A. Clairon, P. Laurent, G. Santarelli, S. Ghezali, S. N. Lea, and M. Bahoura, *IEEE Trans. Instrum. Meas* **44**, 128 (1995).
- [28] T. P. Heavner, E. A. Donley, F. Levi, G. Costanzo, T. E. Parker, J. H. Shirley, N. Ashby, S. Barlow, and S. R. Jefferts, *Metrologia* **51**, 174 (2014).
- [29] G. K. Campbell, A. D. Ludlow, S. Blatt, J. W. Thomsen, M. J. Martin, M. H. G. de Miranda, T. Zelevinsky, M. M. Boyd, J. Ye, S. A. Diddams, T. P. Heavner, T. E. Parker, and S. R. Jefferts, *Metrologia* **45**, 539 (2008).
- [30] C. W. Chou, D. B. Hume, J. C. J. Koelemeij, D. J. Wineland, and T. Rosenband, *Phys. Rev. Lett.* **104**, 070802 (2010).
- [31] E. Riis, D. S. Weiss, K. A. Moler, and S. Chu, *Phys. Rev. Lett.* **64**, 1658 (1990).
- [32] J. Nellesen, J. Werner, and W. Ertmer, *Opt. Commun.* **78**, 300 (1990).
- [33] J. Yu, J. Djemaa, P. Nosbaum, and P. Pillet, *Opt. Commun.* **112**, 136 (1994).
- [34] T. B. Swanson, N. J. Silva, S. K. Mayer, J. J. Maki, and D. H. McIntyre, *J. Opt. Soc. Am. B* **13**, 1833 (1996).
- [35] S. Weyers, E. Aucouturier, C. Valentin, and N. Dimarcq, *Opt. Commun.* **143**, 30 (1997).
- [36] S.-Q. Shang, B. Sheehy, H. Metcalf, P. van der Straten, and G. Nienhuis, *Phys. Rev. Lett.* **67**, 1094 (1991).
- [37] J. Catani, P. Maioli, L. De Sarlo, F. Minardi, and M. Inguscio, *Phys. Rev. A* **73**, 033415 (2006).
- [38] M. Petersen, R. Chicireanu, S. T. Dawkins, D. V. Magalhães, C. Mandache, Y. Le Coq, A. Clairon, and S. Bize, *Phys. Rev. Lett.* **101**, 183004 (2008).
- [39] T. G. Tiecke, S. D. Gensemer, A. Ludewig, and J. T. M. Walraven, *Phys. Rev. A* **80**, 013409 (2009).

- [40] S. Dörscher, B. Thobe, Alexander nd Hundt, A. Kochanke, R. Le Targat, P. Windpassinger, C. Becker, and K. Sengstock, *Rev. Sci. Instrum.* **84**, 043109 (2013).
- [41] I. Nosske, L. Couturier, F. Hu, C. Tan, C. Qiao, J. Blume, Y. H. Jiang, P. Chen, and M. Weidemüller, *Phys. Rev. A* **96**, 053415 (2017).
- [42] C. J. Myatt, N. R. Newbury, R. W. Ghrist, S. Loutzenhiser, and C. E. Wieman, *Opt. Lett.* **21**, 290 (1996).
- [43] T. B. Swanson, D. Asgeirsson, J. A. Behr, A. Gorelov, and D. Melconian, *J. Opt. Soc. Am. B* **15**, 2641 (1998).
- [44] E. Dimova, O. Morizot, G. Stern, C. L. Garrido Alzar, A. Fioretti, V. Lorent, D. Comparat, H. Perrin, and P. Pillet, *Eur. Phys. J. D* **42**, 299 (2007).
- [45] S. R. Mishra, S. P. Ram, S. K. Tiwari, and S. C. Mehendale, *Phys. Rev. A* **77**, 065402 (2008).
- [46] Z. T. Lu, K. L. Corwin, M. J. Renn, M. H. Anderson, E. A. Cornell, and C. E. Wieman, *Phys. Rev. Lett.* **77**, 3331 (1996).
- [47] M. Yan, J. Yin, and Y. Zhu, *J. Opt. Soc. Am. B* **17**, 1817 (2000).
- [48] T. Müller, T. Wendrich, M. Gilowski, C. Jentsch, E. M. Rasel, and W. Ertmer, *Phys. Rev. A* **76**, 063611 (2007).
- [49] T. Müller, M. Gilowski, M. Zaiser, P. Berg, C. Schubert, T. Wendrich, W. Ertmer, and E. M. Rasel, *Eur. Phys. J. D* **53**, 273 (2009).
- [50] R. Grimm, M. Weidemüller, and Y. B. Ovchinnikov, *Optical dipole traps for neutral atoms*, , *Advances In Atomic, Molecular, and Optical Physics Vol. 42*, pp. 95 – 170, Academic Press, 2000.
- [51] M. Ben Dahan, E. Peik, J. Reichel, Y. Castin, and C. Salomon, *Phys. Rev. Lett.* **76**, 4508 (1996).
- [52] F. Bloch, *Z. Phys.* **52**, 555 (1929).
- [53] C. Zener, *Proc. R. Soc. London A* **145**, 523 (1934).
- [54] S. R. Wilkinson, C. F. Bharucha, K. W. Madison, Q. Niu, and M. G. Raizen, *Phys. Rev. Lett.* **76**, 4512 (1996).
- [55] G. H. Wannier, *Phys. Rev.* **117**, 432 (1960).
- [56] S. Kuhr, W. Alt, D. Schrader, M. Müller, V. Gomer, and D. Meschede, *Science* **293**, 278 (2001).
- [57] S. Schmid, G. Thalhammer, K. Winkler, F. Lang, and J. H. Denschlag, *New J. Phys.* **8**, 159 (2006).
- [58] S. M. Dickerson, J. M. Hogan, A. Sugarbaker, D. M. S. Johnson, and M. A. Kasevich, *Phys. Rev. Lett.* **111**, 083001 (2013).

- [59] M. Greiner, I. Bloch, T. W. Hänsch, and T. Esslinger, *Phys. Rev. A* **63**, 031401 (2001).
- [60] W. Hänsel, J. Reichel, P. Hommelhoff, and T. W. Hänsch, *Phys. Rev. Lett.* **86**, 608 (2001).
- [61] O. P. Makarov, R. Côté, H. Michels, and W. W. Smith, *Phys. Rev. A* **67**, 042705 (2003).
- [62] M. Cetina, A. Grier, J. Campbell, I. Chuang, and V. Vuletić, *Phys. Rev. A* **76**, 041401 (2007).
- [63] A. T. Grier, M. Cetina, F. Oručević, and V. Vuletić, *Phys. Rev. Lett.* **102**, 223201 (2009).
- [64] W. G. Rellergert, S. T. Sullivan, S. Kotochigova, A. Petrov, K. Chen, S. J. Schowalter, and E. R. Hudson, *Phys. Rev. Lett.* **107**, 243201 (2011).
- [65] F. H. J. Hall, M. Aymar, N. Bouloufa-Maafa, O. Dulieu, and S. Willitsch, *Phys. Rev. Lett.* **107**, 243202 (2011).
- [66] I. Sivarajah, D. S. Goodman, J. E. Wells, F. A. Narducci, and W. W. Smith, *Phys. Rev. A* **86**, 063419 (2012).
- [67] K. Ravi, S. Lee, A. Sharma, G. Werth, and S. A. Rangwala, *Nat. Commun.* **3**, 1126 (2012).
- [68] C. Zipkes, S. Palzer, L. Ratschbacher, C. Sias, and M. Köhl, *Phys. Rev. Lett.* **105**, 133201 (2010).
- [69] C. Zipkes, S. Palzer, C. Sias, and M. Köhl, *Nature* **464**, 388 (2010).
- [70] S. Schmid, A. Härter, and J. H. Denschlag, *Phys. Rev. Lett.* **105**, 133202 (2010).
- [71] S. Haze, S. Hata, M. Fujinaga, and T. Mukaiyama, *Phys. Rev. A* **87**, 052715 (2013).
- [72] F. H. J. Hall and S. Willitsch, *Phys. Rev. Lett.* **109**, 233202 (2012).
- [73] F. H. Hall, M. Aymar, M. Raoult, O. Dulieu, and S. Willitsch, *Molecular Physics* **111**, 1683 (2013).
- [74] T. Sikorsky, Z. Meir, R. Ben-shlomi, N. Akerman, and R. Ozeri, *Nat. Commun.* **9**, 920 (2018).
- [75] F. H. Hall, P. Eberle, G. Hegi, M. Raoult, M. Aymar, O. Dulieu, and S. Willitsch, *Mol. Phys.* **111**, 2020 (2013).
- [76] L. Ratschbacher, C. Zipkes, C. Sias, and M. Köhl, *Nat. Phys.* **8**, 649 (2012).
- [77] W. G. Rellergert, S. T. Sullivan, S. J. Schowalter, S. Kotochigova, K. Chen, and E. R. Hudson, *Nature* **495**, 490 (2013).
- [78] H. da Silva Jr, M. Raoult, M. Aymar, and O. Dulieu, *New J. Phys.* **17**, 045015 (2015).

- [79] J. Joger, H. Fürst, N. Ewald, T. Feldker, M. Tomza, and R. Gerritsma, *Phys. Rev. A* **96**, 030703 (2017).
- [80] S. Willitsch, M. T. Bell, A. D. Gingell, S. R. Procter, and T. P. Softley, *Phys. Rev. Lett.* **100**, 043203 (2008).
- [81] Y.-P. Chang, K. Długołęcki, J. Küpper, D. Rösch, D. Wild, and S. Willitsch, *Science* **342**, 98 (2013).
- [82] S. D. Hogan, M. Motsch, and F. Merkt, *Phys. Chem. Chem. Phys.* **13**, 18705 (2011).
- [83] E. Narevicius and M. G. Raizen, *Chemical Reviews* **112**, 4879 (2012).
- [84] S. Y. T. van de Meerakker, H. L. Bethlem, N. Vanhaecke, and G. Meijer, *Chemical Reviews* **112**, 4828 (2012).
- [85] S. Chervenkov, X. Wu, J. Bayerl, A. Rohlfes, T. Gantner, M. Zeppenfeld, and G. Rempe, *Phys. Rev. Lett.* **112**, 013001 (2014).
- [86] E. S. Shuman, J. F. Barry, and D. DeMille, *Nature* **467**, 820 (2010).
- [87] J. F. Barry, D. J. McCarron, E. B. Norrgard, M. H. Steinecker, and D. DeMille, *Nature* **512**, 286 (2014).
- [88] M. T. Hummon, M. Yeo, B. K. Stuhl, A. L. Collopy, Y. Xia, and J. Ye, *Phys. Rev. Lett.* **110**, 143001 (2013).
- [89] S. Truppe, H. J. Williams, M. Hambach, L. Caldwell, N. J. Fitch, E. A. Hinds, B. E. Sauer, and M. R. Tarbutt, *Nat. Phys.* **13** (2017).
- [90] L. Anderegg, B. L. Augenbraun, E. Chae, B. Hemmerling, N. R. Hutzler, A. Ravi, A. Collopy, J. Ye, W. Ketterle, and J. M. Doyle, *Phys. Rev. Lett.* **119**, 103201 (2017).
- [91] I. Kozyryev, L. Baum, K. Matsuda, B. L. Augenbraun, L. Anderegg, A. P. Sedlack, and J. M. Doyle, *Phys. Rev. Lett.* **118**, 173201 (2017).
- [92] K. Mølhave and M. Drewsen, *Phys. Rev. A* **62**, 011401 (2000).
- [93] B. Roth, P. Blythe, H. Wenz, H. Daerr, and S. Schiller, *Phys. Rev. A* **73**, 042712 (2006).
- [94] M. T. Bell, A. D. Gingell, J. M. Oldham, T. P. Softley, and S. Willitsch, *Faraday Discuss.* **142**, 73 (2009).
- [95] P. F. Staantum, K. Højbjerg, P. S. Skyt, A. K. Hansen, and M. Drewsen, *Nat. Phys.* **6**, 271 (2010).
- [96] T. Schneider, B. Roth, H. Duncker, I. Ernsting, and S. Schiller, *Nat. Phys.* **6**, 275 (2010).
- [97] X. Tong, A. H. Winney, and S. Willitsch, *Phys. Rev. Lett.* **105**, 143001 (2010).
- [98] X. Tong, D. Wild, and S. Willitsch, *Phys. Rev. A* **83**, 023415 (2011).

- [99] Y. Wang, C. A. Woodward, and W. A. Chupka, *Chem. Phys. Lett.* **214**, 290 (1993).
- [100] A. Dochain and X. Urbain, *EPJ Web of Conferences* **84**, 05001 (2015).
- [101] N. S. Shuman, D. E. Hunton, and A. A. Viggiano, *Chem. Rev.* **115**, 4542 (2015).
- [102] J. R. Peterson and Y. K. Bae, *Phys. Rev. A* **30**, 2807 (1984).
- [103] W. V. D. Zande, W. Koot, J. Peterson, and J. Los, *Chem. Phys. Lett.* **140**, 175 (1987).
- [104] A. Petrigiani, W. J. van der Zande, P. C. Cosby, F. Hellberg, R. D. Thomas, and M. Larsson, *J. Chem. Phys.* **122**, 014302 (2005).
- [105] T. P. Snow and V. M. Bierbaum, *Annu. Rev. Anal. Chem.* **1**, 229 (2008).
- [106] R. D. Levine, *Molecular Reaction Dynamics* (Cambridge University Press, 2005).
- [107] M. Krych, W. Skomorowski, F. Pawłowski, R. Moszynski, and Z. Idziaszek, *Phys. Rev. A* **83**, 032723 (2011).
- [108] P. Langevin, *Ann. Chim. Phys.* **5**, 245 (1905).
- [109] A. B. Henson, S. Gersten, Y. Shagam, J. Narevicius, and E. Narevicius, *Science* **338**, 234 (2012).
- [110] C. Foot, *Atomic Physics* (Oxford University Press, 2005).
- [111] D. A. Steck, Rubidium 87 D Line Data. <https://steck.us/alkalidata/rubidium87numbers.1.6.pdf>, 2001.
- [112] M. H. Shah, H. A. Camp, M. L. Trachy, G. Veshapidze, M. A. Gearba, and B. D. DePaola, *Phys. Rev. A* **75**, 053418 (2007).
- [113] R. J. Yokelson, R. J. Lipert, and W. A. Chupka, *J. Chem. Phys.* **97**, 6144 (1992).
- [114] H. Park, L. Li, W. A. Chupka, and H. Lefebvre-Brion, *J. Chem. Phys.* **92**, 5835 (1990).
- [115] G. Herzberg, *Molecular Spectra and Molecular Structure: I. Spectra of diatomic molecules* (Van Nostrand, 1950).
- [116] C. C. Bradley, J. J. McClelland, W. R. Anderson, and R. J. Celotta, *Phys. Rev. A* **61**, 053407 (2000).
- [117] B. Roth, P. Blythe, and S. Schiller, *Phys. Rev. A* **75**, 023402 (2007).
- [118] S. Willitsch, M. T. Bell, A. D. Gingell, and T. P. Softley, *Phys. Chem. Chem. Phys.* **10**, 7200 (2008).
- [119] M. Drewsen and A. Brøner, *Phys. Rev. A* **62**, 045401 (2000).

- [120] P. Eberle, *A Study of Reactions Between Laser-Cooled Calcium Ions and Rubidium Atoms at Ultra-Low Collision Energies*, Master's thesis, University of Basel, 2012.
- [121] S. Schlemmer, T. Kuhn, E. Lescop, and D. Gerlich, *Int. J. Mass Spectrom.* **185-187**, 589 (1999).
- [122] F. Grieman, J. Hansen, and J. Moseley, *Chem. Phys. Lett.* **85**, 53 (1982).
- [123] H. Böhlinger, M. Durup-Ferguson, D. W. Fahey, F. C. Fehsenfeld, and E. E. Ferguson, *J. Chem. Phys.* **79**, 4201 (1983).
- [124] L. E. de Clercq, H.-Y. Lo, M. Marinelli, D. Nadlinger, R. Oswald, V. Negnevitsky, D. Kienzler, B. Keitch, and J. P. Home, *Phys. Rev. Lett.* **116**, 080502 (2016).
- [125] D. Rösch, *Reactive collisions with conformationally controlled molecules*, PhD thesis, University of Basel, 2016.
- [126] P. W. Smith and R. Hänsch, *Phys. Rev. Lett.* **26**, 740 (1971).
- [127] K. B. MacAdam, A. Steinbach, and C. Wieman, *Am. J. Phys* **60**, 1098 (1992).
- [128] B. Fröhlich, T. Lahaye, B. Kaltenhäuser, H. Kübler, S. Müller, T. Koch, M. Fattori, and T. Pfau, *Rev. Sci. Instrum.* **78**, 043101 (2007).
- [129] C. von Planta, *Numerical Simulation of a Shuttling Rubidium Atom Cloud in a Magneto-Optical Trap with Optimized Kinetic Energy Resolution*, Master's thesis, University of Basel, 2015.
- [130] A. D. Dörfler, P. Eberle, D. Koner, M. Tomza, M. Meuwly, and S. Willitsch, *Nat. Commun.* **10**, 5429 (2019).
- [131] A. D. Dörfler, *Cold molecular ion-neutral collisions in a dynamic ion-atom hybrid trap*, PhD thesis, University of Basel, 2020.
- [132] LeCroy, Application Note AN\_006 - Digital Oscilloscopes - Enhanced Resolution. <http://teledynelecroy.com/doc/digital-oscilloscopes-enhanced-resolution>, 1999.
- [133] D. Gerlich, G. Jerke, U. Mück and U. Person, Schnelles Ventil zur Erzeugung sehr kurzer Gasimpulse. [http://www.tu-chemnitz.de/physik/ION/Technology/Piezo\\_Valve/](http://www.tu-chemnitz.de/physik/ION/Technology/Piezo_Valve/), 1990.
- [134] C. T. Rettner, E. E. Marinero, R. N. Zare, and A. H. Kung, *J. Chem. Phys.* **88**, 4459 (1984).
- [135] M. E. Weber, N. F. Dalleska, B. L. Tjelta, E. R. Fisher, and P. B. Armentrout, *J. Chem. Phys.* **98**, 7855 (1993).
- [136] A. B. van der Kamp, P. Cosby, and W. J. van der Zande, *Chemical Physics* **184**, 319 (1994).

- [137] K. Huber and G. Herzberg, Constants of diatomic molecules (data prepared by J.W. Gallagher and R.D. Johnson, III), in *NIST Chemistry WebBook, NIST Standard Reference Database Number 69*, edited by P. Linstrom and W. Mallard, retrieved June 2017.
- [138] M. Tomza, private communication (2017).